Potential For Tsunami Detection And Early-Warning Using Space-Based Passive Microwave Radiometry

by

Rebecca G. Myers

B.S., Aerospace Engineering (Astro)
United States Naval Academy, 2003

Submitted to the Department of Aeronautics and Astronautics
in partial fulfillment of the requirements for the degree of

Master of Science in Aeronautical and Astronautical Engineering

at the

MASSACHUSETTS INSTITUTE OF TECHNOLOGY

February 2008

Author .....
Department of Aeronautics and Astronautics
February 1, 2008

Certified by .....
Dr. Victor Y. Raizer
Zel Technologies, LLC
Thesis Reader

Certified by .....
Capt. John E. Draim
USN, ret.
Thesis Reader

Certified by .....
Dr. Paul J. Cefola
Lecturer, Department of Aeronautics and Astronautics
Thesis Supervisor

Certified by .....
Dr. David Miller
Professor, Department of Aeronautics and Astronautics
Thesis Supervisor

Accepted by .....
Dr. David Darmofal
Associate Professor of Aeronautics and Astronautics
Chair, Committee on Graduate Students

Potential For Tsunami Detection And Early-Warning Using Space-Based Passive Microwave Radiometry

by

Rebecca G. Myers

Submitted to the Department of Aeronautics and Astronautics
on February 1, 2008, in partial fulfillment of the
requirements for the degree of
Master of Science in Aeronautical and Astronautical Engineering

Abstract

The threat of a tsunami in coastal communities is considerable, especially in the Pacific and Indian Oceans. Current warning systems consist of two networks: (1) a network of seismometers, and (2) a network of sea level gauges and bottom pressure recorders. Bottom pressure recorders communicate with ocean surface buoys, which send the data to processing centers through satellite communication uplinks. The ability to quickly and accurately detect a tsunami in the deep ocean is proposed using a new space-based passive microwave radiometer system. Passive microwave radiometry can detect oceanic parameters such as sea-surface temperature and sea surface roughness to contribute to earlier tsunami detection, when the tsunami is farther from shore, which will increase the reaction time for at-risk coastal communities.

This thesis will outline a physics based approach to manipulating brightness temperature data from the ocean's surface through the variation as a result of the satellite platform, the sensor, its location, the antenna, and other considerations. The thesis will give a description of how each component of the overall system will change the surface data because the observations are space-based. The thesis will also outline how the current detection system can be compared to the new space-based system. In the future, the comparison method can be used to make an argument to support the system with the best capability to serve as an efficient and accurate tsunami early-warning system.

Thesis Reader: Dr. Victor Y. Raizer
Title: Zel Technologies, LLC

Thesis Reader: Capt. John E. Draim
Title: USN, ret.

Thesis Supervisor: Dr. Paul J. Cefola
Title: Lecturer, Department of Aeronautics and Astronautics

Thesis Supervisor: Dr. David Miller
Title: Professor, Department of Aeronautics and Astronautics

Acknowledgments

Over the past three semesters (and a summer) I have learned more about tsunami, oceanography, and physics than I have in my entire life. I would like to thank Paul Cefola for taking me on as an unfunded graduate student and helping me select the topic of my thesis. He was instrumental in the form and purpose of the thesis. His guidance, help, and suggestions slowly allowed me to grow as a student and helped me to ease into this broad topic. He also was always trying to find ways to help me move forward and also to find funding for this area of research. Despite the difficulty in getting funding, the overall experience is one that cannot be found anywhere else (nor would I want to find it anywhere else). I would also like to thank him for the internship and the job opportunity that he opened for me.

Without the help of Victor Raizer, an expert in the field of radiometry, I would still not understand how a radiometer works. He helped answer questions about radiometry and its uses. His references and papers also formed a large portion of the background material on radiometry for the thesis. Capt. John Draim, USN, ret., helped me understand the applications of constellation design and offered many suggestions. He also was a wonderful collaborator, helping me to create pages of information from small discussions.

Portions of the work on the physics based algorithm were studied thanks to an undergraduate, Tash Bosanac, who helped me to keep up with the pace during the last semester. The work was completed as part of the Undergraduate Research Opportunity Program. She found valuable references and made significant advances in the geolocation component which helped me move forward with the latter parts of the algorithm.

My attendance at MIT was supported by my parents and supported financially by my grandparents, Joseph and Elizabeth Bragg. I cannot repay their kindness, so I offer my thanks. They do not really know how much the opportunity opened proverbial doors (and windows) to help me move forward in my field.

A big thank you goes to my friends, Josef Bogosian and Zachary Folcik, who heard me babble endlessly about things I'm sure they don't understand or care about. From hockey games, parties, and Six Flags, we maintained a level of sanity in an insane world, which was the only reason I was able to finish my thesis. Thank you.

Finally, I would like to thank my husband, Tommy, for his support and for his ear (which is probably bleeding by now). His support was invaluable during the long days of taking too many classes and especially when I was entirely too frustrated to keep going.

I'm glad that I got to complete this challenging part of my life independently, quickly, and with a little bit of help from my family and friends. Thank you!

Contents

List of Figures

List of Tables

Chapter 1

Introduction

1.1 Thesis Objective

Above all, a tsunami early-warning and detection system must serve the people it was created to protect. As such, it must be reliable, efficient, and accurate. Microwave radiometers have a variety of uses including measuring atmospheric water vapor content, sea temperature, sea ice concentration, snow cover, atmospheric rain rate, soil moisture, ocean winds, and ice types [Ulaby, 1981]. Radiometers have improved by expanding the uses of measurements and increasing measurement accuracy. As the technology in the satellite sensors' ability to detect Earth phenomena progresses, the advancement can be used for other purposes, like tsunami detection. Microwave radiometer technology can be applied to the area of tsunami detection to improve warning accuracy and reaction time.

Tsunami have affected human cultures for millennia. Their destructive force has notoriety in almost every civilization that borders the sea. These civilizations have documented the changes that take place after tsunami and how it effected them socially and economically. For most, tsunami are a dangerous threat that has no warning, cannot be predicted, and result in significant casualties and loss of life.

Currently, the world relies on buoys and their connection to pressure sensors on the ocean's bottom to detect tsunami. The purpose of this thesis is to consider a new system to detect tsunami using a satellite constellation that carries microwave radiometers. The thesis will examine: (1) the satellite system architecture for detecting a tsunami from space, (2) the physical mechanisms of a tsunami, (3) explore the creation of a physics based simulation that will produce the tsunami and its visualization from the satellite radiometer system,

(4) discuss the creation of a comparison method to determine whether the new proposed system is actually more effective than the current system, and (5) will discuss the political, economical, and social difficulties of dealing with a tsunami.

1.2 Destruction/History

The first tsunami events are documented in several civilizations: 684 AD in Japan, 173 AD in China, 1480 BC in the eastern Mediterranean, 1821 Hawaii, 1788 Alaska, and 1562 Chile [Iida, 1967]. The volcanic island of Santorini erupted in 1500 BC, creating a Mediterranean Sea tsunami wave that crashed into Crete, which possibly led to the extinction of the Minoan civilization [Myles, 1985]. Large humanitarian disasters have been documented in recent years, including the Great Chile tsunami on May 22, 1960. This tsunami was detected and a warning was issued by the Seismic Sea Wave Warning System, which is operated by the Coast and Geodetic Society of the United States Department of Commerce. Although the Chilean tsunami was detected and had an issued warning, it still resulted in massive fatalities for two reasons.

First, the 1960 Chile tsunami was deadly because it was widespread. It was detected at 630 sites around the Pacific Ocean. Second, more than one tsunami wave hit land. The tsunami was generated by the last of over four dozen earthquakes occurring on the fault line running parallel to Chile's coast. The largest earthquake had a magnitude of 9.5 that caused the coastal lands to sink by two to four meters. Many people living near the coast put out to sea to escape the flooding that began. Within an hour, an eight meter high tsunami wave returned, traveling at a speed of 200 km per hour.

An hour later, an even higher eleven meter wave came ashore, although it moved slower than the first. Because of the time delay before the onslaught of the first wave and the gap between the first and second waves, many people left safe areas and were subsequently killed [Bryant, 2001]. Those who left immediately after the earthquake in boats were swept out to sea. The total loss of life in Chile is unknown but probably is between 5,000 and 10,000. The property damage in Chile alone was $417 million. Over the next day, the tsunami waves swept across the Pacific, killing more than 2,231 and damaging property in many countries. Although the warnings were issued and were accurate, the tsunami's behavior and consecutive waves were still very difficult to predict and protect against. The

1960 Chilean tsunami triggered the international communities involved to form the Pacific Tsunami Warning Center.

Table 1.2.1: Largest Death Tolls from Tsunami across the Globe over the Last 2,000 Years

Date	Fatalities	Location
26 Dec 2004	297,248	Sumatra, Indonesia
01 Nov 1775	100,000	Lisbon, Portugal
27 Aug 1883	36,500	Krakatau, Indonesia
28 Oct 1707	30,000	Nankaido, Japan
05 Feb 1783	30,000	Messina, Italy
15 Jun 1896	27,122	Sanriku, Japan
20 Sep 1498	26,000	Nankaido, Japan
13 Aug 1868	25,674	Arica, Chile
27 May 1293	23,024	Sagami Bay, Japan
04 Feb 1976	22,778	Guatemala
29 Oct 1746	18,000	Lima, Peru
21 Jan 1917	15,000	Bali, Indonesia
21 May 1792	14,524	Unzen, Ariake Sea, Japan
24 Apr 1771	13,486	Ryukyu Archipelago, East China Sea
22 Nov 1815	10,253	Bali, Indonesia
May 1765	10,000	Guanzhou, South China Sea

Source: [NGD, 2007] and [Bryant, 2001]

Other significant and deadly tsunami have been felt across the globe in the past. Table 1.2.1 shows the tsunami with the largest death tolls in the last 2,000 years. The Sumatra tsunami of 2004 is by far the most deadly tsunami. It could be considered the world's first global disaster because it affected people in dozens of countries on two different continents [Athukorala and Resosudarmo, 2005]. The response to this disaster was global; many nations pulled together, contributing assistance in rebuilding the lives of those affected by the tsunami. However, the Indian Ocean region was hit hard because there was no warning for these communities. The Pacific Tsunami Warning Center detected the 9.0 magnitude earthquake and in 18 minutes issued an e-mail communication to those in European countries indicating they were not in danger. A second e-mail indicated the possibility of a tsunami that would affect the Indian Ocean region, but the warning was not heard because the countries at risk could not communicate effectively with their people.

No warning system was in place in the Indian Ocean at the time of the 2004 Sumatra tsunami. Even if the government received a warning, there was little infrastructure within each country to distribute the warning to coastal inhabitants. Overall, the tsunami highlighted the inability to communicate warnings quickly with those living in threatened zones.

No matter how effective a disaster warning system is, the critical factor is the ability of a nation to warn its citizens about a threat.

At hand when a tsunami occurs is the physics surrounding the tsunami and its waves. The structure of the earth's bedrock, how the tsunami was created, and the topography of the ocean floor all contribute to a particular tsunami's characteristics. It is therefore necessary that these factors are explored in order to understand a tsunami and its properties.

1.2.1 Earth Bedrock Structure and Topography of the Ocean

The earth is comprised of four main parts: crust, mantle, outer core, and inner core (see Figure 1.2.1). The crust is by far the thinnest, comprising 1.5% of the earth's total mass. The crust contains two types of material: granite and basalt. Under the continents, the crust may be more than 40 miles thick in places, with an average thickness of 20 miles, and is made up of light granite. Under the seas, the crust runs to a depth of three to nine miles and is largely composed of heavier basalt (see Figure 1.2.2). The crust is composed of a lighter material laying on top of a heavier core. The upper layer is called the sial because silicon and aluminum are the principal elements. The heavier one is called sima because it is composed of silicon and magnesium. The sial underlies continental land masses and the seas' foundation is mostly sima.

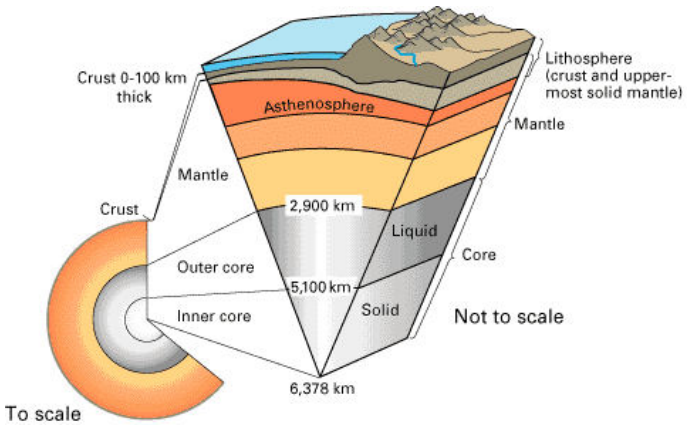

Figure 1.2.1: Cutaway view showing the internal structure of the earth [ATN, 2007].

There are two well defined depth levels within the sea. The first is the continental shelf, beginning where the continents end and has an average depth of 600 feet. It is a transitional region between land and the deep-ocean and is relatively shallow. As the shelf ends, there

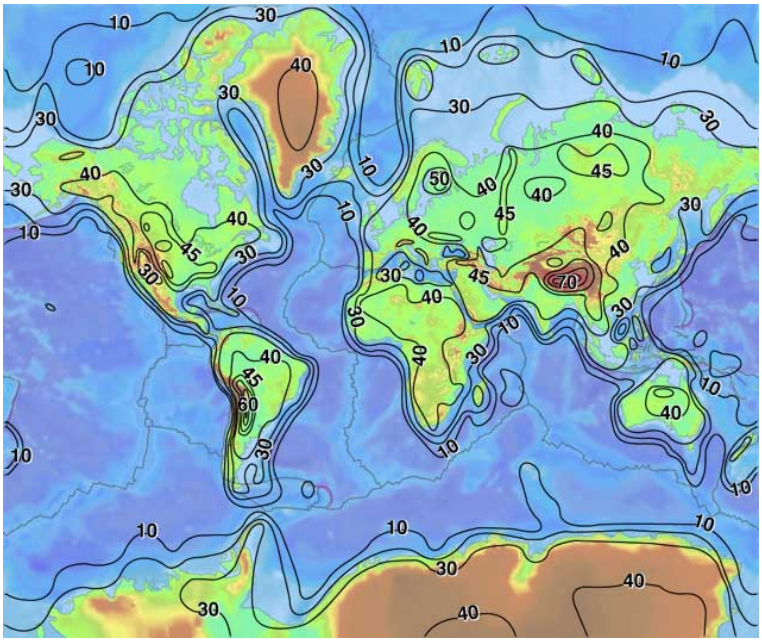

Figure 1.2.2: Contour map of the thickness of the earth's crust (in miles) [USG, 2007].

is a sudden increase in depth as the continental slope begins, leading downward toward the lowest portion of the ocean floor.

The second are the deep-ocean basins, having an average depth of 15,000 to 18,000 feet, beginning where the continental slope ends. Half the planet's total surface and five-sevenths of the sea-covered regions are comprised of deep-ocean basins [Myles, 1985]. The Pacific Ocean basin is so large that all land areas could fit within its area with considerable room remaining. This basin contains the world's greatest chains of volcanoes (known as the Ring of Fire). About 80% of the world's earthquakes occur within the Ring of Fire, because the basin's crust is unstable and is marked with deep trenches, cracks, fissures, and crevasses [Myles, 1985]. Due to the crust's instability, its features are in a constant state of change. These changes can create a deadly tsunami.

One of the changes of the crust involves the movement of plates, which are large sections of intact crust (see Figure 1.2.3). The theory of plate tectonics describes four types of movement of the earth's plates: sea-floor spreading, continental collision, subduction, and lateral transformation, where one plate slides past another moving in the opposite direction. Near trenches, the plates of the ocean floor are driven downward by the heavier and older

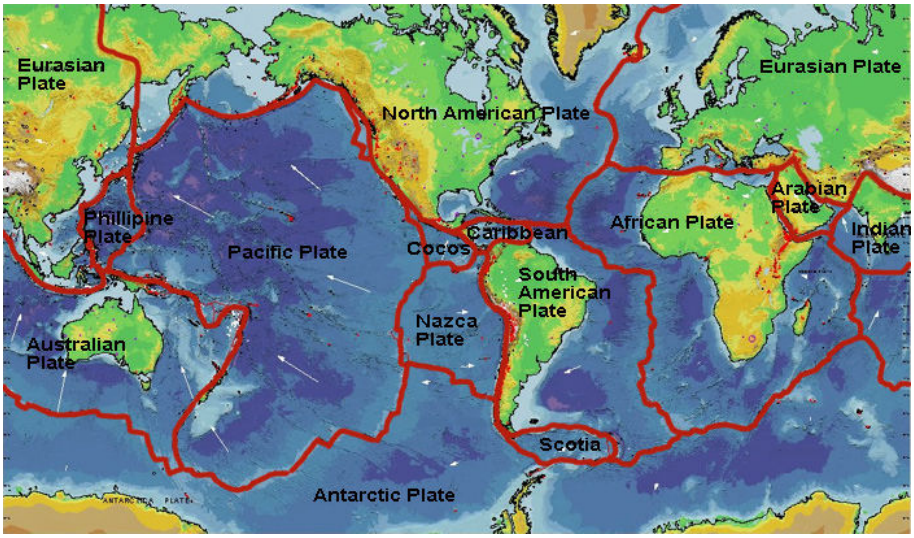

Figure 1.2.3: Plates in the crust of the earth [USG, 2007].

continental land mass plates. This means that each trench marks a subduction zone (see Figure 1.3.1 in Section 1.3 below).

1.3 Proposed Tsunami Detection & Early-Warning System

A tsunami has the potential for significant loss of life. To reduce this potential, tsunami warning systems have been created and deployed to protect some of the vulnerable coastal communities near subduction zones. Current warning systems consist of two networks: (1) a network of seismometers, and (2) a network of sea level gauges and bottom pressure recorders. The bottom pressure recorders communicate through an acoustic connection to ocean surface buoys, which send the data to processing centers through satellite communication uplinks.

This thesis introduces a new architecture for rapid and accurate tsunami detection. We propose employing passive microwave radiometers onboard a satellite constellation capable of continuous monitoring of potential tsunami source zones in the Pacific and Indian Oceans, including the Alaska-Aleutian, Japan-Kurile, Peru - Chilean, Central American, Sunda, and Cascadian Subduction Zones shown in Figure 1.3.1.

Radiometers can detect the presence of a tsunami through the tsunami's physical characteristics. The ability for the sensor to quickly and accurately detect a tsunami is important to maximize the available reaction time and also to minimize the number of false warnings

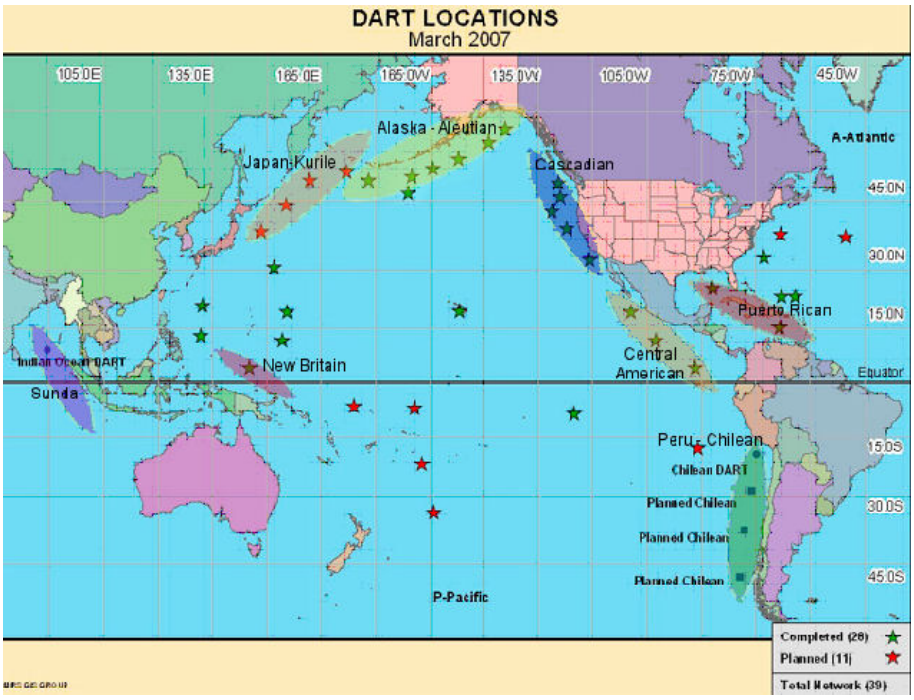

Figure 1.3.1: Sample of Global Subduction Zones and Locations of Completed and Planned DART II Buoys [Eisenman, 2007].

generated to coastal communities. False warnings are a major source of concern because they have a great economic and psychological impact. On 17 November 2003, the United States detected a small tsunami generated by an earthquake near Adak, Alaska, but because of the detection system's accuracy, the tsunami was determined not to be a threat to Hawaii. Detection system accuracy saved the Hawaiian state government estimated $68 million [Lautenbacher, 2005].

An event of similar magnitude in 1986 was very costly to the state of Hawaii. Hawaii's coastal areas were evacuated although the impending tsunami had a magnitude of only one foot. It caused no damage but the economic impact was great: an estimated $40 million. False warnings also tend to create havoc when a threat is real because the communities at risk are tired of heeding the warnings and evacuating, prompting some to stay behind, which puts them in great danger. This danger can be avoided with the announcement of only accurate warnings. Some error is always present, but the error should be minimized to protect those at risk.

1.4 Current System of Buoys

Currently, the United States has put monetary resources toward a comprehensive network of buoys to detect the presence of tsunami in the deep ocean. The buoy's components include a sensor called a tsunameter and a bottom pressure recorder. It sends its data with the help of Iridium, a satellite constellation, to be analyzed at the Pacific Tsunami Warning Center (PTWC) located in Hawaii. Buoy locations are shown in Figure 1.3.1. The buoy system is discussed with more detail in Section 3.4.

1.5 Early-Warning Detection System Objectives

Overall, the main point of the early-warning system for tsunami detection is to allow the end-users enough time to react to the threat in a community. The time allowed will depend upon the location of the generation source, the speed of the tsunami, and the location of the community at risk. This thesis proposes using a new system of spaceborne sensors which can monitor the entire ocean more efficiently.

1.6 History of the Detection Center Architecture

In 1949, the United States responded to a tsunami generated in the Aleutian Islands that devastated Hilo, Hawaii, by founding the Tsunami Warning Center in Ewa Beach, Hawaii. Until the Chilean tsunami of 1960, Japan used its own tsunami warning system, because they thought that tsunamis affecting Japan were all generated locally. However, the 1960 Chilean earthquake proved that any submarine earthquake in the Pacific Ocean region could spread ocean wide [Bryant, 2001]. In the wake of the international disaster, Pacific nations decided to coordinate efforts to prevent such loss of life. The United Nations Intergovernmental Oceanographic Commission (IOC) established the Intergovernmental Coordination Group for the Pacific Tsunami Warning System (ICG/PTWS) in 1968. The U.S. offered the Ewa Beach, Hawaii, Tsunami Warning Center as the operational headquarters for the Pacific Tsunami Warning System, and the facility was renamed the Pacific Tsunami Warning Center (PTWC).

In 1967, the West Coast & Alaska Tsunami Warning Center (WC/ATWC) was established in Palmer, Alaska, in response to the 1964 Alaskan earthquake and tsunami [NOAA,

2007]. In 1982, the WC/ATWC area of responsibility was enlarged to include the issuing of tsunami warnings to California, Oregon, Washington, and British Columbia for potential tsunamigenic earthquakes occurring in their coastal areas. Until 1996, the PTWC continued to issue tsunami warnings to these areas, when this responsibility was given to the WC/ATWC. Following 2004, the PTWC's responsibility areas were enlarged to include the Indian Ocean, the Caribbean, and adjacent regions until those areas have a dedicated tsunami warning center. As of 2004, the responsibilities of the PTWC and the West Coast Alaskan Tsunami Warning Center (WC/ATWC) have been divided as shown in Figure 1.6.1.

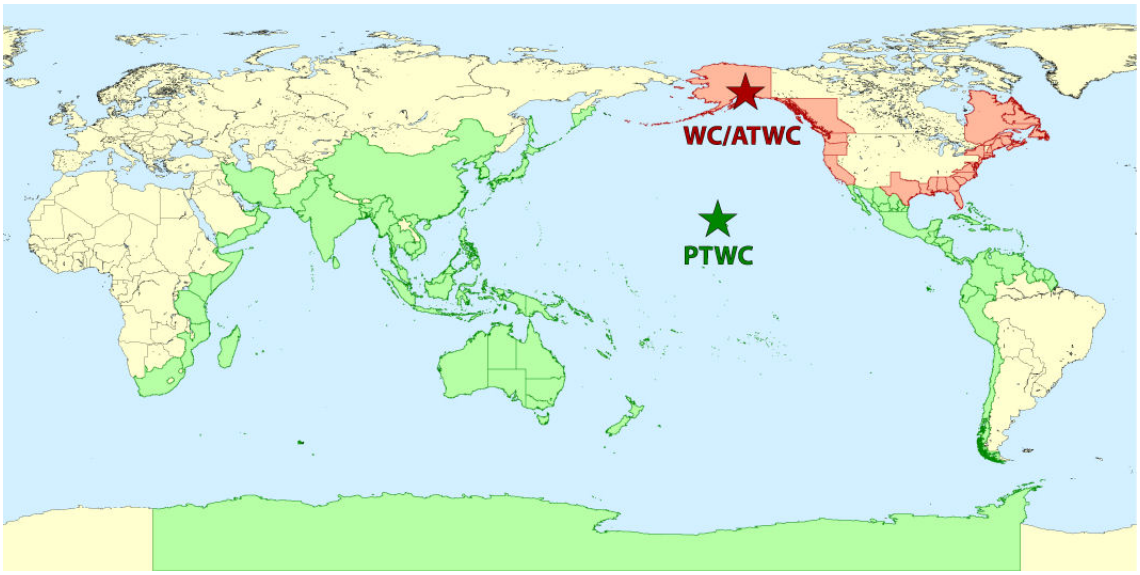

Figure 1.6.1: The two responsibility areas of the PTWC and the WC/ATWC [NOAA, 2007].

The National Tsunami Hazard Mitigation Program (NTHMP) of the United States was created to reduce *domestic* tsunami risks. In 2005, Congress appropriated $17.24 million in supplemental funding to enhance these efforts; they approved $9.82 million in 2006 and $21.66 million was requested for 2007 [GAO, 2006]. The National Oceanographic and Atmospheric Administration (NOAA) is currently using these funds to increase the ability to detect a tsunami by expanding its buoy network, from four in 2004 to thirty-nine total planned.

Internationally, additional tsunami warning systems have been created that will cover areas outside the Pacific region. The International Oceanographic Commission created the Indian Ocean Tsunami Warning and Mitigation System (IOTWS) after the Sumatra tsunami, which has operations similar to the PTWC. The biggest challenge of coordination

within the Indian Ocean region is the coordination and communication required to relay its threat to exposed communities. The Indian Ocean received its first buoy, deployed by NOAA in 2006, and is expected to get more buoys and also monitoring buoys with the help of several nations. Their locations and a schematic of a monitoring buoy is shown in Figure 1.6.2.

Figure 1.6.2: Locations of Planned Buoys in the Indian Ocean [Stone and Kerr, 2005]

1.7 Conclusion

Tsunami warning systems are not only useful, but are needed for natural disaster protection around the globe. This protection relies not only on the ocean's geological properties, but also on the communication and coordination of multiple agencies and governments. In

general, the early-warning and mitigation systems must be reliable and accurate, but also rely on accurate technology. Technology can be improved to increase the awareness of potential tsunami threats in the minimum amount of time. Applications must be expanded to allow the detection system to improve as technology progresses. Tsunami detection can and should be included in the expansion.

1.8 Thesis Overview

The remainder of the thesis analyzes the broad system and delves into the useful knowledge within each part of the system that contributes to the entire purpose: tsunami early-warning and detection. Chapter 2 discusses the physical properties of ocean wave propagation and how to recognize a wave's behavior. It also explains the difference in the behavior of a wave while it is in coastal areas and while it is in the deep ocean. Chapter 3 explains tsunami phenomenology, the specific characteristics of tsunami, and how a tsunami wave is different from other types of oceanic waves. It explains the methods currently in use to detect a tsunami. Some of these methods are post-hoc methods, but one in particular is designed to detect a tsunami before it strikes land and can warn coastal communities in danger. Chapter 4 gives the history and the fundamental background for microwave radiometry and how these sensors work. Then it describes basic radiometer architectures and how radiometer technology can be used to measure tsunami characteristics. This chapter also discusses the tsunami detection potential of radiometers.

Because we are proposing a new system to complete the tsunami detection task, the system will be described in detail. Chapter 5 describes how space-based sensors can be maximized by utilizing a satellite constellation that will observe the whole ocean. Chapter 6, the crux of the thesis, describes how the analytical evaluation of the sensor's data will be collected, corrected, and assembled for the end-user. Chapter 7 compares the current DART II buoy system with the new, proposed space-based radiometer system. Chapter 8 briefly illustrates the system's early-warning capability and disaster risk in general. Finally, Chapter 9 states the conclusions from this research and makes recommendations for future work.

Chapter 2

Ocean Wave Propagation

In order to understand how a tsunami will affect the ocean's surface, we must understand the random waves present on the surface of the ocean, without the tsunami. The purpose of this chapter is to mathematically describe the random harmonic waves and their behavior. The random nature of waves is shown in Figure 2.0.1, which looks very similar to Figure 6.1.2(a) shown later in Chapter 6.

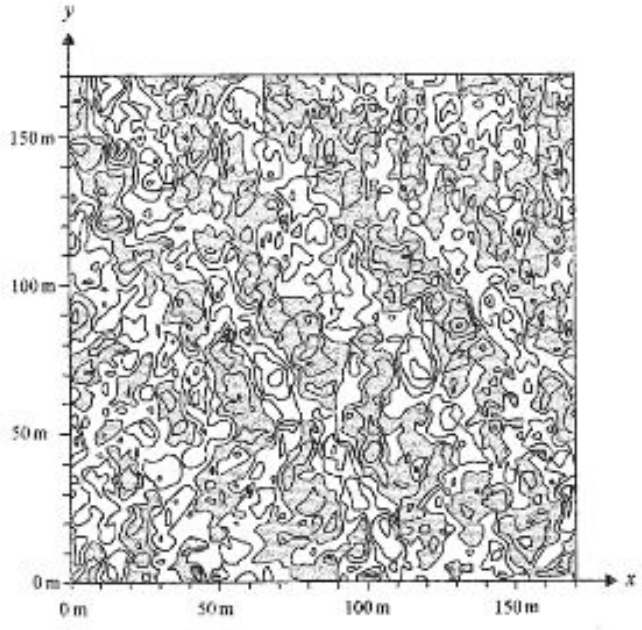

Figure 2.0.1: Sea surface elevation as a function of horizontal coordinates at a moment in time (the contour line interval is 0.2 m; shaded areas are below mean sea level) [Holthuijsen, 2007]

The equations outlined here describe the motion of waves and therefore, tsunami. This motion model can be utilized later to continue the work of this document by creating a simulation that includes the models of ocean waves. This can help the system become more useful by increasing the understanding of ocean waves and the mechanisms that determine their motion.

2.1 Linear Wave Theory in Oceanic Waters

The following theory is described in detail by Holthuijsen [2007]. The derivations are replicated here to go through the overall equations governing the waves of the sea. The basic theory behind waves in deep water is the linear theory, which only applies when gravitation is the only external force [Holthuijsen, 2007]. The linear theory is based on mass and momentum balance equations, which can be result in the Laplace and Bernoulli equations. For the linear theory to apply, the waves' amplitude must be small compared to the wavelength and the water depth.

Water is assumed to be an ideal fluid: it is considered incompressible, has a constant density, and has no viscosity. Aside from the previous assumption that water is only subjected to the external force of gravitation, there are two additional requirements. Water particles may neither leave the surface or penetrate the bottom and the water body must also be continuous, which will exclude complications associated with air bubbles, wind pressure, and wave variation, or breaking waves.

2.1.1 Balance equations

Two balance equations are used to describe a wave's motion: a mass balance theory and a momentum balance theory [Holthuijsen, 2007]. Since the derivations are similar, the equations will be derived for an arbitrary property, μ. The derivations found here are outlined by Holthuijsen [2007], which goes into greater explanation than shown here.

Consider a fluid in a Cartesian reference frame (x- and y-axes form the horizontal plane and the z-axis is vertically upwards). The fluid transports the property, μ, through a volume

Δx Δy Δz. The property's volume will be balanced over a time interval ,Δt:

$$\begin{aligned} &\textit{storage of } \mu \textit{ during } \Delta t = \\ &\quad \textit{net import of } \mu \textit{ during } \Delta t + \\ &\quad \textit{local production of } \mu \textit{ during } \Delta t \end{aligned} \tag{2.1.1}$$

By finding the difference between the quantity of μ remaining at the end of the time interval and the quantity of μ at the beginning of the time interval (in short, the net quantity of μ remaining), we can find the storage term:

$$\begin{aligned} &\textit{storage of } \mu \textit{ during } \Delta t \\ &\quad = \left(\mu\ \Delta x\ \Delta y\ \Delta z\ + \frac{\partial(\mu\ \Delta x\ \Delta y\ \Delta z)}{\partial t}\ \Delta t \right) -\ \mu\ \Delta x\ \Delta y\ \Delta z \\ &\quad = \frac{\partial \mu}{\partial t}\ \Delta x\ \Delta y\ \Delta z \end{aligned} \tag{2.1.2}$$

We can solve these equations for each direction. To find the net import in the x-direction, for particles with a velocity component equal to u_x, the balance equation must be rewritten. The storage of μ is conceptually the import through the left hand side of the volume (having an area of $\Delta y\ \Delta z$) minus the export through the right hand side of the volume. If μ is transported with the velocity of the water particles, the net import in the x-direction is:

$$\begin{aligned} &\textit{net import of } \mu \textit{ in the } x - \textit{direction during } \Delta t \\ &\quad =\ \textit{import}\ -\ \textit{export} \\ &\quad =\ \mu\ u_x\ \Delta y\ \Delta z\ \Delta t\ - \left(\mu\ u_x\ + \frac{\partial(\mu\ u_x)}{\partial x}\ \Delta x \right) \Delta y\ \Delta z\ \Delta t \\ &\quad =\ -\frac{\partial(\mu\ u_x)}{\partial x}\ \Delta x\ \Delta y\ \Delta z\ \Delta t \end{aligned} \tag{2.1.3}$$

Similarly, the net imports in the y- and z-directions during the interval Δt are:

$$\begin{aligned} &\textit{net import of } \mu \textit{ in the } y - \textit{direction during } \Delta t \\ &\quad =\ -\frac{\partial(\mu\ u_y)}{\partial y}\ \Delta x\ \Delta y\ \Delta z\ \Delta t \end{aligned} \tag{2.1.4}$$

$$\begin{aligned} &\textit{net import of } \mu \textit{ in the } z-\textit{direction during } \Delta t \\ &= -\frac{\partial(\mu\ u_z)}{\partial z}\ \Delta x\ \Delta y\ \Delta z\ \Delta t \end{aligned} \tag{2.1.5}$$

The local production of μ in the volume, during interval Δt is:

$$\begin{aligned} &\textit{local production of } \mu \textit{ during } \Delta t \\ &= S\ \Delta x\ \Delta y\ \Delta z\ \Delta t \end{aligned} \tag{2.1.6}$$

where S is the production of μ per unit time, per unit volume. Equations 2.1.2 through 2.1.6 can be plugged into Equation 2.1.1 to give:

$$\begin{aligned} &\frac{\partial \mu}{\partial t}\ \Delta x\ \Delta y\ \Delta z\ \Delta t \\ &\quad = -\frac{\partial(\mu\ u_x)}{\partial x}\ \Delta x\ \Delta y\ \Delta z\ \Delta t\ -\frac{\partial(\mu\ u_y)}{\partial y}\ \Delta x\ \Delta y\ \Delta z\ \Delta t \\ &\quad = -\frac{\partial(\mu\ u_z)}{\partial z}\ \Delta x\ \Delta y\ \Delta z\ \Delta t\ + S\ \Delta x\ \Delta y\ \Delta z\ \Delta t \end{aligned} \tag{2.1.7}$$

Simplifying leads us to the balance equation for μ per unit volume, per unit time:

$$\frac{\partial \mu}{\partial t} + \frac{\partial(\mu\ u_x)}{\partial x} + \frac{\partial(\mu\ u_y)}{\partial y} + \frac{\partial(\mu\ u_y)}{\partial y} = S \tag{2.1.8}$$

The first term on the left-hand side of Equation 2.1.8 represents the local rate of change of μ. The three following terms represent the effect of transportation and are called advective terms. Lastly, the right-hand side term is the source term. It represents the generation or dissipation of μ. Following Holthuijsen [2007], the general balance equations derived in this section will be explored further by breaking them down into the specific equations for mass, continuity, and momentum.

Mass balance and Continuity equations

If the mass density of sea water is $\mu = \rho \approx 1025 \frac{kg}{m^3}$, we can substitute it into Equation 2.1.8, and obtain the mass balance equation:

$$\frac{\partial \rho}{\partial t} + \frac{\partial(\rho\ u_x)}{\partial x} + \frac{\partial(\rho\ u_y)}{\partial y} + \frac{\partial(\rho\ u_y)}{\partial y} = S_\rho \tag{2.1.9}$$

Since the mass density is assumed to be constant and the production of water is assumed to be zero (i.e., $S_\rho = 0$), we can find the continuity equation:

$$\frac{\partial u_x}{\partial x} + \frac{\partial u_y}{\partial y} + \frac{\partial u_z}{\partial z} = 0 \tag{2.1.10}$$

The above continuity equation is a linear equation in terms of the water particle velocities u_x, u_y, and u_z.

Momentum balance

As Holthuijsen [2007] explains, the momentum density of the water, μ is equal to the mass density of water time the velocity of the water particles: $\mu = \rho\vec{u} = (\rho u_x, \rho u_y, \rho u_z)$. This balance equation is a vector equation which requires three component equations. By substituting $\mu = \rho u_x$ into Equation 2.1.8, the x-component's balance equation is found:

$$\frac{\partial(\rho u_x)}{\partial t} + \frac{\partial(u_x \rho u_x)}{\partial x} + \frac{\partial(u_y \rho u_x)}{\partial y} + \frac{\partial(u_z \rho u_x)}{\partial z} = S_x \tag{2.1.11}$$

where S_x is the momentum's production in the x-direction. The production of momentum is defined from Newton's second law of mechanics as the force acting on the volume. This means that we can rewrite Equation 2.1.11 as

$$\frac{\partial(\rho u_x)}{\partial t} + \frac{\partial(u_x \rho u_x)}{\partial x} + \frac{\partial(u_y \rho u_x)}{\partial y} + \frac{\partial(u_z \rho u_x)}{\partial z} = F_x \tag{2.1.12}$$

where F_x is the body force in the x-direction per unit volume. The advective terms (the second, third, and fourth terms on the left hand side of Equation 2.1.12) contain the velocities in quadratic combinations which are nonlinear [Holthuijsen, 2007]. In order for the theory to remain linear, the nonlinear terms must be removed, which reduces the momentum balance equation (Equation 2.1.12) to the linearized momentum balance equation:

$$\frac{\partial(\rho u_x)}{\partial t} = F_x \tag{2.1.13}$$

F_x is due to the horizontal pressure gradient ∂p / ∂x in the water, which is due to the external force of gravity. The total horizontal force on the volume $\Delta x\ \Delta y\ \Delta z$ is equal to the change in pressure-induced force between the left-hand side and right-hand side of the

volume:

$$p\ \Delta y\ \Delta z - \left(p + \frac{\partial p}{\partial x}\Delta x\right)\Delta y\ \Delta z \tag{2.1.14}$$

Per unit volume, this is:

$$F_x = -\frac{\partial p}{\partial x} \tag{2.1.15}$$

If the mass density of water is constant, then the momentum balance equation for the x-direction becomes:

$$\frac{\partial u_x}{\partial t} = -\frac{1}{\rho}\frac{\partial p}{\partial x} \tag{2.1.16}$$

The linearized momentum balance equations for the x-, y-, and z-directions are, respectively:

$$\frac{\partial u_x}{\partial t} = -\frac{1}{\rho}\frac{\partial p}{\partial x} \qquad \frac{\partial u_y}{\partial t} = -\frac{1}{\rho}\frac{\partial p}{\partial y} \qquad \frac{\partial u_z}{\partial t} = -\frac{1}{\rho}\frac{\partial p}{\partial z} - g \tag{2.1.17}$$

Boundary conditions

Specific boundary conditions must be found by solving the continuity and momentum balance equations. Boundary conditions are based on the kinematics and dynamics of the water particles. One dynamic and three kinematic boundaries must be considered: the ocean bottom, ocean surface, and lateral boundaries on each side of the volume. The lateral boundaries at the up-wave side and down-wave side of the x-domain will be described in a two-dimensional frame. This is because we assume that the wave has infinitely long crests in the y-direction, with no variation.

The kinematic boundary condition at the ocean surface is that particles may not leave the surface. The linearized velocity of the particle normal to the surface is equal to the speed of the surface in that direction. This is expressed as:

$$u_z = \frac{\partial \eta}{\partial t} \qquad at\ z = 0 \tag{2.1.18}$$

where η is the surface elevation, measured vertically upwards from $z = 0$ [Holthuijsen, 2007]. The kinematic boundary condition at the ocean bottom is that particles may not penetrate the fixed, horizontal bottom:

$$u_z = 0 \qquad at\ z = -d \tag{2.1.19}$$

where d is the water's depth. To ensure that the wave is a free wave that is only subject to the external force of gravity, the atmospheric pressure at the water surface is constant. This is the dynamic surface boundary condition:

$$p = 0 \qquad at\ z = 0 \tag{2.1.20}$$

2.2 Velocity Potential Function

As Holthuijsen [2007] describes, the velocity potential function, $\phi = \phi(x, y, z, t)$, is used to solve the above balance equations and the boundary conditions. It is defined as the a function that has spatial derivatives are equal to the velocities of the water particles:

$$\phi(x, y, z, t)\ defined\ such\ that\ u_x = \frac{\partial \phi}{\partial x},\ u_y = \frac{\partial \phi}{\partial y},\ and\ u_z = \frac{\partial \phi}{\partial z} \tag{2.2.1}$$

The equation can only exist if the water particles' velocities do not rotate. Then the continuity equation (Equation 2.1.10) in terms of the velocity potential function, ϕ, can be found by substituting the above equation into Equation 2.1.10, giving:

$$\frac{\partial^2 \phi}{\partial x^2} + \frac{\partial^2 \phi}{\partial y^2} + \frac{\partial^2 \phi}{\partial z^2} = 0 \tag{2.2.2}$$

Equation 2.2.2 is called the Laplace equation. It is derived from the mass balance equation, but mass and mass density has been eliminated from the equation.

To express the kinematic boundary conditions at the surface and at the bottom in terms of the velocity potential function, the derivatives of Equation 2.2.1 must be substituted into Equations 2.1.19 and 2.1.20:

$$\frac{\partial \phi}{\partial z} = \frac{\partial \eta}{\partial t} \qquad at\ z = 0 \tag{2.2.3}$$

$$\frac{\partial \phi}{\partial z} = 0 \qquad at\ z = -d \tag{2.2.4}$$

The three momentum balance equations can be expressed in terms of ϕ. For momentum in the x-direction, the result is:

$$\frac{\partial}{\partial t}\left(\frac{\partial \phi}{\partial x}\right) = -\frac{1}{p}\frac{\partial p}{\partial x} \tag{2.2.5}$$

Which equals:

$$\frac{\partial}{\partial x}\left(\frac{\partial \phi}{\partial t}+\frac{p}{\rho}\right)=0 \tag{2.2.6}$$

The gravitational term, gz, from Equation 2.1.17 can be added because it will disappear after taking the derivative in the x- and y-directions [Holthuijsen, 2007].

$$\begin{aligned}
\frac{\partial}{\partial x}\left(\frac{\partial \phi}{\partial t}+\frac{p}{\rho}+gz\right)&=0\\
\frac{\partial}{\partial y}\left(\frac{\partial \phi}{\partial t}+\frac{p}{\rho}+gz\right)&=0\\
\frac{\partial}{\partial z}\left(\frac{\partial \phi}{\partial t}+\frac{p}{\rho}+gz\right)&=0
\end{aligned} \tag{2.2.7}$$

Because the sum of terms between the brackets appears in each equations, the sum is not a function of either x, y, or z. It is an arbitrary function of time t. If we solve for $f(t)=0$, we get the linearized Bernoulli equation for linear flow as shown in Holthuijsen [2007]:

$$\frac{\partial \phi}{\partial t}+\frac{p}{\rho}+gz=0 \tag{2.2.8}$$

Taking the linearized Bernoulli equation at the surface $z=\eta$, with $p=0$, allows the dynamic boundary condition to also be expressed in terms of ϕ:

$$\frac{\partial \phi}{\partial t}+g\eta=0 \qquad at\ z=0 \tag{2.2.9}$$

where the surface elevation, η, is taken into account, but the boundary condition is applied at $z=0$. The above equations and boundary conditions are summarized in Figure 2.2.1 from Holthuijsen [2007].

The Laplace equation and the kinematic boundary conditions are used in the following section to obtain the solution for the velocity potential. The momentum balance equations and the boundary conditions are not needed to do this exercise. The linearized Bernoulli equation and the linearized boundary condition will be used to obtain expressions for some of the dynamic aspects of the waves.

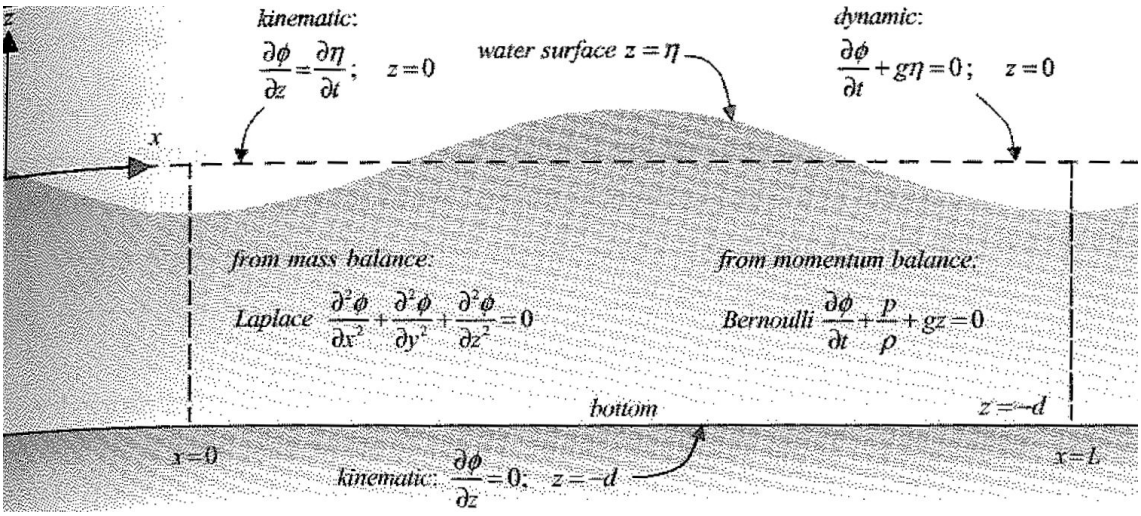

Figure 2.2.1: The basic equations and boundary conditions for the linear wave theory in terms of the velocity potential, ϕ [Holthuijsen, 2007]

2.3 Propagating harmonic waves

An analytical solution to the Laplace equation with the stated boundary conditions (Equations 2.2.2 and 2.2.9) is a harmonic wave propagating in the positive x-direction:

$$\eta(x,t) = a\sin(\omega t - kx) \tag{2.3.1}$$

where η is the surface elevation, ω is the radian frequency, k is the wave number, and a is the amplitude [Holthuijsen, 2007]. The solution has the following velocity potential function:

$$\phi = \hat{\phi}\cos(\omega t - kx) \quad where \quad \hat{\phi} = \frac{\omega a}{k}\frac{\cosh\left[k(d+z)\right]}{\sinh(kd)} \tag{2.3.2}$$

Here is where the harmonic wave is introduced to the linear wave theory of oceanic waves. It is based on the small approximation, meaning that the amplitude of the wave should be small compared with the wavelength and water depth (see Section 2.1).

If the position of the crest of the wave, x, has a constant phase, then the equation can be manipulated to find the forward speed of the crest of the wave.

$$\frac{\partial(\omega t - kx)}{\partial t} = 0 \quad or \quad \frac{\partial(\omega t)}{\partial t} - \frac{\partial(kx)}{\partial x}\frac{dx}{dt} = 0 \quad \omega - k\frac{dx}{dt} = 0 \tag{2.3.3}$$

Therefore, the phase speed $c = dx/dt$, from Equation 2.3.3 is:

$$c = \frac{dx}{dt} = \frac{\omega}{k} \tag{2.3.4}$$

The velocity potential function, ϕ, of Equation 2.3.2 did not consider the wave's dynamic aspects, like the Bernoulli equation or the dynamic surface boundary condition [Holthuijsen, 2007]. This implies that ϕ is based solely on the Laplace equation and the kinematic boundary conditions. The expression for ϕ applies to both free and forced waves, as long as the surface wave is harmonic, using Equation 2.3.1.

Particle velocity

Particle velocities can be obtained from the velocity potential ϕ, by using its definition: the spatial derivatives of ϕ are the velocity components $\partial\phi/\partial x = u_x$ and $\partial\phi/\partial z = u_z$, so that, from Equation 2.3.2 the particle velocities are given by:

$$\begin{aligned} u_x &= \omega a \frac{\cosh\left[k(d+z)\right]}{\sinh(kd)} \sin(\omega t - kx) \\ u_y &= 0 \\ u_z &= \omega a \frac{\sinh\left[k(d+z)\right]}{\sinh(kd)} \cos(\omega t - kx) \end{aligned} \tag{2.3.5}$$

Because the harmonic wave propagates in the x-direction, the velocity in the y-direction is zero. This is an orbital velocity because it corresponds to motion of the particles in closed, circular, or elliptical orbits for deep water [Holthuijsen, 2007]. In deep water, when $kd \to \infty$, the expressions for the amplitudes of the velocity components $\hat{u_x}$ and $\hat{u_z}$ reduce to:

$$\hat{u_x} = \hat{u_z} = \omega a e^k \quad \text{for deep water} \tag{2.3.6}$$

The total velocity is independent of time because the velocity components are equal:

$$u = \sqrt{u_x^2 + u_z^2} = \omega a e^k z \quad \text{for deep water} \tag{2.3.7}$$

For deep water, the wave-induced velocities decrease exponentially with the distance to the surface. At the surface, the total orbital velocity is:

$$u = \omega a \tag{2.3.8}$$

2.3.1 Capillary waves

This section is adapted from the explanations on capillary waves by Holthuijsen [2007]. The pressure on the surface is assumed to be constantly zero because it is assumed that the wave is free of external forces other than gravity. However, wind is an external force that plays a significant role. For very small waves (having a centimeter of length), the water surface itself contains a force that acts normal to the surface, due to surface tension. Surface tension has a component normal to the surface if that surface is curved [Holthuijsen, 2007].

$$p_{\text{surface tension}} = -\tau_s \frac{\partial^2 \eta}{\partial x^2} \tag{2.3.9}$$

where τ_s is the surface-tension coefficient. For a harmonic wave, this can be written as:

$$p_{\text{surface tension}} = \tau_s k^2 \eta \tag{2.3.10}$$

It can be included with the dynamic surface boundary condition (see Equation 2.2.9), with the result that:

$$\frac{\partial \phi}{\partial t} + \left(g + \frac{\tau_s k^2}{\rho} \right) \eta = 0 \quad at\ z = 0 \tag{2.3.11}$$

The surface boundary conditions are the same as the dynamic surface boundary condition for a free wave, except that the dynamic surface boundary condition's gravitational acceleration g was replaced with $g + \frac{\tau_s k^2}{\rho}$. Then, the dispersion relationship becomes:

$$\omega^2 = \left(g + \frac{\tau_s k^2}{\rho} \right) k \tanh(kd) \tag{2.3.12}$$

and the phase velocity becomes:

$$c = \sqrt{\frac{g + \frac{\tau_s k^2}{\rho}}{k} \tanh(kd)} \tag{2.3.13}$$

For a wave length of 0.017 m, the surface tension term is approximately equal to the gravitational acceleration. For shorter waves, the effect of surface tension will increase. Waves dominated by surface tension are called capillary waves and can be important for remote sensing because of the applications which operate in a small range (centimeter level). It is the modulation of capillary waves by the longer waves that create the image of wind waves on radar [Holthuijsen, 2007].

2.4 Wave modeling for arbitrary cases

Wave predictions are usually required when a situation is not ideal. The ideal circumstances outlined in previous sections do not entirely explain wave behavior because realistic situations are not ideal. A random-phase/amplitude model, explained in Section 2.4.1, will be assumed to model waves in arbitrary cases. Wave prediction will be based on predicting individual components of independent waves. These components include all effects of generation, wave-wave interaction, and dissipation that a wave encounters. Then the independent wave components are predicted individually by investigating the spectral density $E = E(f, \theta)$ of each wave component as it varies in time (t) and horizontal position (x, y): $E(f, \theta) = E(f, \theta; x, y, t)$ [Holthuijsen, 2007].

2.4.1 Random-phase/amplitude model

The random-phase/amplitude model is the basic way to describe the moving surface elevation of a wave, $\eta(t)$, where the surface elevation is the sum of a large number of harmonic waves. Harmonic waves have a constant amplitude and a phase chosen randomly for each point in time:

$$\eta(t) = \sum_{i=1}^{N} \underline{a}_i \cos(2\pi f_i t + \underline{\alpha}_i) \tag{2.4.1}$$

where N is a large number of frequencies and $\underline{a}_i$ is amplitude and $\underline{\alpha}_i$ is phase [Holthuijsen, 2007]. The underlined amplitude and phase factors indicate that they are random variables, which are fully characterized with respective probability density functions. The phase at each frequency, f_i, is uniformly distributed between 0 and 2π:

$$p(\alpha_i) = \frac{1}{2\pi} \quad \text{for} \quad 0 < \alpha_i \leq 2\pi \tag{2.4.2}$$

and the amplitude, $\underline{\alpha}_i$, is at each frequency:

$$p(a_i) = \frac{\pi}{2}\frac{a_i}{\mu_i^2}\exp\left(-\frac{\pi a_i^2}{4\mu_i^2}\right) \quad \text{for} \quad a_i \geq 0 \tag{2.4.3}$$

where μ_i is the expected value of the amplitude $\mu_i = E\underline{a}_i$. The exact values of the frequencies are not important as long as they are densely distributed along the frequency axis and they are in the correct range for waves at sea (typically 0.05 - 1.0 Hz) [Holthuijsen, 2007].

2.4.2 Energy balance equation

Holthuijsen [2007] explains how to find the energy balance equation for the wave. The evolution of the energy density of each wave component can be found by integrating the energy evolution equation while propagating with the group velocity along a wave ray:

$$\frac{dE(f,\theta;x,y,t)}{dt} = S(f,\theta;x,y,t) \tag{2.4.4}$$

where the left-hand side term is the rate of change of the energy density, and $dx/dt = c_{g,x}$ and $dy/dt = c_{g,y}$ (where $c_{g,x}$ and $c_{g,y}$ are the $x-$ and $y-$ components of the group velocity of the wave component), and frequency and direction are constant because we are investigating the wave in deep water [Holthuijsen, 2007]. The right-hand side source term includes generation effects, wave-wave interactions, and dissipation. This method works for deep water because the wave rays are straight lines or great-circles. Equation 2.4.4 should only be integrated along these straight lines.

However, integrating the source term is difficult because the energy densities are not completely known, so the Lagrangian approach cannot be used for computations. The Eulerian approach treats the energy balance of the waves on a regular geographic grid successfully. It is explained thoroughly by Holthuijsen [2007] and will not be discussed here.

2.4.3 Wave propagation and swell

Surface gravity waves' linear theory shows that the propagation speed of the wave energy depends on the frequency of the considered wave component in deep water[Holthuijsen, 2007]. A low-frequency wave's energy travels faster than that of high-frequency waves. If

an initially random wave field moves in fields of more regular waves, it will disintegrate. This process is called frequency-dispersion. The waves become more and more regular, but they also change from short-crested to long-crested because the waves travel in a multitude of directions and the initial wave fields disintegrate into these directions. This process is called direction-dispersion. Waves dispersed across the ocean are called "swell".

Frequency- and direction-dispersion both imply that the energy spectrum at a geographic point has a narrow frequency band and a particular direction [Holthuijsen, 2007]. The narrow spectrum of energy is a discrete subset of the broader energy spectrum. Waves at a distance from where the swell began have a smaller amplitude because of dispersion; no dissipation is involved. The simple model of frequency- and direction-dispersion has been verified by tracking swell across the ocean [Holthuijsen, 2007].

2.4.4 Generation by wind

A model for a wave's generation is the instability of the water surface layer where the wind generates a current. Two fluids with different speeds will generate instabilities at their interface if the densities and speeds differ enough [Lamb, 1932]. This theory is apparent when viewing an area of water. As wind blows over still water, small and short waves appear. Slowly, these waves become longer and higher. In modeling the wave's generation, the small waves can be imposed. Another theory by Phillips [1957] poses that waves are generated by resonance between propagating wind-induced pressure waves (i.e., air pressure) at the water surface and freely propagating water waves. This theory assumes that the wind-induced surface pressure is a natural aspect of the wind itself, without the waves' influence [Holthuijsen, 2007]. This assumption is not entirely correct because the waves' influence will increase as the waves evolve.

In the theoretical model by Miles [1957], he found that the air pressure at the water surface attains a maximum on the windward side of the wave crest and a minimum on the leeward side of the wave crest. This implies that the wind pushes the water surface down where the wave surface is moving down and consequently, pushes up where the wave surface is moving up. This out-of-phase coupling between pressure and motion transfers energy to the waves. The air pressure's effect causes the energy to continually be added, making them grow. In making them grow, the mechanism becomes more effective [Holthuijsen, 2007].

2.4.5 Wave-wave interactions

This is the second mechanism affecting wave growth in deep water, because it allows waves to transfer energy among each other, by resonance. These interactions are non-linear. In deep water, the resonance conditions require a pair of wave components to interact with another pair. This is possible because each pair of waves will create a diamond pattern of crests and troughs, which has its own wave length, speed and direction [Holthuijsen, 2007]. For resonance, the two pairs must have the same wave length, speed, and direction. If the frequency, wave number and direction of one diamond pattern coincide with those of another diamond pattern, then energy is transferred amongst the four free components involved. A set of these four wave components is called a quadruplet and the interactions are called quadruplet wave-wave interactions. Unlike wind generation, the interactions only transfer energy. No energy is added or removed from the quadruplet as a whole [Holthuijsen, 2007].

Quadruplet interactions transfer a significant fraction of the wind input from the mid-range frequencies to lower frequencies and a small fraction to higher frequencies. At high frequencies, white-capping dissipates the energy. At low frequencies, energy is absorbed without significant dissipation. The energy of low frequencies grows, allowing these frequencies to dominate the evolution of the overall frequency spectrum. Including the effects of quadruplet interactions is important because of the changes in energy; however, the computation is complex and costly because there are many quadruplets [Holthuijsen, 2007].

Aside from the linear theory in deep water, there is also a theory for coastal waters. The changes in the theory highlight the transfiguration of the tsunami wave as it travels to shore.

2.5 Linear Wave Theory in Coastal Waters

When ocean waves enter coastal waters, the waves' amplitude and direction will change due to the limited water depth. There are several types of phenomena that govern the specific changes of the waves: shoaling, refraction, diffraction, and reflection. Shoaling is the changing in the direction of propagation, or in the longitudinal direction, because the group velocity changes (see Equation 3.1.1). It results in increased wave height near the coast. Refraction is the directional changes of the wave because the phase speed changes. Refraction will turn the wave toward shallower water. Diffraction is a rapid change in

amplitude, causing the waves to turn into areas with lower amplitude. Reflection is the echo of waves off the coastline and its geographical features. All of these properties are caused because the wave moves into shallow water. They can be explained, modeled, and analyzed with the linear wave theory unless the waves are too steep or not in very shallow water. When these two exceptions are present, the waves must be analyzed with a nonlinear theory, such as a Boussinesq model [Voit, 1987], which will not be explained here.

2.5.1 Shoaling

In general, shoaling is a process that involves two factors. The first factor dominates when the wave first moves into shallow water (generally as the wave reaches the continental shelf). The wave height will decrease because the wave slows down until its velocity to equal the group velocity. This factor decreases the wave height to about 90% of its deep water height by the time the depth is one-sixth of the wavelength and dominates until the depth is one-sixth of the wavelength.

The second factor occurs because the waves' wavelength shortens as it enters shallow water. As the wave's velocity decreases, its crests move closer together creating a shorter wavelength. Because the energy must be conserved, its wave height must increase. Therefore, the waves become higher near the shore. A wave that was barely perceptible in deep water may reach a height of several meters in shallow water. This factor predominates after the depth is one-sixth of the wavelength. This effect causes the waves' height to increase to a large value close to the shore. The physics equations that explain the effect of shoaling are explained below and are adapted from Holthuijsen [2007].

A harmonic wave that propagates at the ocean's surface has a dispersion relationship between radian frequency, ω, and wave number, k:

$$\omega^2 = gk \tanh kd \tag{2.5.1}$$

where d is depth. If depth decreases, the wave length will decrease. The phase speed will correspondingly decrease:

$$c = \sqrt{\frac{g}{k} \tanh kd} \tag{2.5.2}$$

Initially the group velocity c_g increases slightly, but then it also decreases:

$$c_g = nc \tag{2.5.3}$$

$$n = \frac{1}{2}(1 + \frac{2kd}{\sinh 2kd}) \tag{2.5.4}$$

As stated earlier, because the wave propagates to shallow water, the phase speed will become equal. Both the phase speed and the group velocity approach zero at the water line. The variation in the group velocity causes variations in the energy of the wave and amplitude [Holthuijsen, 2007].

2.5.2 Refraction

In general, waves arrive parallel to the shore as they leave deep water. This effect is caused because waves try to conform to bottom contours. Refraction results from the inshore portion of the wave having a slower speed than the portion still in deep water. This causes a change in wave height and direction in shallow water [Holthuijsen, 2007]. If a harmonic wave approaches a hypothetically straight coast at an angle, the wave will slowly change direction until it is parallel as it approaches the coast. Refraction is created because of depth variation along the wave crest and because there is a variation in phase speed along the crest.

$$c = \sqrt{\frac{g}{k} \tanh kd} \tag{2.5.5}$$

The crest moves faster in deeper water so that, in a time interval, the crest will move farther in deeper water than it does in shallower water. The effect is that the wave turns toward the region with shallower water, or, toward the coast. This is a universal characteristic of waves: a wave always turns toward the region with a lower propagation speed [Holthuijsen, 2007].

2.5.3 Diffraction

In the absence of refraction, waves will travel into the shadow of an obstacle in almost a circular pattern of crests with diminishing amplitude [Holthuijsen, 2007]. For refraction, the linear theory was used to model the wave's behavior, but to account for diffraction, the spatial derivatives of amplitude in the linear wave theory must be included. Following the

steps explained by Holthuijsen [2007], the extension of the Laplace equation yields extra terms in the expression of the linear wave theory:

$$C = c(1 + \delta_a)^{-1/2} \tag{2.5.6}$$

where c is the phase speed of the harmonic wave without diffraction's effects and C is the phase speed of the harmonic wave including the effects of diffraction. The term δ_a is the diffraction component that includes the non-linear terms:

$$\delta_a = \frac{\nabla^2 a}{k^2 a} \quad \text{where} \quad \nabla^2 a = \frac{\delta^2 a}{\delta x^2} + \frac{\delta^2 a}{\delta y^2} \tag{2.5.7}$$

and k is the wave number. The group velocity becomes:

$$C_g = c_g(1 + \delta_a)^{1/2} \tag{2.5.8}$$

The turning rate is given by the same equation as refraction. The simplified equation for diffraction in a constant depth of water is:

$$\left(\frac{d\theta}{dn}_{dif}\right) = \frac{1}{2(1 + \delta_a)\frac{\partial \delta_a}{\partial m}} \tag{2.5.9}$$

and the turning rate in time for diffraction in a constant depth of water is:

$$c_{\theta,diff} = \frac{C_g}{2(1 + \delta_a)} \frac{\partial \delta_a}{\partial m} \tag{2.5.10}$$

The computation of the wave rays require amplitudes, which requires the wave rays to be known. As Holthuijsen [2007] explains, the above approach is unconventional because of the complex computations. Approximations can be made with an Eulerian approach. Because of the complexity of diffraction, the entire explanation will not be written here. See Holthuijsen [2007] for more in-depth descriptions.

2.5.4 Reflection

Coasts will reflect waves to some degree as the wave propagates close to it. At each point off the coast, the motion of the wave is the combination of the incoming wave and the

reflections. The modeling for this phenomena depends on coastline characteristics because different geographies will result in different levels of reflection.

2.5.5 Attenuation

In the event of an earthquake, shock waves are transmitted from the point of origin in all directions. The shock waves pass completely through the earth and return to the surface and can be recorded on seismographs thousands of miles away. There are three basic types, each of which is slower than its predecessor [Myles, 1985]. The first to arrive are known as P (or primary) waves. Primary waves are of comparatively low amplitude and have a short distance from crest to crest. They thrust in the line of their own propagation so they are called longitudinal waves. These waves travel in any medium and are almost twice as fast as their successor, known as S (or secondary) waves. The different types of waves are shown in Figure 2.5.1.

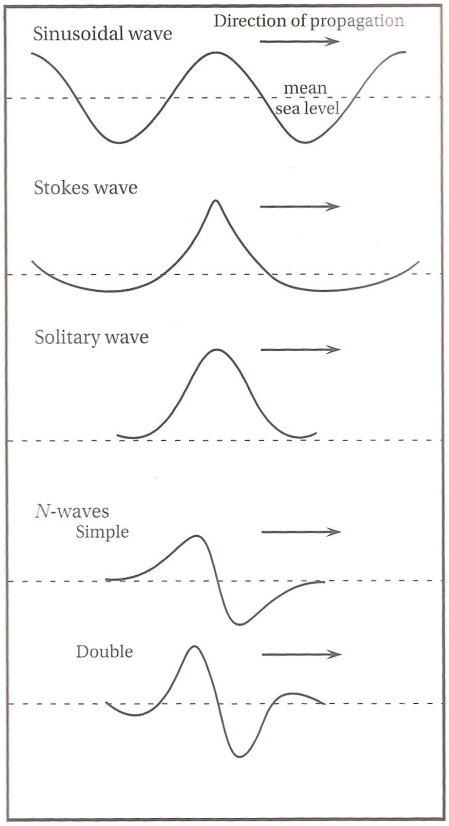

Figure 2.5.1: Depiction of different types of wave types [Bryant, 2001].

The secondary waves' arrival time is dependent on the distance from the quake's focus. Measuring the time interval between the arrival of P and S waves can pinpoint the epicenter of an earthquake. From the speed of the waves provided by the Jeffreys-Bullen table, the distance traveled can be computed [Myles, 1985]. S-waves' amplitude is greater than P-waves and their period is longer. Their passage produces lateral rather than vertical vibration; they are called shear or transverse waves. If they begin to move through gas or liquid substances, these waves are deflected or absorbed.

2.6 Comparison of Surface waves and Tsunami Waves

Normally, slippage of the earth's crust due to a submarine earthquake creates seismic sea waves. This slippage is normally vertical, causing a rising or subsidence of the sea floor, which creates a duplication of this change at the surface. Figure 2.6.1 shows that when the sea floor either rises or falls, the surface will follow. Either case will cause an oscillation and the tsunami moves away from the point of origin in ever-expanding concentric circles, one after another (see Figure 2.6.2). There can be as many as five or six successive waves, and sometimes as many as nine [GAO, 2006].

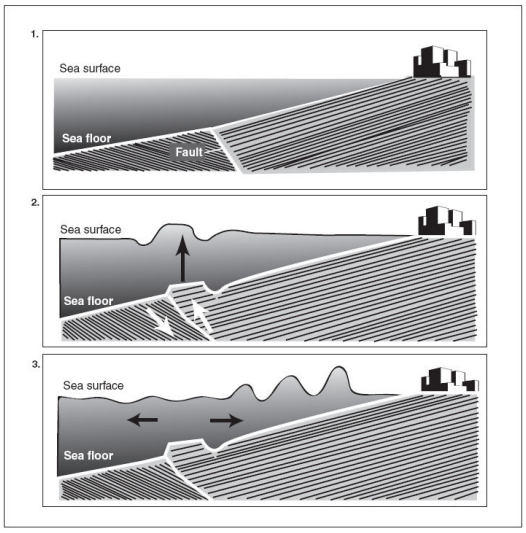

Figure 2.6.1: Subduction zone earthquake generates a tsunami [GAO, 2006]

The tsunami wave can be very high at the source, but it is quickly flattened by gravity and looks like a normal longitudinal wave. However, the tsunami may have an enormous

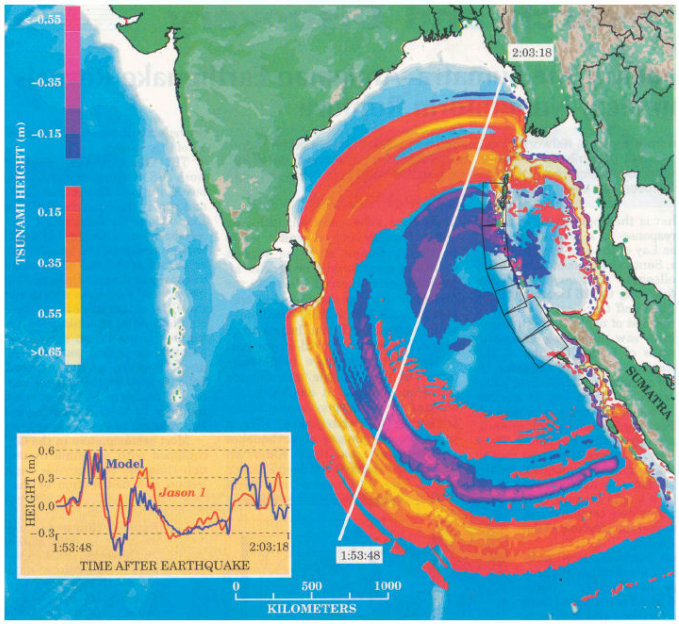

Figure 2.6.2: Simulated snapshot of tsunami consisting of reconstructed peaks and troughs that formed in Indian Ocean at a moment 1 hr, 55 min after the earthquake struck [Wilson, 2005]

wavelength (as much as 600 miles in the broad Pacific deep-ocean basin), but have a height from crest to trough of two feet or less in the deep ocean. As such, it will have a speed proportional to the square root of the depth of water over which it is passing. The velocity of tsunami is readily found by:

$$v = \sqrt{gd} \tag{2.6.1}$$

In this equation, v is the velocity of the wave, g is the gravitational acceleration, and d the depth of the water. Samples of average speeds for tsunami in each ocean are shown in Table 2.6.1.

Table 2.6.1: Average Speed of Tsunami Waves in Earth's Oceans

Ocean	Avg Depth (m)	Deepest Depth	Tsunami Wave Speed (m/s)
Pacific Oc.	4637	Mariana Tr. 11033	$766.8 < v < 1184.4$
Atlantic Oc.	3926	Puerto Rico Tr. 8605	$705.6 < v < 1044.0$
Indian Oc.	3963	Java Tr. 7725	$709.2 < v < 990.0$
Southern Oc.	4500	S Sandwich Tr. 7235	$712.8 < v < 957.6$
Arctic Oc.	1205	Eurasia Basin 5450	$388.8 < v < 831.6$

Source: [Halif and Sabki, 2005].

Wavelength of a tsunami can be found by:

$$\lambda = vt \tag{2.6.2}$$

For the example of the great Chilean earthquake of 1960, the wave traveled 6,600 miles in 14 hours and 56 minutes from the Chilean coast to Oahu, Hawaii, having an average speed of 442 miles per hour. It had a period of 60 minutes, which was computed from tide gauge data in the Pacific Basin. The wavelength of this tsunami was approximately 520 miles. From these computations, it is obvious why ships on the open ocean cannot detect tsunami. Despite its great speed, the tsunami passes under a large vessel without any effect. It is only when the tsunami arrives at the coast that it changes.

Where the continental shelf rises, tsunami encounters shallow water for the first time. The drag effect of the shallow bottom causes a tremendous slowing of the tsunami's velocity. Over a mile or two of shelf distance, a 500 mph tsunami may have its speed reduced to half. Meanwhile, as the P-wave slows, the water behind it *piles up*, causing it to rise rapidly to a great height. The differences in the tsunami's equations for velocity and wavelength should indicate why someone surfing a normal surface wave 45-feet high can survive, while a 6-foot tsunami can devastate whole regions and have deadly force. The next chapter will explore the phenomena associated with a tsunami and how these characteristics can be detected.

Chapter 3

Tsunami Phenomenology and Detection

Tsunami is defined as an ocean wave produced by a sub-marine earthquake, landslide, or volcanic eruption (see Table 3.0.1) that create sudden dislocations of the ocean floor. Tsunami waves have sufficient energy to travel across entire oceans. The waves have a large amplitude and are long, nonlinear surface gravity waves. As explained in Section 2.6, the waves propagate outward from the epicenter very rapidly with a small detectable height in the deep ocean.

Table 3.0.1: Causes of Tsunami across the Globe over the Last 2,000 Years [NGD, 2007]

Cause	Number of Events	Percentage of Events	Number of Deaths	Percentage of Deaths
Landslides	26	3.3	1,549	0.3
Earthquakes	700	89.3	501,412	91.7
Volcanic	51	6.5	37,845	6.9
Other	7	0.9	6,210	1.1
TOTAL	784	100	547,016	100

The Sumatra tsunami had a recorded wave height of 60-80 cm in the deep ocean. As explained in Chapter 2, when a tsunami wave nears the shore and encounters shallow coastal water, it will shoal. Shoaling causes a decrease in speed, an increase in wave height, and allows the tsunami to align parallel to the shore. The Sumatra tsunami had a maximum wave height of 15 m in shallow water near Banda Aceh. To protect those living in areas with a potential for tsunami landfall, the time from tsunami creation to impact is the most

important factor in saving lives. Any effort to detect the tsunami as soon as possible from the point of origin in the ocean will increase the number of protected individuals.

In this respect, a detection system located on a satellite platform will increase warning time by detecting the tsunami further away from a susceptible coastline and more immediately upon generation. Currently, parts of the detection of tsunami is conducted closer to shore, through the data collected on tide gauges. Tsunameters in the ocean are also only in limited locations, which increases the probability of time spent waiting for the tsunami to arrive. As technology progresses, deep ocean tsunami detection capability has increased. Moving forward with deep ocean detection from space will provide a significant benefit to at risk coastal communities.

A tsunami is a surface gravity wave with a wavelength much larger than the ocean depth. The wave develops in three stages: formation of the wave due to the initial cause and propagation near the source; free propagation of the wave in the open ocean at large depths; and propagation of the wave in the region of continental shelf and shallow coastal water. These stages, and other properties, will be explored to better understand a tsunami wave's behavior.

3.1 Tsunami Phase Velocity

A wave's phase velocity is the rate at which the phase of the wave propagates in space. Its group velocity is the rate that amplitude changes will propagate. The phase velocity, c, and group velocity, v, are nearly equal and can be found by (which has already been shown in Chapter 2):

$$c = v = \sqrt{gd} \tag{3.1.1}$$

where g is the gravitational constant and d is the depth of the water. For depths greater than 50 m, the tsunami behaves as a linear long-wave. This assumption allows a spectral representation for the tsunami to be used, as explained by Bryant [2001]. In a long gravity wave of amplitude, a, the amplitude of the horizontal and vertical surface velocities (u_h and u_v respectively) can be found by:

$$u_h = a\sqrt{\frac{g}{d}} \tag{3.1.2}$$

$$u_v = \frac{2\pi}{cT} d u_h \tag{3.1.3}$$

where c is the phase velocity and T is the period [Bryant, 2001]. Using an amplitude of 0.3 m (a typical height of a tsunami in the deep ocean) and the average ocean depth, $d = 3808$ m, these velocities are relatively small: $u_h = 0.015$ m/s and $u_v = 1.88/T$ m/s.

3.2 Resonance

Resonance can occur in any semi-enclosed body of water caused by a sudden change in barometric pressure, tides, volcanic eruptions, or tsunami. The wave period of the cause determines if the body of water will be affected by resonance. Tsunami can be amplified within natural or man-made areas such as harbors and bays if the period approximates some harmonic of the basin's natural frequency [Bryant, 2001]. The word *tsunami* literally means "ferry crossing wave" in Japanese, but most translate it to "harbor wave" for this reason. Tsunami can oscillate in the basin for longer periods of time which can last up to twenty-four hours or more. The oscillations are known as *seiches*, which is a German word used to describe long, atmospherically induced waves in Swiss alpine lakes [Bryant, 2001]. Seiches are independent of the forcing mechanism and are related to the three-dimensional form of the bay or harbor as follows:

$$Enclosed\ basin:\ T_s = 2L_b(gd)^{-.05} \tag{3.2.1}$$

$$Open\ basin:\ T_s = 4L_b(gd)^{-.05} \tag{3.2.2}$$

where L_b is the length of the basin or harbor and T_s is the wave period of seiching in a bay, basin, or harbor [Bryant, 2001]. Equation 3.2.1 is known as Merian's Formula and is for enclosed basins. These basins do not need to have a link with the ocean to be affected. For example, the 17 January 1994 Northridge earthquake emptied swimming pools in Los Angeles, CA.

3.3 Run-up and Inundation

Tsunami wave height increases near the shore and is called run-up. The run-up height can often be more than two times the wave's height in the deep ocean. In the Pacific Region, forty-two tsunami have generated wave run-up heights in excess of six meters since 1900. The Alaska tsunami of 1 April 1946 overtopped cliffs on Unimak Island and wiped out a

lighthouse as shown in Figure 3.3.1. The largest run-up height in recorded history was from the 9 July 1958 tsunami in Lituya Bay, Alaska. Water swept 524 m above sea level up the shoreline on the opposite side of the bay [Bryant, 2001]. The run-up height of a tsunami varies depending upon the configuration of the shore, diffraction, standing wave resonance, and trapping of incident wave energy by refraction of reflected waves from the coast.

Figure 3.3.1: The Scotch Cap lighthouse on Unimak Island, Alaska before and after the 1946 tsunami [University of Washington, 2005].

A tsunami's motion in water is different from other waves because the wave's motion occurs throughout the entire water column, from the surface to the ocean bottom. This phenomenon causes a tsunami to take on the shape of a solitary wave in shallow water. Little energy is dissipated because the wave's motion involves the entire water column, especially on steep coasts. The maximum run-up height is:

$$H_{rmax} = 2.83(\cot\beta)^{0.5} H_s^{1.25} \tag{3.3.1}$$

where H_{rmax} is the maximum run-up height of a tsunami above sea level and H_s is the wave height at shore [Bryant, 2001]. If the wave is preceded by a trough, then the maximum run-up height will be even greater. An N-wave (either single or double), as shown in Figure 2.5.1, is more likely to be generated near the shore because it occurs when the critical distance over which a tsunami wave develops is not long enough relative to the tsunami's wavelength to generate a wave with a leading crest. The critical distance can be as great as 100 km from shore. The following equations govern an N-wave's maximum run-up height of a tsunami

above sea level (H_{rmax}) [Bryant, 2001].

$$Simple\ N-wave:\ \ H_{rmax} = 3.86(\cot\beta)^{0.5} H_s^{1.25} \tag{3.3.2}$$

$$Double\ N-wave:\ \ H_{rmax} = 4.55(\cot\beta)^{0.5} H_s^{1.25} \tag{3.3.3}$$

The general characteristics of a tsunami including velocity, deep ocean height, direction, and earthquake magnitude all play a part in the detection of tsunami. In order to accurately detect a tsunami wave, these characteristics must be understood and included in the detection technology. The next section explains the current technology and its components.

3.4 Current Detection System - DART II Buoys

Currently, detection relies on the network of Deep-Ocean Assessment and Reporting of Tsunami (DART) II buoys placed by the National Oceanic and Atmospheric Administration (NOAA) in the oceans near critical land masses like Hawaii, Japan, and the western coast of the United States (Figure 1.3.1). DART II buoys are fabricated at NOAA's Pacific Marine Environmental Laboratory located in Seattle, Washington. The United States government assisted the government of Thailand in launching the first buoy in the Indian Ocean between Thailand and Sri Lanka on December 1, 2006 [Eisenman and Feltgen, 2006] as shown on the map in Figure 1.3.1. It is the first of 22 tsunameters planned for the Indian Ocean's regional tsunami warning system.

The DART II System employs a tsunameter comprised of a bottom pressure recorder (BPR) and a bi-directional acoustic link to communicate to a satellite network (Figure 3.4.1). The BPRs that are capable of detecting a tsunami with a wave height of one cm in 6,000 m of water [Lautenbacher, 2005].

Tsunameters used by NOAA have a maximum depth allowance of 6000 meters, can be deployed for longer than one year, and cost less than $250,000 [Gonzalez et al., 2005]. The tsunameter creates tidal reports every 15 minutes for transmission to the buoy with a maximum status report interval of less than six hours. It can automatically generate a tsunami detection report when the tsunami detection algorithm is employed [Meinig et al., 2005b]. The tsunami detection algorithm is a process that verifies the plausibility of a tsunami's creation from an energy-generating event, like an earthquake.

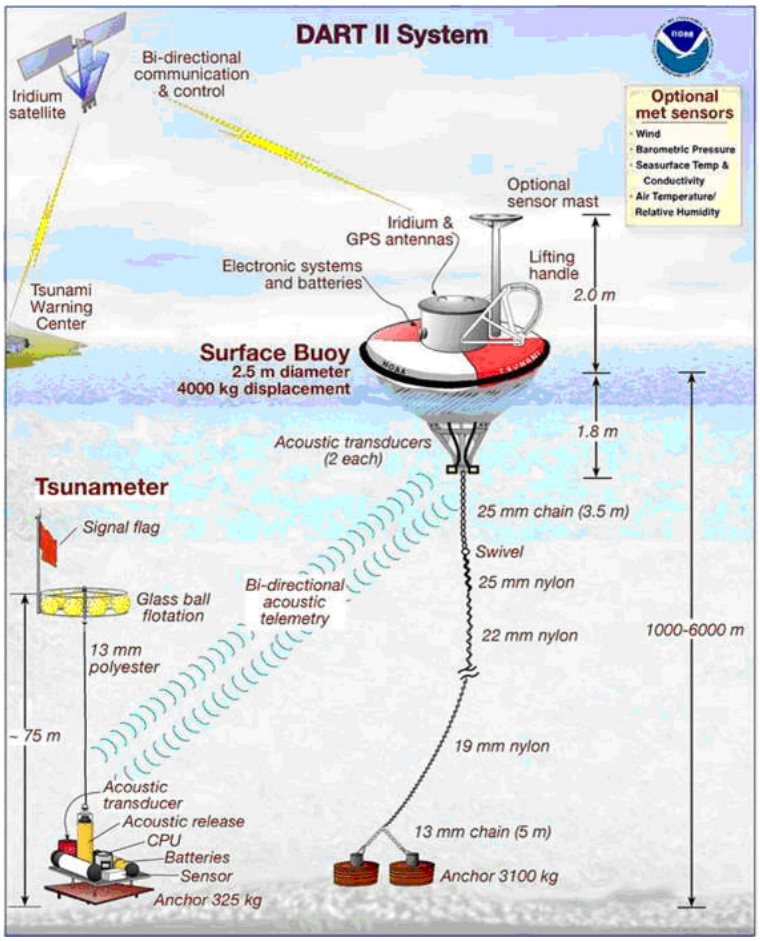

Figure 3.4.1: DART II System [Meinig et al., 2005a]

While tsunamis are typically recorded by tidal gauge stations, recordings on the high seas have been rare because a tsunami's wave amplitudes are small and its wavelength is large. This prevents direct observation of surface deformation and is a major disadvantage of the system. Two types of observational sensors are known to directly detect a tsunami in the open ocean: altimeters and microwave radiometers. Another observation method is visible detection. Although this type of detection allows very minimal warning time, it highlights some unique characteristics of tsunami as it approaches shore. The next section explains the experiences of those who have reported a visible sighting of a tsunami before its arrival on land.

3.4.1 Visible detection

Detection of tsunami by the visible eye has been documented. On 4 October 1994, along the shore of Oahu, Hawaii, observers saw a dark strip on the ocean surface. The strip's arrival coincided with a small tsunami from the Shikotan earthquake. A pilot also saw a dark strip 2300 miles from the epicenter of the 1 April 1946 Aleutian Islands earthquake [Dudley and Lee, 1998]. The visible element of the tsunami is called a "tsunami shadow", which is caused by a change in the sea surface slope that affects sunlight's surface reflection. The slopes of the mean ocean surface due to a tsunami are small, typically 1-6$\times 10^{-10}$ away from the shore [Godin, 2004]. The subtle change in sea surface slope in the deep ocean affects surface microwave emission and therefore is likely to be detected by a radiometer (see Figure 3.4.2).

There are also other non-visible tsunami surface manifestations including wind velocity changes and airflow turbulence in the atmospheric boundary layer above the surface. Godin discovered that in the lowest few centimeters of the atmosphere above the ocean's surface, wind velocity perturbations can exceed the velocity of tsunami-induced currents by a factor of 10 to 60 for representative values of tsunami and wind parameters, which appears to be the cause of the mysterious tsunami shadow observations. Because of the change in the sky brightness and color, an observer directly overhead will view the change in the surface as a dark area, which is the tsunami shadow.

Although a tsunami shadow can be seen with the naked eye, it is feasible to conduct data collection with another type of sensor like a microwave radiometer or radar. These sensors have an advantage over optical sensors: they can overcome many meteorological conditions, especially cloud cover. Spaceborne sensors with an ability to detect tsunami are discussed in the next section.

3.4.2 Satellite Observational Data and Sensor Types

Satellites have various remote sensing capabilities. For oceanographic parameters, altimeters and radiometers are the primary mode of observation. These sensors detect changes in variables that describe the ocean surface's physical phenomena and the sea-atmosphere interaction. Specific property changes can be indicative of a tsunami.

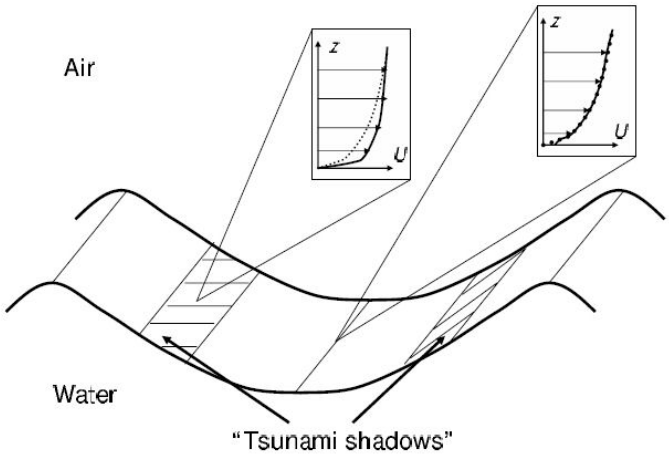

Figure 3.4.2: Tsunami shadows are parallel to the wave front and occur in between tsunami troughs and crests where the wind perturbation is maximal. Perturbed (solid lines) and unperturbed (dotted lines) wind velocity is shown as a function of height above the ocean surface [Godin, 2004].

Satellite Altimetry

Altimetry data is available from many current space platforms and its availability is advantageous for post-hoc tsunami detection. The data analysis of altimetry requires time to parse the signal from noise levels and height variations in the ocean surface not due to tsunami. Due to the time restraints of early-warning, the delay in understanding data due to processing time is too restrictive. Thus, altimetry data cannot be part of an effective early-warning system. Progress in satellite altimetry allowed post-hoc detection of the 1992 Nicaraguan tsunami's deformation of the ocean surface [Okal et al., 1999].

Altimetry data from the Jason-1 satellite detected the 2004 Sumatra tsunami (Figure 3.4.3), which measured the amplitude of the tsunami in the open ocean. Days after the tsunami struck land, altimetry data was analyzed. The radar altimeter onboard the Jason-1 satellite registered the sea level displacement of the head tsunami wave and its shape [Gower, 2005]. Numerical simulations corroborated the detection [Lay et al., 2005]. The tsunami front was detected as it passed through 3°S latitude. Note the disturbed sea height behind the front shown in Figure 3.4.3. At approximately 4°N latitude, there was a storm which also was detected by the altimeter, although its choppy characteristics are visibly different from the tsunami wave.

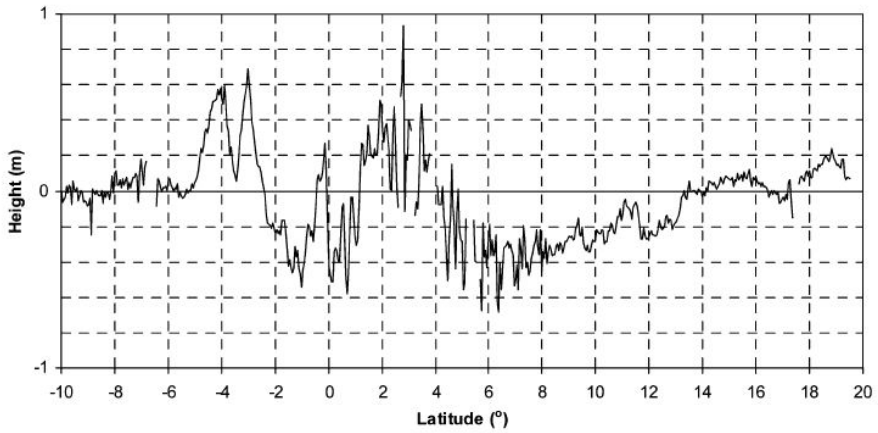

Figure 3.4.3: Plots of sea surface height anomalies on Jason-1's pass 129 in cycle 109 [Gower, 2005]

The altimeter in Cycle 109 recorded a rise in sea level of about 70 cm above the average height measured in Cycles 108 and 110. The total trough-to-crest wave height was about 1 m [Godin, 2004]. Analysis of the data from the Jason-1 satellite showed that other data, including the changes in wind speed, exhibited a significant variation simultaneously as the sea level varied. Aside from altimeters, radiometers are also a feasible sensor for tsunami detection.

Microwave Radiometry

For some sensors, including altimeters, atmospheric conditions like haze, rain, or clouds can scatter ocean emissions before the sensor receives the data. Microwave radiometers are advantageous because they avoid scattering by using long wavelengths and are considered all-weather devices. Although they possess all-weather capability, they do have some disadvantages. First, thermal emission is weak at longer wavelengths. Second, in order to maintain signal strength, a wide field of view (FOV) must be kept, which makes the associated spatial resolution of microwave radiometers poor. Despite disadvantages, microwave radiometers do have the capability to measure a multitude of oceanographic parameters: sea surface salinity, sea surface temperature, and sea surface roughness. Spaceborne microwave radiometers detected the 26 December 2004 tsunami. Jason-1's 3-channel radiometer operating at frequencies 18.7 GHz, 23.8 GHz, and 34 GHz that are used for retrieving water

vapor content in the atmosphere, detected the tsunami. The brightness temperature reflected the sea surface roughness variations [Troitskaya and Ermakov, 2006].

A change in sea-surface slope due to the Sumatra tsunami was also detected by a satellite. The initial tsunami waves heading west took 2 hours to make landfall on Sri Lanka's southwestern coast. As the National Aeronautics and Space Administrations's (NASA) Terra satellite passed overhead, the Multi-angle Imaging SpectroRadiometer (MISR) payload captured an image of deep-ocean tsunami waves about 30-40 km from Sri Lanka's SW coast (Figure 3.4.4). The waves in the image arrived three hours after the initial tsunami wave. The image covers 208 km x 207 km. The waves were made visible because sea surface slope changes affected the sun glint pattern seen from MISR's 46-degree-forward looking camera. The large waves were invisible to MISR's nadir camera.

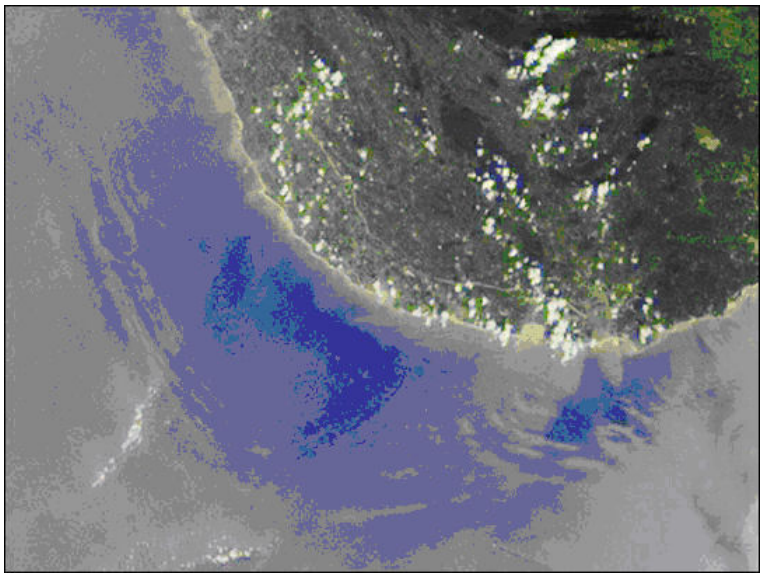

Figure 3.4.4: Deep ocean tsunami waves off the Sri Lankan coast detected from the Terra satellite [Staff, 2005a]

Radiometers can detect a profile of the ocean's surface parameters at a given time or capture multiband radiometric images. These images have advantages over profile data because they show the spatial variability and features of ocean hydrodynamic processes and fields through unified passive microwave pictures [Raizer, 2005a]. The capability for a satellite to detect a tsunami in the deep ocean is based on the physical principles of microwave radiometry and the ocean's physical characteristics and traits. The next chapter will delve into the parameters of microwave technology, its history, background, improvements, and

uses. This will highlight the advantages of using a microwave radiometer to measure the ocean for a variety of uses which supplement the use of tsunami early-warning and detection.

Chapter 4

Microwave Radiometer Technology

The ocean has been monitored through the use of sensors for many years. The most common type of monitoring method is aerial photography. However, microwave radiometry has several advantages, namely the ability to penetrate clouds and an independence of the sun as a source of illumination. Microwave radiometers are also able to penetrate significantly into the surface itself. This penetration is not available with the use of visible sensors or infrared radiation.

Microwave remote sensing combines the physical properties of the studied surface and the radiowave propagation. Sensors can either be passive or active. Active sensors are those that have their own source of illumination, like scatterometers, radar imagers, or altimeters. Passive sensors are receivers that measure the radiation coming from the observed scene. The passive type is what is referred to as a microwave radiometer.

Radars have been used to map geological structures, particularly when cloud cover prevents mapping by optical sensors. Microwave radiometers have mainly been used to measure the sea-air interaction over the ocean surface, retrieve atmospheric temperature and water vapor density over the oceans, and to discriminate between different types of sea ice as a navigational aid. Other potential applications are being researched and include soil moisture content, snow water content, and tsunami detection.

A microwave radiometer is mainly used because it is independent of the sun and can penetrate clouds, rain, and other objects to an extent [Ulaby, 1981]. For example, a radiometer can penetrate dense vegetation. Optical waves have a more difficult time penetrating deeply into dense vegetation. A radiometer's actual depth of penetration is dependent on the veg-

etation's moisture content and its density, as well as the wavelength of the radiometer. Longer wavelengths penetrate more deeply so shorter wavelengths reveal properties of the upper layers of vegetation and longer wavelengths yield information of the lower layers of vegetation.

Microwaves can also penetrate into the ground, or ocean surface, itself; this penetration is larger than that obtainable with visible and infrared radiation [Peichl et al., 2003]. Microwaves also have different information from that of visible and infrared regions of the spectrum. Observing a part of the ground that was covered with vegetation would show that the color in the microwave region is a result of geometric and bulk-dielectric properties. The color in the infrared and visible region is determined by molecular resonances in the surface layer of the vegetation. The three different types of measurements can complement one another to achieve a maximum amount of information. The increase in types of measurements is a sign of progress through the history of microwave radiometry. Overall, radiometers have advanced significantly in the past seventy years.

4.1 History of Microwave Sensing

Any matter radiates electromagnetic energy. The radiation is due to collisions of molecules inside the material. Radiometry is the measurement of incoherent radiant electromagnetic energy. Microwave radiometer techniques were developed in the 1930s and 1940s to measure electromagnetic energy of extraterrestrial origin. Until 1958, radiometers were never used to measure radiation of the earth's surface. During that year, a group at the University of Texas made radiometric observations of several materials like water, wood, and grass. Since the research group's initial curiosity in the radiometry of the earth, microwave radiometry has become an integral part of environmental remote sensing [Ulaby, 1981].

Passive microwave radiometry measures naturally emitted microwave energy, called brightness temperature, which is based on a surface's physical, electrical, and thermodynamic variables. The ocean surface's properties affect physical-electrical interactions, which then determine the surface's microwave emission [Robinson, 2004].

The first brightness temperature data was acquired from a satellite platform on 14 December 1962, aboard the Mariner 2, when sensors observed the planet Venus [Ulaby, 1981]. The satellite had a 2-channel microwave radiometer operating at wavelengths of

1.35 and 1.9 cm. Later, the Russians made passive observations of Earth in 1968 with the satellite Cosmos 243 which had four microwave radiometers. Other satellites that used microwave radiometer sensors include Skylab; Nimbus 5, 6, and 7; and Seasat. In 1972, NASA's Nimbus-5 satellite carried the Nimbus-E microwave spectrometer (NEMS) and the electrically scanning microwave radiometer (EMSR). In 1975 another EMSR flew with a scanning microwave spectrometer on the Nimbus-6. EMSR scanned through different angles but the NEMS measured only a single nadir view in five channels. The EMSR on Nimbus-5 identified different types of sea ice in the Beaufort Sea and the NEMS measured rainfall distribution over the oceans [Robinson, 2004].

In 1978, a scanning multifrequency microwave radiometer (SMMR) was flown on Seasat and Nimbus-7. The Nimbus-7 radiometer was the first radiometer designed to observe the earth's oceans. SMMR's performance in measuring the sea surface temperature (SST) was not impressive because it was not possible to obtain accurate calibrations of the radiometer [Robinson, 2004]. During the 1980s, a radiometer's measurements were inferior to an infrared sensor's, causing oceanographers and scientists to focus more completely on the infrared spectrum. The next radiometer that had the capacity to measure SST was flown nearly 20 years after SSMR's launch. The SMMR continued to record measurements until 1986 [Robinson, 2004]. The longevity of the sensor combined with improved atmospheric water measurements led swiftly to a successful series of microwave radiometers for atmospheric application, the SSM/I series [Robinson, 2004].

The special sensor microwave imager (SSM/I) was first deployed in 1987. This sensor was able to calibrate more accurately through the use of a hot load/cold sky system (described in Section 4.4.5), making it a reliable sensor. This sensor has been fabricated multiple times by the US Defense Meteorological Satellite Program (DMSP). Many different defense satellites from 1987-2000 flew the sensor, allowing it to have a long history of measurements. However, it still had an inability to detect SST because its frequencies were not low enough. It measured water vapor and wind successfully, adding these areas to the effective uses of radiometer measurements. These measurements helped to improve the database used by global atmospheric models.

The evolution of microwave radiometers since the late 1960s enabled an increase in the range of frequencies that can be scanned. In 1998 the MTVZA multichannel microwave imaging radiometer aboard the Meteor-3M spacecraft used by the Russian Space Agency

utilized frequencies as low as 19 GHz [Cherny and Raizer, 1998], but by 2005, the lowest frequency was 6.9 GHz [Vitaliy, 2005]. The progress of microwave radiometer technology has allowed improved sensitivity for determining oceanographic parameters like ocean temperature and wind. While radiometer design technology improved, the purpose of radiometers expanded. The radiometer's improvement is founded on their physical principles. Next, thermal emission, emissivity of the ocean, and depth of microwave penetration will be explored to further understand the physical principles of microwave radiometers.

4.2 Physical Principles of Microwave Radiometers

Microwave radiometers normally operate at electromagnetic wavelengths between 0.1 cm and 100 cm. Radiometers observe thermal radiation emitted by the ocean's surface, which can help relate oceanographic parameters to the presence of tsunami. One advantage of radiometry is that at long wavelengths, it is not limited by absorption or scattering created because of the atmospheric effects. Physical attributes such as the microwave's thermal emission and penetration depth serve as indicators of a tsunami's presence. Robinson [2004] gives the detailed analysis of the basic laws explaining the following parameters.

4.2.1 Thermal emission

Planck's radiation law controls the thermal emission of the microwave:

$$L_\lambda(\theta,\phi) = \frac{2hc^2\epsilon(\theta,\phi)}{\lambda^5 e^{\frac{hc}{\lambda kT}} - 1} \tag{4.2.1}$$

where L_λ is the spectral radiance at wavelength λ, in units of power per steradian per unit projected area per unit wavelength interval; h is Planck's constant; c is the speed of light; k is Boltzmann's constant; T is the temperature of the emitter in K; θ and ϕ are the zenith and azimuth angles defining the direction of the microwave energy flux propagation; and $\epsilon(\theta,\phi)$ is the emissivity of the surface in the direction (θ,ϕ).

The emitted radiance for microwave radiation is expressed as T_B per unit frequency in the Rayleigh-Jeans approximation [Robinson, 2004]. The ocean can be represented as a black body at 300 K, therefore the approximation differs in preciseness from Planck's law by less than 1% as long as $\lambda > 2.57$ mm. Because the frequency is the phase velocity divided

by wavelength, it follows that:

$$T_B(\theta,\phi) = \frac{2hf^3}{c^2}\frac{\epsilon(\theta,\phi)}{e^{\frac{hc}{\lambda kT}}-1} \tag{4.2.2}$$

At microwave frequencies: $\epsilon(\theta,\phi) \approx 1 + \frac{hc}{\lambda kT}$ Therefore:

$$T_B = \frac{2kf^2\epsilon(\theta,\phi)}{c^2} = \frac{2kT\epsilon(\theta,\phi)}{\lambda^2} \tag{4.2.3}$$

Thus, the emitted radiance is directly proportional to the emitting body's temperature. Emitted radiance is sometimes referred to as brightness temperature, T_B [Robinson, 2004]. T_B is dependent on the emissivity of the surface, the frequency, and the viewing direction with respect to the normal of the ocean surface. Because of its dependence on viewing direction, brightness temperature is sensitive to surface geometry. This dependence allows a tsunami's presence to be detected.

4.2.2 Emissivity of the Ocean

The ocean's emissivity depends on the dielectric properties of the water skin-layer, surface waves, surface roughness, foam, temperature, and salinity. The Cole-Cole relaxation model is usually used for microwave remote sensing and gives a good approximation for the emissivity of salt water:

$$\epsilon_w = \epsilon_\infty + \frac{\epsilon_s - \epsilon_\infty}{1 + (i(\frac{\lambda_s}{\lambda})^{1-\alpha} - i60\sigma\lambda)} \tag{4.2.4}$$

where λ is the wavelength; σ is the conductivity of the water, ϵ_s is the low-frequency permittivity; ϵ_∞ is the high-frequency permittivity; λ_s is the critical wavelength, which is related to relaxation time τ by $\lambda_s = 2\pi c\tau$, and α is the Cole-Cole parameter which depends on the relaxation time distribution [Cherny and Raizer, 1998]. Normally, α is between 0.01 and 0.30. Dielectric relaxation is the momentary delay in the dielectric medium to an external electric field of microwave frequencies. The relaxation is described in terms of permittivity as a function of frequency. When $\alpha = 0$, the formula is simplified and is known as the Debye model.

The emission is dependent on polarization, which can be either horizontal or vertical. Horizontal and vertical polarization is defined relative to the surface of the ground. A

plane wave is horizontally polarized if its electric field vector is parallel to the surface and it is vertically polarized if its magnetic field is parallel to the surface [Ulaby, 1981]. The emissivity also depends on the Fresnel amplitude reflection coefficient, ρ, and is different for the horizontal and vertical polarizations states:

$$\epsilon_{H,V} = 1 - \rho_{H,V}^2 \tag{4.2.5}$$

The Fresnel amplitude coefficient can be found based on the dielectric constant, emissivity, and the incidence angle, θ:

$$\rho_H = \frac{\cos(\theta) - \sqrt{\epsilon_w - \sin^2\theta}}{\cos(\theta) + \sqrt{\epsilon_w - \sin^2\theta}} \tag{4.2.6}$$

$$\rho_V = \frac{\epsilon_w \cos(\theta) - \sqrt{\epsilon_w - \sin^2\theta}}{\epsilon_w \cos(\theta) + \sqrt{\epsilon_w - \sin^2\theta}} \tag{4.2.7}$$

The brightness temperature's dependence on geometry allows for the detection of oceanic parameters that indicate a tsunami's presence. However, its geometric dependence makes it difficult to calculate the emitted radiation exactly. Microwave radiometers use a wide field of view so the measured radiation must be integrated over an area having dimensions on the order of tens of kilometers. It is the statistical distribution of the angle of incidence (θ) for the field of view that affects the brightness temperature.

The brightness temperature, T_B, relies on sea surface slope statistics, which is something a tsunami's presence will alter. Therefore, the detected brightness from a microwave radiometer can determine the presence of a tsunami. In addition to depending on geometry and emissivity, the brightness temperature also depends heavily on frequency. This dependency causes measured characteristics like sea roughness and temperature to be measured at different frequencies.

4.2.3 Depth of Microwave Penetration

The microwave radiation penetration depth is related to its wavelength and the medium's conductivity. Penetration depends on salinity, temperature, and frequency. Skin depth, δ_s, is defined as the distance into the medium where the power of the electromagnetic radiation is reduced by a factor e^{-2} [Robinson, 2004]. The temperature of the water contributing to the emitted radiation determines the strength of the signal.

The penetration depth of millimeter and centimeter microwaves weakly depends on the water temperature and salinity. The optimal range of wavelengths for measuring sea surface temperature variations is between 3 and 8 cm. For measuring salinity the range is between 18 and 75 cm [Cherny and Raizer, 1998]. As wavelength increases, the influence of salinity on the brightness temperature increases and the influence of SST decreases.

Satellite microwave radiometers use a frequency range of 6 - 10 GHz to measure SST with a penetration depth of 2 to 3 mm, which is much greater than the sea skin. Therefore, microwave radiometry can see beneath the ocean sea skin's thermomicrolayer. Skin depth has an impact on the emitted brightness and can be approximately calculated [Robinson, 2004]. Assuming a temperature decreasing exponentially with depth, d_T, with a microwave radiation distance of d_μ, the apparent temperature contributing to the radiation brightness is:

$$T_{app} = \gamma T_{z=0} + (1-\gamma) T_{subskin} \tag{4.2.8}$$

where

$$\gamma = \frac{\int_0^\infty e^{-\frac{z}{d_\mu}}}{\int_0^\infty e^{-\frac{z}{d_\mu}}} dz = \frac{d_T}{d_\mu + d_T} \tag{4.2.9}$$

and $T_{z=0}$ is the temperature at the true surface of the sea. Because of the differences in the microwave radiation and the distributed temperature distances, a radiometer is influenced greatly by the sub-skin temperature but weakly influenced by skin temperature.

4.3 Applications of Microwave Radiometry

A single multifrequency sensor can measure a multitude of different environmental parameters. The expansion of uses for radiometers includes area covered by ice, age of ice, ice edge, precipitation over land, land surface temperature, snow cover, tropical rainfall measurements, sea surface temperature, vegetation density, ocean salinity, and ocean wind speed. Atmospheric measurements like water vapor are important factors in sea-air interaction. Precipitation is a concern for those estimating the net flux of water across the air-sea interaction in relation to salinity and freshwater balances in the upper ocean. Wind parameters can also be measured, which drives many ocean processes.

The advancement in measuring sea surface temperature is also promising. Sea ice and its parameters are scientifically important in order to understand the role of polar sea

bottoms, in climate change, and in processes which affect marine biology in the marginal ice zone [Robinson, 2004]. The versatility of the sensor is remarkable and has a lot to offer because it can take several independent measurements of different parameters from the same sensor. These parameters many times are complementary to one another, so combined measurements can be exploited to advance studies of meteorological phenomenons.

Microwave radiometers can be used for astronomical studies, military applications, and environmental monitoring. Radiometers can also be used to measure emissions from other objects besides the earth. The military use of radiometers is mainly for detecting metal objects. The brightness temperature varies based on the material of an object, however there can be errors when using radiometry strictly for this purpose. Geoscientific fields like agriculture, hydrology, and meteorology also use radiometers to measure soil moisture, measure sea-ice mapping, or monitor severe storms like hurricanes and cyclones. Next, the radiometer's components and architecture are explained to understand the technology of microwave radiometry.

4.4 Basic Architecture

A microwave radiometer contains optics, detectors, an antenna, and feed horns (Figure 4.4.1). The optics collect, disperse, and separate the radiation's spectral components and then focus the radiation to a field stop. The detectors are located behind the field stop and respond to the photons with a voltage signal. The signal is amplified electronically and converted into digital counts. Radiometer performance is based on responsiveness, detection, and calibration. Responsiveness is a measure of the output per input. Detection is expressed as the ratio of the responsiveness per noise voltage. Calibration references the output to known inputs [Menzel, 2001].

4.4.1 Types of Radiometers

A radiometer measures power in terms of the equivalent temperature, which is the temperature of a black body that would radiate the same power. This equivalent temperature is known as the brightness temperature or T_B. It can also be the temperature of a resistor that has the same output power as that of the receiving antenna, known as antenna temperature or T_A. A radiometer has an antenna pointed towards an object of interest with equivalent

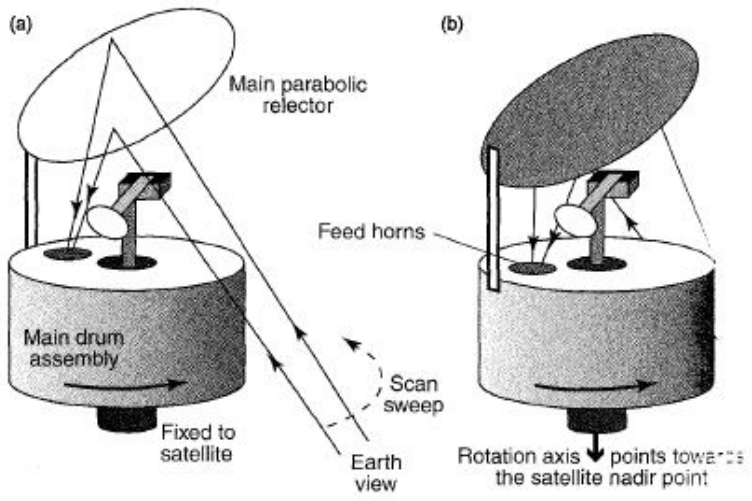

Figure 4.4.1: Mechanically Scanning Microwave Radiometer Schematic [Robinson, 2004]

brightness temperature. The output of the antenna is expressed in terms of the antenna temperature. The goal of using a radiometer is to relate T_A to T_B with sufficient resolution and accuracy to make a connection. The radiometer selects a portion of the power (in its bandwidth), around a certain frequency, and the power is amplified and output. The following derivations can be found in the text by Skou and Le Vine [2006]. The radiometer generates noise, T_N, which will also add to the input signal. The output power in Watts is:

$$P = kBG(T_A + T_N) \tag{4.4.1}$$

where k is Boltzmann's constant, B is the bandwidth, and G is gain. There is a sensitivity problem associated with all radiometer measurements. The radiometer's sensitivity is defined as the standard deviation of the output due to a constant input. The sensitivity equation is shown here:

$$\Delta T = \frac{T_A + T_N}{\sqrt{B\tau}} \tag{4.4.2}$$

For the power output to be stable, the portions of Equation 4.4.1 including, B, T_N, and G must be assumed constant. The bandwidth of the radiometer is dependent on a passive source, which is a filter. As long as the filter is designed and produced with care, B can be assumed to be constant. Gain and noise temperature, however, represent active components like amplifiers and mixers. The stability of G and T_N are extremely important and there

are ways with ensuring they are not counterproductive to measuring the T_B of the earth's surface.

Aside from stability, accuracy is also a concern. The main way to ensure accuracy is to calibrate frequently enough to know the constants. A stable instrument need not be accurate, requiring calibration. Section 4.4.5 discusses calibration in more detail. The following knowledge about radiometers and their properties is adapted from the thorough information given by Skou and Le Vine [2006].

Total Power Radiometer

Figure 4.4.2 shows the block diagram for a total power radiometer. The gain is represented by an amplifier with a gain of G and frequency selectivity has been symbolized by a filter with a bandwidth B. After the filter comes the detector, in this case a square-law detector. This type of detector is useful because the output voltage will be proportional to the input voltage and therefore the input temperature. Next, the signal from the detector is smoothed by an integrator to reduce fluctuations in the output. The longer the integration time, τ, the more smooth the output becomes.

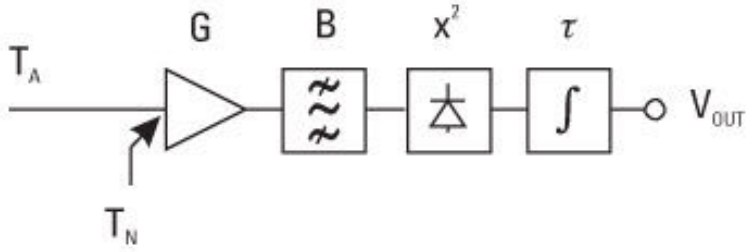

Figure 4.4.2: Block diagram of a total power radiometer [Skou and Le Vine, 2006]

This output can be expressed by:

$$V_{OUT} = c(T_A + T_N)G \tag{4.4.3}$$

where c is a constant. V_{OUT} is totally dependent on T_N and G. Sometimes, T_N and G are stable enough to satisfy requirements for accuracy. This is especially worthwhile when frequent calibration is possible. Other times, they are too unstable, requiring a different type of radiometer.

The sensitivity is expressed by:

$$\Delta T = \frac{T_A + T_N}{\sqrt{B\tau}} \tag{4.4.4}$$

The Advanced Microwave Scanning Radiometer (ASMR-E) used a total power radiometer. To achieve its superior sensitivity, calibration was conducted once per scan period of 1.5 s.

Dicke Radiometer

In 1946 R.H. Dicke found a way to improve the stability of radiometers. He did this by adding a component to the beginning of a total power radiometer: a switch (see Figure 4.4.3). This switch moves frequently between the antenna and a reference source of a known temperature, allowing the radiometer to measure the difference between the antenna and the known temperature. Therefore, the sensitivity of the measurement to gain and noise temperature instability is dramatically reduced.

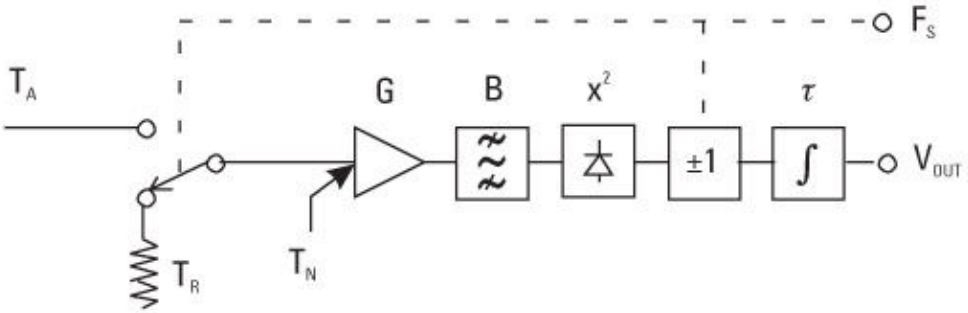

Figure 4.4.3: Block diagram of a Dicke radiometer [Skou and Le Vine, 2006]

The output of the square-law detector is multiplied by either $+1$ or -1 depending on the location of the switch, before integration. Provided that the switching frequency is high enough that T_N and G can be viewed as constants over the period and that the period is much shorter than τ, the radiometer output is:

$$V_{OUT} = c(T_A - T_R)G \tag{4.4.5}$$

From Equation 4.4.5, it can be seen that the noise temperature has now been eliminated from the power output by the radiometer. To achieve better immunity to instability, only

half of the measurement time is spent on the actual field of view to be measured. Therefore, the sensitivity is poorer than for a total power radiometer.

The conservative estimation of a Dicke radiometer's sensitivity is expressed by:

$$\Delta T = 2\frac{T_R + T_N}{\sqrt{B\tau}} \tag{4.4.6}$$

The T_R term can be replaced by T_A, but because $T_R < T_A$, this is the conservative estimate.

Noise-Injection Radiometer

This type of radiometer's output is independent of noise temperature and gain. In a Dicke radiometer, the output is zero if the reference temperature and antenna temperature are equal. The noise injection radiometer is a Dicke radiometer with an additional component: a servo loop (see Figure 4.4.4), which keeps the zero output voltage requirement. For Earth remote sensing, the antenna temperature is below approximately 300 K. The Dicke reference temperature is set at 300-320 K. For a noise-injection radiometer, the output T_I is added to the antenna signal T_A to ensure that the resultant temperature, $T_{A'}$, is equal to the reference temperature. This method requires accurate and stable noise noise sources.

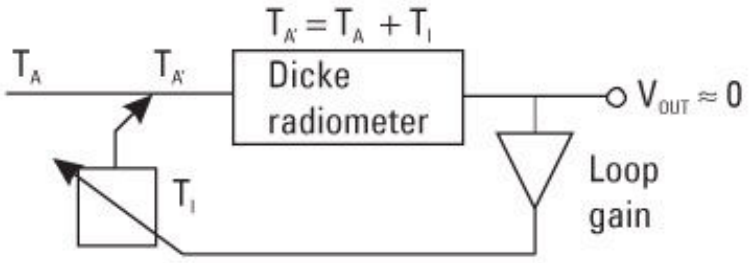

Figure 4.4.4: Block diagram of a noise-injection radiometer [Skou and Le Vine, 2006]

The sensitivity is equal to that of a Dicke radiometer and is given in Equation 4.4.6.

4.4.2 Scanning Radiometers

If a radiometer with a mounted antenna points toward the earth and does not scan, the forward movement of the earth at approximately 7.5 km/s will facilitate measurements on the ground in a straight line directly below the satellite's nadir. Obtaining coverage of the entire earth or even just the oceans would take an enormous number of spacecraft.

Therefore, scanning the reflector to achieve more observations per pass of the satellite will be more efficient and dramatically increase the mapping efficiency for the sensor. Figure 4.4.5 shows the geometry for such a scanning reflector.

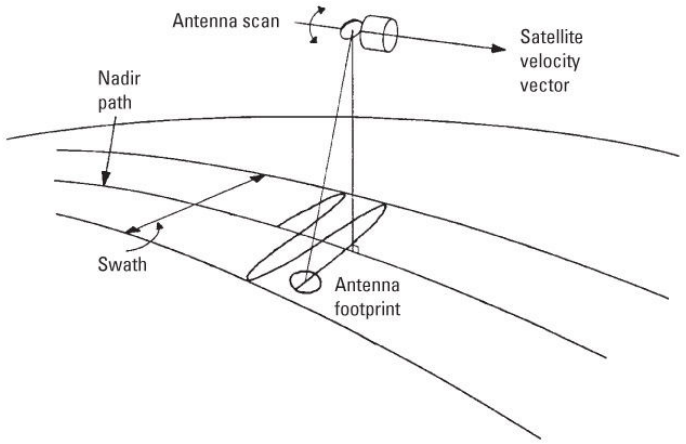

Figure 4.4.5: Spaceborne line scanner [Skou and Le Vine, 2006]

As explained in Skou and Le Vine [2006], the antenna moves back and forth around a rotation axis that is parallel to the satellite velocity vector. The maximum angle the antenna moves away from the nadir axis is defined as the scan angle. This movement makes the footprint move back and forth across the nadir path, covering a certain swath width on the ground. The swath width is dependent on the scan angle of the antenna and the satellite's altitude. Relationships exist between swath width, footprint, and scan speed. The speed must be large enough to not create gaps in the ground coverage. Because the footprint will move with the scan speed, there is a finite amount of time available to make brightness temperature measurements, which constrains the integration time of the radiometer.

Conical Scanner

The line scanner is used for spaceborne operations, but the system has one major drawback: varying incidence angle. Because the measurements are extremely delicate for our purposes, varying the incidence angle is not acceptable. A scanner that moves cylindrically is appropriate to overcome the drawback characterized in a line scanner. The conical scanner moves around a vertical axis, making the footprint scan the swath, but at a constant incidence angle, as shown in Figure 4.4.6. This type of scan has been used by the Technical University

of Denmark (DTU) airborne radiometry system and the Special Sensor Microwave Imager (SSM/I) created by NASA.

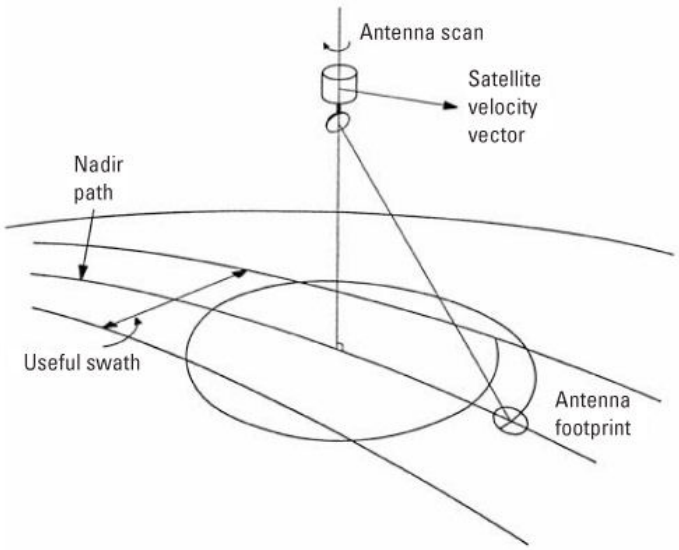

Figure 4.4.6: Spaceborne conical scanner [Skou and Le Vine, 2006]

The long wavelength of microwave radiation makes it difficult to focus and isolate a very narrow spread of rays onto the detector. To focus the rays, a scanning radiometer moves over the ground swath and focuses its beam from the narrowest field of view possible, without losing appropriate signal strength [Skou and Le Vine, 2006]. A parabolic reflector scans and focuses by rotating about its axis, which is set at an angle to the nadir axis. The parabolic reflector then directs the radiation to a set of feed horns located near the focal point of the reflector. The feed horns guide the radiation to the microwave detector devices which operate on individual frequencies to discriminate between horizontally and vertically polarized radiation. Due to each feed horn's offset, they all observe a slightly different field of view.

Scanning is accomplished by rotating the entire assembly. The observation is simpler if the sensor's axis is also the vertical between the satellite and the nadir point on the ground because the viewing angle of the observed beam relative to the ground is constant as the assembly rotates. For this design, the horizontal and vertical polarization states remain fixed relative to the detector. The main difficulty of rotating the entire assembly is that it requires rotation while observing the ocean, producing a large torque on the satellite. This torque must be counter-balanced to maintain the spacecraft's attitude.

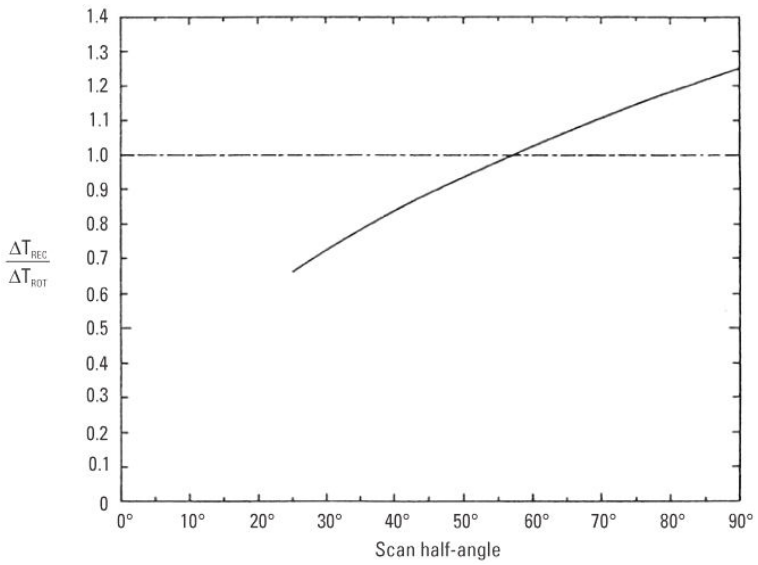

Figure 4.4.7: Trade-off between a linear scan (solid line) and a rotating scan (dashed line) [Skou and Le Vine, 2006]

As explained by Skou and Le Vine [2006], scanning disturbs the stability of the platform because the satellite system's mass is not that much greater than the mass of the radiometer system. When a linear scanner alters directions, a large amount of time must be used to allow the system to come to a halt and then to reverse direction. However, the conical scan does not require this time to reposition because it allows the satellite to turn in one direction at a constant pace, which is easier for satellite designers to implement in a design.

There is a trade-off between the line and rotating scans. The ratio of the resulting sensitivities $\frac{\Delta T_{LIN}}{\Delta T_{ROT}}$ for a radiometer in the line versus rotating case is shown in Figure 4.4.7 as a function of scan half-angle [Skou and Le Vine, 2006]. The scan half-angle is defined as the maximum scan angle in the linear case and the angle defining the useful swath in the rotating case. The point where the two lines cross is approximately 57°. The proposed system will have an incidence angle very close to this one.

Using a conical scan, three different methods of the scanning path can be used. Methods that improve the amount of data reduction required are ideal, meaning they cover the entire desired area with a minimal amount of overlap. This minimizes the amount of redundant data points and leads to fast and economical postprocessing. The traditional conical scan method can have large overlaps that require heavy postprocessing. The first option is to use a reciprocal scan which moves in both across-track directions, called a pendulum scan (see

Figure 4.4.8(a)). The pendulum scan creates a zig-zag across the path of the sub-satellite point on the earth's surface. The second option is to use a reciprocal scan can be used that moves only in one cross-track direction, called a parallel scan (see Figure 4.4.8(b)). This method returns back to the starting point by either returning after the scan is complete or by completing the revolution using an accelerated angular velocity [Kemppinen and Hallikainen, 1992]. The parallel scan creates multiple one-way paths of the sensor across the path of the sub-satellite point on the earth's surface. The third option is to use a traditional conical scan with a constant angular velocity.

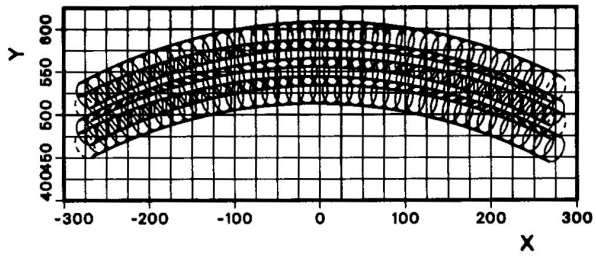

(a) Pendulum

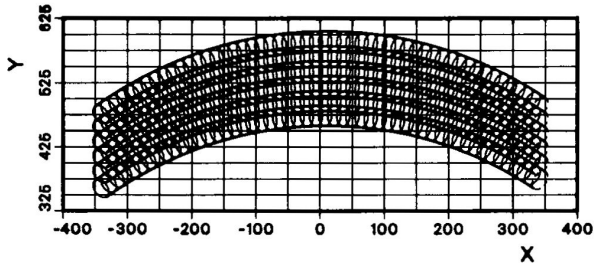

(b) Parallel

Figure 4.4.8: Conical scan method options [Kemppinen and Hallikainen, 1992]

Although the last option is the least complex with respect to the design of the attitude and control system, a study was conducted by Kemppinen and Hallikainen [1992] which found that the parallel scan was the optimal option for a scan method because it has a lower overlap amount. However, the study did not explore whether the improved scan method will lead to improved images. For our purposes, a fast postprocessing method is important so this should be further explored to determine how to achieve the most efficient data and eliminate significant processing time.

Aside from conical scanning methods, there is another option, push-broom scanning, which can be used for tsunami early-warning and detection. It has drawbacks including

multiple hardware components which will boost cost and complexity, but it may yield more efficient images. If the images are significantly improved over a conical scan, this method is more desirable because the end-user needs the most efficient method for the highest accuracy.

Push-Broom Scanner

In general, users seek a small footprint, which yields a high resolution. Small footprints mean the system must have a high frequency or a large antenna. As technology moves forward, high resolution is possible, but results in a rapid scan speed which leaves a small amount of integration time, resulting in poor sensitivity. The sensitivity problem is solved by using a push-broom sensor, where a multiple beam antenna covers the swath width while the satellite moves forward, as shown in Figure 4.4.9.

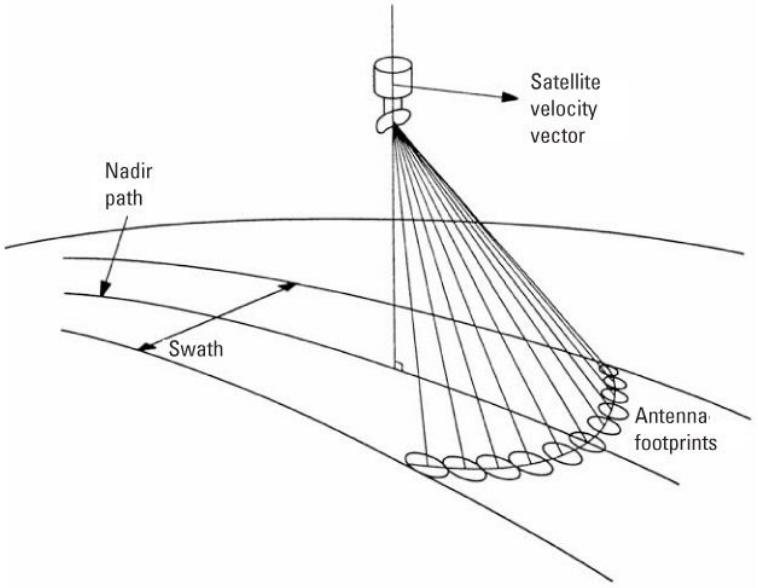

Figure 4.4.9: Push-broom imager [Skou and Le Vine, 2006]

Many radiometer receivers are connected to an equal number of feeds, outputting multiple beams to sense the earth simultaneously while the satellite moves. The two main advantages for this scanner are: (1) no moving antenna and (2) a much longer dwell time per footprint, which yields better sensitivity. The disadvantages are: (1) a complicated antenna involving a high number of components and (2) many receivers per antenna beam. However, because of technological advances that make receivers more cheap and lightweight,

this type of scanner is more feasible for a satellite designer, in both the mass budget and the cost budget for the system.

Performance analysis between rotating and push-broom scanners

Key performance factors can be computed for both a conically scanning radiometer and a push-broom radiometer. The following derivation was taken from Skou and Le Vine [2006] and goes into further detail than is presented here.

For a conical scanning radiometer, the geometry is seen in Figure 4.4.10. The maximum

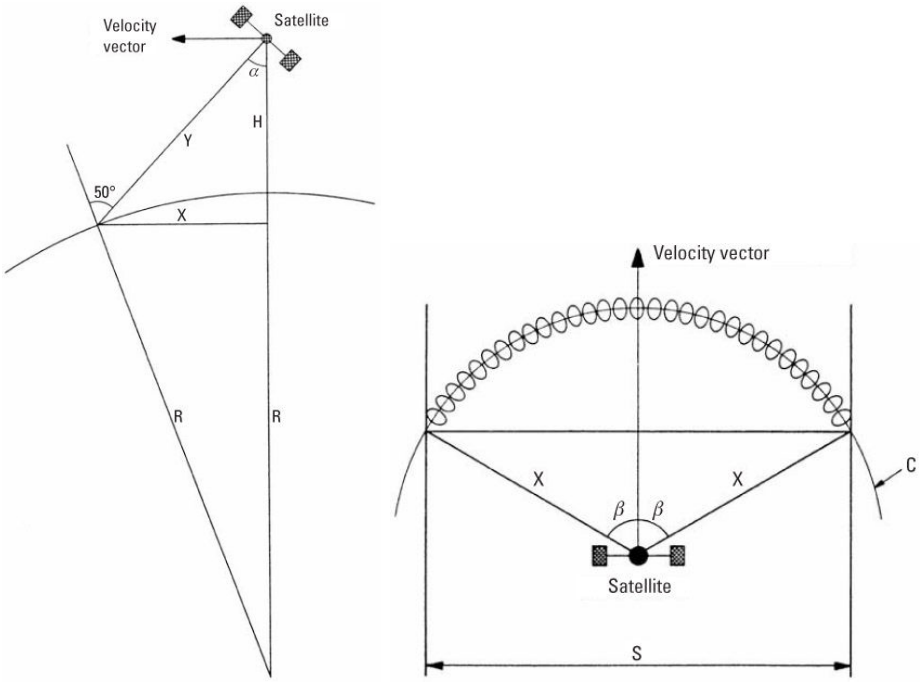

(a) Side view (b) Top view

Figure 4.4.10: Conical scan geometry [Skou and Le Vine, 2006]

useful swath can be achieved by setting $\beta \leq 60°$ as seen in 4.4.10(b). Increasing the angle past 60° results in very minimal increase in the overall swath width, even though the number of footprints increases proportionally with β. For the mechanical scanner, ground coverage with a 30% overlap was assumed for both the across- and along-track directions. This coverage would be achieved by a single receiver with one antenna beam by a rotating conical scanner having an incidence angle with the ground of 53°.

To find the maximum swath width, assuming a maximum β, we can use the following:

$$S_{max} = 2X \sin \beta_{max} \tag{4.4.7}$$

If $X = 865$ km, $Y = 1,219$ km, and $\alpha = 45.2°$, then the maximum swath can be calculated as 1,498 km [Skou and Le Vine, 2006]. The perimeter of the entire scan will be equal to:

$$c = 2\pi X \tag{4.4.8}$$

With the given distances used above, the circumference is 5,435 km. Next, the antenna 3-dB beamwidth, θ can be computed:

$$\theta = \frac{1.4\lambda}{D} \tag{4.4.9}$$

where D is the antenna diameter. If we insert the known equation $c = F\lambda$ (where F is frequency), the equation simplifies to:

$$\theta = \frac{.42}{FD} \tag{4.4.10}$$

where frequency, F, is in GHz and the antenna diameter, D, is in meters. Next the footprint sizes can be computed. The along scan direction, or across track direction, has a footprint size, FPS of:

$$FPS = Y\theta = \frac{.42Y}{FD} = \frac{511.98}{FD} \tag{4.4.11}$$

The along track direction has a footprint size, FPL, of:

$$FPL = \frac{FPS}{\sin(90 - \theta_i)} = \frac{FPS}{\sin(37°)} = \frac{850.76}{FD} \tag{4.4.12}$$

where θ_i is the incidence angle for the scanner, assumed to be 53°. The overall footprint size, FP, is:

$$FP = \sqrt{FPS \cdot FPL} = \frac{659.98}{FD} \tag{4.4.13}$$

Therefore:

$$FPS = .7758FP \tag{4.4.14}$$

$$FPL = 1.289FP \tag{4.4.15}$$

Sometimes the end-user will specify a required footprint. In this case, the antenna's diameter will be the component to solve for:

$$D = \frac{659.979}{F \cdot FP} \tag{4.4.16}$$

where the diameter, D, will be solved in meters, the FP is in km, and F is in GHz.

The number of footprints for contiguous coverage in a scan is:

$$N_{FP} = \frac{C}{FPS} = \frac{2\pi X}{FPS} \tag{4.4.17}$$

The number of swaths per second for contiguous coverage is:

$$N_S = \frac{V_{SSP}}{FPL} \tag{4.4.18}$$

where V_{SSP} is the velocity of the sub-satellite point on the surface of the Earth [Skou and Le Vine, 2006]. The velocity of the sub-satellite point is found by:

$$V_S = R \cdot \frac{g_s}{R + H} \tag{4.4.19}$$

$$V_{SSP} = V_S \cdot \frac{R}{R + H} \tag{4.4.20}$$

where g_s is the gravitational constant in km/s. For this problem, V_{SSP} is 6.625 km/s. The number of footprints per second is:

$$N_F = N_{FP} \cdot N_S = \frac{2\pi X V_{SSP}}{VPS \cdot VPL} = \frac{36034}{FP^2} \tag{4.4.21}$$

The dwell time for each footprint is:

$$T_D = \frac{1}{N_F} = \frac{FP^2}{36034} \tag{4.4.22}$$

The integration time, τ, of the radiometer is:

$$\tau = T_D \cdot .7 = \frac{FP^2}{73538} \tag{4.4.23}$$

Assuming it is a total power radiometer, the sensitivity can be calculated:

$$\Delta T = \frac{T_A + T_N}{\sqrt{B \cdot t\tau}} \tag{4.4.24}$$

Assuming the radiometer finds an antenna temperature of 230 K, has a noise temperature of 290 K, at a frequency of 20 GHz, and a bandwidth of 200 MHz. The sensitivity can be computed:

$$\Delta T = \frac{230 + 290}{\sqrt{200 \cdot 10^6 \frac{FP^2}{73538}}} = \frac{10}{FP} \tag{4.4.25}$$

where FP is in km and the sensitivity is in Kelvin. A figure-of-merit for radiometers is a radiometer constant, C, calculated for a 1-second integration time. The figure-of-merit is equal to 0.037K for these determining factors.

For a push-broom scanner, ground coverage with a 30% overlap was assumed. The coverage was conducted by a number of footprints and the identical number of receivers, N_E, covering the swath simultaneously having an incidence angle with the ground of 53°. The maximum swath, S_M, is the same as for a mechanical scanner, 1,498 km. However, there is a trade-off swath width and the number of channels, which constitutes cost. Therefore, it is reasonable to assume that the cost for the same swath would be prohibitive [Skou and Le Vine, 2006], but the calculations will continue with the equivalent swath width. The calculated swath width is a product of Equation 4.4.7 and the number of receivers:

$$S = .7 \cdot FPS \cdot N_E \tag{4.4.26}$$

The along-scan footprint is the same as for the mechanical scanner, which allows us to find:

$$S = .5430 \cdot FP \cdot N_E \tag{4.4.27}$$

where S and FP are in km. The dwell time per footprint is calculated by:

$$T_D = \frac{FPL}{V_{SSP}} \tag{4.4.28}$$

Table 4.4.1: Consideration of Important Parameters between Two Types of Scanning Radiometers

Performance Factors	Rotating	Push-Broom
Orbit Height, h	800 km	800 km
Beta, β	60°	60°
Swath Width, S	1,498 km	1,498 km
Radiometer Constant, C	0.037 K	0.074 K

From the fact that $\tau = .7 \cdot T_D$ and $FPL = 1.289 \cdot FP$, then the integration time is:

$$\tau = 0.136 \cdot FP \tag{4.4.29}$$

Assuming the receiver is the same as in the mechanical case, but using a Dicke radiometer type, the sensitivity is:

$$\Delta T = 2\frac{T_A + T_N}{\sqrt{B \cdot \tau}} = 2\frac{230 + 290}{\sqrt{200 \cdot 10^6 \cdot 0.136 FP}} = \frac{0.20}{\sqrt{FP}} \tag{4.4.30}$$

where FP is in km and ΔT is in Kelvin. The sensitivity is equal to 0.074 K for a 1-second integration time.

Table 4.4.1 shows the comparison between the two types of scanning radiometers. The push-broom has a higher radiometer constant which is one reason why this sensor was created. The comparison was conducted with an equivalent swath width for both sensors.

These sensitivities, or radiometer constants, are only guidelines and will change based on the frequency of the radiometer. However, these numbers are good for the general case of 5-100 GHz. Outside this range, the sensitivities must be calculated individually. These numbers are calculated based on a typical brightness temperature of 230 K. Figure 4.4.11 indicates that for small footprints, the push-broom is the more efficient system because the scanning system cannot give reasonable sensitivities.

4.4.3 Receiver Design

There are several types of receivers including the total power receiver and switching receivers used in the Dicke and noise-injection radiometers. The total power receiver is more simple than receivers that include a switch and has the best obtainable sensitivity properties.

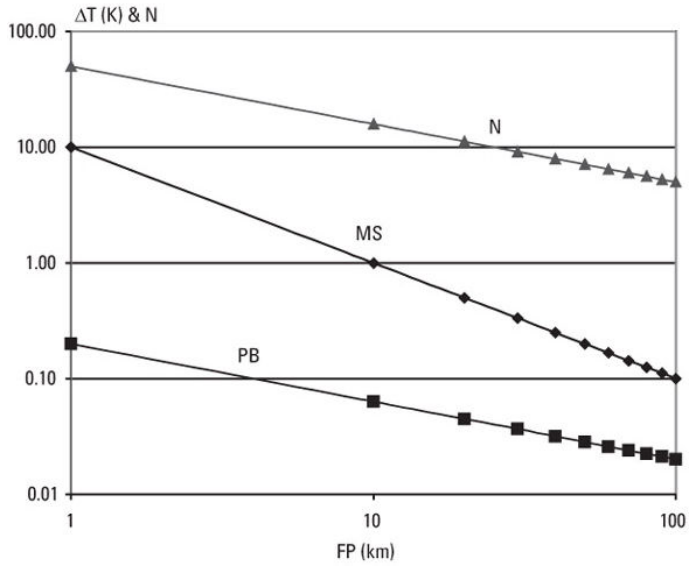

Figure 4.4.11: The graph shows a comparison between sensitivities (ΔT) and footprint for a mechanical scanner (MS) and a push-broom scanner (PB) for a sensor at an altitude of 800 km. $N = \frac{\Delta T_{MS}}{\Delta T_{PB}}$ [Skou and Le Vine, 2006]

Switching radiometers require a fast, low-loss switch in the input circuitry. However, the total power receiver is inferior to the switching receivers when it comes to stability. Because the total power receiver has stability problems, it must be calibrated very frequently, at least once per minute [Skou and Le Vine, 2006].

For scanners that are linear or rotating, the total power receiver is the best choice because the sensitivity requirement is very important. Calibration is also a simple process, which makes the total power receiver a good choice. However, for the push-broom system, the requirement for sensitivity is relaxed because there is a much lower data rate per receiver as compared to traditional mechanically moved scanners. Frequent calibration is not is difficult as all push-broom receivers are focused on sensing the earth. A well-designed Dicke radiometer or a noise-injected radiometer only requires daily calibration, so a push-broom system is the best option.

Calibration of the receiver

The transfer function of the receiver is estimated by measuring the output voltage as a function of the noise source's temperature prior to launch [Skou and Le Vine, 2006]. The noise source is connected to the receiver input terminals. The method assumes that the

receiver's transfer function is linear. If a radiometer is well designed, then it should be relatively linear. However, linearity is relative to the sensitivity and accuracy that are required. In general, both these factors are around 0.5 K [Ulaby, 1981]. Linearity is not just a factor for the receiver. The detector is the major contributor to nonlinearities. This component must also be well designed and properly loaded.

To begin calibrating, a calibration noise source is placed at the radiometer input. The output current for two known values of the antenna temperature ($T_A^{'}$) can determine the two constants, a and b, seen here:

$$I_{out} = a(T_A^{'} + b) \tag{4.4.31}$$

For some radiometer configurations, the constant b is given in terms of constant known temperature; $b = -T_{REF} = -T_0$ for Dicke radiometer types, in which case only one calibration is needed to find a [Skou and Le Vine, 2006]. However, calibration should be redundant to ensure that the proper calculations are correct before launch.

Different calibration noise sources can be used. The first is a matched load resistor whose temperature can remain constant. A hot load is usually enclosed in a temperature controlled environment and a cold load is usually immersed in a cryogenic, such as liquid nitrogen. A second type of calibration noise source are materials with known emissivities. These materials can be engineered to have emissivities near unity, making their brightness temperature close to their physical temperature [Ulaby, 1981]. Satellite sensors can use a third source, which is called cold sky, which means observing the brightness temperature of outer space, which is a constant 2.7 K.

4.4.4 Antenna Design

The main purposes of the antenna are twofold: collect emitted radiation and present it to the radiometer input. An ideal antenna has no external gain and complete gain within the field of view. This cannot be realized because of the shape of the pattern, as seen in Figure 4.4.12(a). Figure 4.4.12(b) shows a more realistic main beam, but even this cannot be realized because there are side lobes that pick up emitted energy from far away from the main beam that cannot be avoided. Figure 4.4.12(c) shows the realistic antenna pattern of the main and side lobes. The ratio between the sought energy from the main lobes and

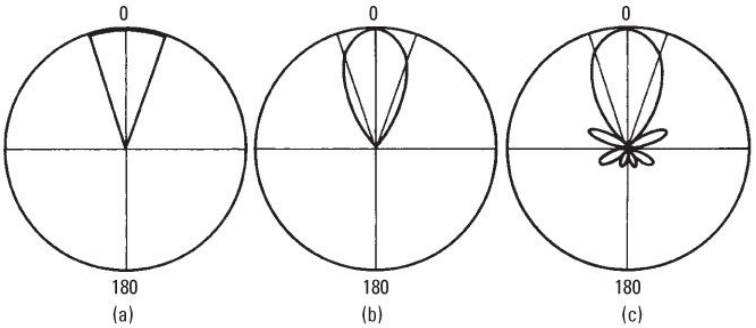

Figure 4.4.12: Antenna polar patterns; (a) idealized shape, (b) realistic main beam, (c) realistic pattern [Skou and Le Vine, 2006]

the total emitted energy collected is known as the beam efficiency, η. The 3-dB points are normally used as reference points (as a certain level on the beam compared to the peak gain) to define the beamwidth [Skou and Le Vine, 2006]. The antenna pattern in Figure 4.4.12(a) has a beam efficiency of 100%; making it ideal but physically impossible in applications.

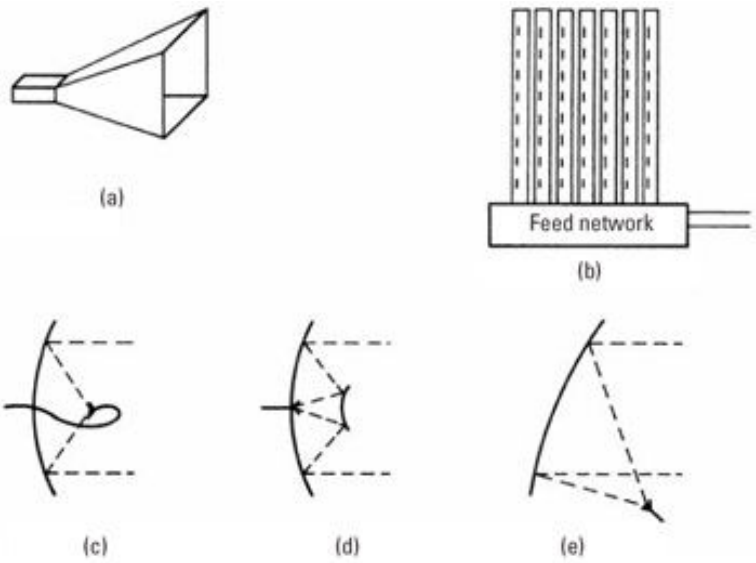

Figure 4.4.13: Antenna types: (a) horn, (b) phased array, (c) front-fed paraboloid, (d) Cassegrain, (e) offset paraboloid [Skou and Le Vine, 2006]

Different types of antennae are shown in Figure 4.4.13. The horn is generally not used for spaceborne operations. There are several different types of horn antennae, but the one shown here has a square, pyramidal shape which is not optimal. The phased array shown is a slotted waveguide array. The phased array is also not typically used in spaceborne

operations because they are lossy, one-frequency devices [Skou and Le Vine, 2006]. Reflector antennas like the ones in Figure 4.4.13(c), (d), and (e), are more ideal for space applications. Figure 4.4.13(c) shows a front-fed paraboloid which has losses in the long feed waveguide. The Cassegrain parabolic antenna in Figure 4.4.13(d) can be used but it has problems with sidelobe radiation because of the sub-reflector and the struts. Figure 4.4.13(e) shows an offset paraboloid, which is an ideal radiometer antenna for spaceborne purposes. The feed can be connected directly to the radiometer input which creates low losses and without aperture blockage.

The ideal reflector is a section of an entire parabola that does not include the vertex, as shown in Figure 4.4.14. It includes a feed horn at the focal point. The unique property of an offset parabolic reflector is that if the reflector's rotation axis is aligned with the horn antenna's axis, the antenna beam will be scanned out of the plane shown in Figure 4.4.14, but the reflector will still be properly illuminated by the feed horn [Skou and Le Vine, 2006].

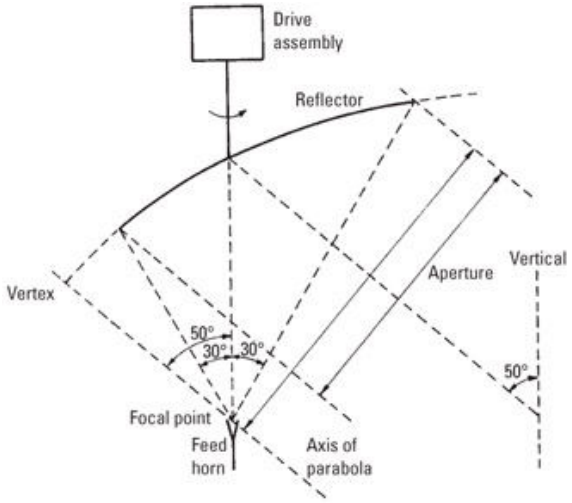

Figure 4.4.14: Offset parabolic reflector geometry [Skou and Le Vine, 2006]

When the electric aperture is roughly equal to the physical aperture, it is simple to define the beamwidth. As explained by Skou and Le Vine [2006], the 3-dB beamwidth is slightly larger than the reciprocal of the aperture measured in wavelengths of the operating frequency, as shown in Equation 4.4.32 below. This rule-of-thumb usually has a constant of 1.2, but the constant here is 1.4, reflecting the need for a high beam efficiency. This result is obtained by carefully designing the offset reflector to have a low aperture edge illumination,

making the beam wider than in other applications.

$$\theta \approx 1.4\frac{h}{\lambda} \tag{4.4.32}$$

Calibration of the antenna

In cases where the side lobe is not neglected during the image processing phase, the antenna must be calculated to determine the main-beam efficiency of the antenna. The accuracy and precision of the radiometric measurements are based on the magnitude of radiation and the main-beam efficiencies, and the accuracy by which they are known [Ulaby, 1981]. The following equation will help illustrate the purpose of the antenna calibration process:

$$T_A^{'} = \eta_l \eta_M \bar{T}_{ML} + \eta_l(1-\eta_M)\bar{T}_{SL} + (1-\eta_l)T_0 \tag{4.4.33}$$

where η_l is the antenna radiation efficiency, η_M is the antenna main-beam efficiency, $\bar{T}_{ML}$ is the main lobe contribution, $\bar{T}_{SL}$ is the side lobe contribution, and T_0 is the physical temperature of the antenna. However, increasing the main-beam efficiency requires a wider main-beam which uses a lower aperture efficiency. Therefore, there is a tradeoff between the main-beam efficiency, η_M, and the aperture efficiency, η_a.

If the side lobe contribution is negligible (η_l and η_M both equal one), Equation 4.4.33 reduces to:

$$T_A^{'} = \bar{T}_{ML} \tag{4.4.34}$$

4.4.5 Radiometer Signal Processing

As discussed above, radiometers measure the radiant electromagnetic energy from the earth's surface, the earth's atmosphere, and noise. Since noise and the ocean's radiation emissions have the same random character, the radiometer must be capable of distinguishing between the two signals, requiring the detector to be sensitive and to minimize the instrument noise. Signal processing is important because it determines the difference between the two signals.

Noise

There is a connection between the noise-like radiometric signal and the noise generated by thermal agitation of charge in electrical conductors [Ulaby, 1981]. This connection shows that the noise power from a resistor at temperature T_R, measured across a bandwidth Δf, is $kTR\Delta f$ (where k is Boltzmann's constant). The connection can also be utilized to compare the antenna temperature to the intercepted power at the antenna [Robinson, 2004]:

$$T_A = \frac{P_A}{k\Delta f} \tag{4.4.35}$$

If the losses were negligible from the antenna (loss-less), then its temperature would not matter, but the antenna will have losses. This antenna temperature should be understood as the equivalent resistor temperature required to generate the same noise power [Robinson, 2004]. The thermal high-frequency noise is overcome by integrating over many samples. To reduce the noise contribution, the samples must be spaced by a time interval, which is related to the inverse of the antenna bandwidth, $(\Delta f)^{-1}$ [Robinson, 2004]. Within a sample interval duration, t_s, the number of independent observations N is defined as:

$$N = t_s \Delta f \tag{4.4.36}$$

This can be related to the radiometric resolution for the radiometer:

$$\Delta T = \frac{M}{\sqrt{N}} \tag{4.4.37}$$

where M is a Figure of Merit depending on the design of the receiver circuits. For a scanning radiometer ΔT and footprint size are not independent. If N footprints are to be viewed across a swath of ground with a radiometer with a speed U over distance d_s, then the maximum value of the sample duration (assuming that there is 50% efficiency of useful views) is:

$$t_s = \frac{d_s}{2UN} \tag{4.4.38}$$

Therefore, the radiometric resolution is:

$$\Delta T = M \left(\frac{2UN}{d_s \Delta f} \right)^{\left(\frac{1}{2}\right)} \tag{4.4.39}$$

This can be related to the swath width, S, where the number of footprints is of the order $N = \frac{S}{d}$. This can be included in the above equation, yielding:

$$\Delta T = \frac{M}{d_s} \left(\frac{2US}{\Delta f} \right)^{\left(\frac{1}{2}\right)} \tag{4.4.40}$$

Resolution

Robinson [2004] explains how resolution plays an effect on the radiometer's signal processing, which is described here. The resolution of a microwave radiometer, β, is defined as the half-power width of the antenna main beam. This depends on the wavelength of radiation and the aperture diameter of the antenna, D, to satisfy $\beta = \frac{\lambda}{D}$ radians. For a satellite at altitude h, this results in a ground resolution or beam footprint with a linear dimension:

$$d = \beta h = \frac{\lambda h}{D} = \frac{ch}{Df} \tag{4.4.41}$$

Radiometers measuring oceanographic parameters need to operate in a frequency band of 2-10 GHz. Salinity detection is conducted between 2-6 GHz and temperature detection is conducted between 6-10 GHz, which means that the radiometer should have a wavelength between 30-150 mm. For a 25 km footprint, using a 2-GHz frequency band with $\lambda = 300$ mm on a radiometer at an altitude of 1000 km altitude, the diameter of the antenna needs to be 6 m. However, at 10 GHz, the needed diameter is only 120 cm for the same footprint.

Radiometer Calibration

Prior to launch, basic calibration of the radiometer is carried out to find the relationship between known radiometric inputs and the known digital counts. This is conducted while receivers are in a nominal environment; the radiometer sensitivity is also checked. After the radiometer is calibrated, the losses due to other components can then be calculated. Despite the rigorous pre-launch tests, the radiometer cannot expect to be perfectly stable in the harsh environment and drastic temperature changes of space. Not only can the temperature inside the radiometer fluctuate by entire degrees, but unplanned thermal gradients within the satellite can also affect the radiometer temperature [Skou and Le Vine, 2006].

To counteract the disadvantages of the space environment, the radiometer calibration should also include calibrating for different temperatures. This way, the true brightness

temperature at the antenna can be determined when the radiometer temperature is not at its nominal level. During operations, the radiometer must also be calibrated. This is conducted with the help of multiple temperature sensors imbedded within the different compartments to allow for data relay to ground.

Well known systems, like the SSM/I from NASA employ onboard calibration by a hot load/cold sky reflector layout, as shown in Figure 4.4.15. As Skou and Le Vine [2006] explain, while the antenna rotates, there are certain times when the beam of the antenna is not aimed at the useful swath. During these times, the layout of the calibration method requires the ray path between the feed and the main reflector to be interrupted by the hot load, which in turn interrupts the sky reflector. The switch shown in Figure 4.4.15 is actually theoretical, because a two-point calibration is carried out instead by using the hot load and cold sky, which is normally 2.7 K. Only the reflector is outside the calibration loop. The loss of present-day, high-performance reflectors is extremely low, which allows it to be neglected.

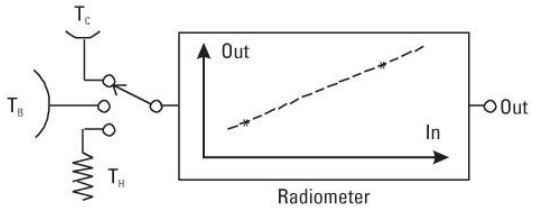

Figure 4.4.15: A hot load/cold sky reflector calibration layout [Skou and Le Vine, 2006].

Aside from pre-launch calibration, the operational calibration of the radiometer will also help improve accuracy and remove error. The calibration required and its frequency will depend on the type of radiometer chosen for the satellite constellation, as mentioned in Section 4.4.1 above.

If a total power radiometer is chosen, the calibration must be frequent to overcome stability issues with the sensor. The calibration frequency of a Dicke radiometer is lower than a total power radiometer because there is a tradeoff in sensitivity for stability, which allows the calibration frequency to be reduced. The Dicke radiometer will only need to be calibrated on the order of once per day, given its well designed components. It also only needs one, low temperature calibration point [Skou and Le Vine, 2006].

For spaceborne sensors, the most appropriate source of a low temperature calibration point is a cold sky. In the case of a scanning radiometer, the layout of the sensor has already been shown to move the antenna to point towards the cold sky. There are two disadvantages to this procedure: (1) there are moving parts and (2) the layout of the cold sky receiver and the normal antenna beam construction create complications for the architectural design of the spacecraft [Skou and Le Vine, 2006]. The first disadvantage is somewhat limited because the movement of the antenna beam is slow, the mass that is moving is small, and the procedure must be performed infrequently. The advantage to this method is that it provides a very consistent calibration. The calibration includes the total sensor and no losses or complexity in the signal path are introduced for switching mechanisms and hardware [Skou and Le Vine, 2006].

Another option for receiving the input temperature of the sky is to use a separate feed horn, and switch to its output for calibration purposes. This method may not be optimal for a push-broom system because it is proven for a single receiver system, whereas a push-broom system will have a large number of receivers.

4.5 Oceanographic Applications of Passive Microwave Data

The brightness temperature of the sea depends on a multitude of properties including frequency, incidence angle, polarization, sea surface temperature, wind speed creating surface roughness, and salinity. If wind speed is considered zero, the brightness temperature of the ocean's surface can be calculated in a straightforward way. The calculations find the Fresnel reflection coefficients knowing the dielectric constant of water by assuming that the surface is a plane boundary between water and air [Skou and Le Vine, 2006]. The calculations were conducted by the Klein and Swift computerized model maintaining an incidence angle of 53° [Klein and Swift, 1977]. The ocean's surface roughness and slope, radar cross section, surface wind velocity, and sea surface temperature all change when a tsunami is present. Because so many parameters change upon the presence of a tsunami, the detection of multiple characteristics can improve the accuracy of tsunami detection.

Based on the output of the Klein and Swift model, several key properties were noticed [Klein and Swift, 1977]. The salinity sensitivity is only high at very low frequencies, especially when accompanied by low sea surface temperatures. Salinity's sensitivity increases

with decreasing frequency, through the UHF band. In general, the detection of this sensitivity is disturbed after nearing frequencies being used by active radio services which limits the minimum salinity detection frequency band of 1.4 to 1.427 GHz [Skou and Le Vine, 2006].

Sea Surface Temperature

At the skin of the sea surface, there is a small variation in temperature due to the presence of tsunami which is typically about a few tenths of one Kelvin (K) cooler than the water temperature a few millimeters below. The change in temperature occurs over a depth of 1 mm or less and can be measured by microwave radiometry. Figure 4.5.1 shows the brightness temperature of the ocean surface with a frequency of 1.4 GHz as a function of sea surface temperature (SST).

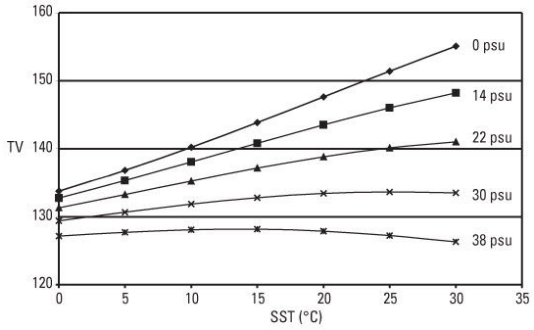

Figure 4.5.1: Vertical brightness temperature (TV) as a function of sea surface temperature with different salinities. Frequency is 1.4 GHz and wind speed is zero [Skou and Le Vine, 2006].

Note that as the temperature increases, the sensitivity to salinity also increases as the parameter lines separate by greater distances as the graph moves to the right. The large part of the earth's oceans have moderate-to-warm temperatures and high salinity that is around 35 practical salinity units (psu). Extremely northern or southern oceans and brackish waters do not meet this assumption, but for the majority of the oceans, this assumption is acceptable. With an open-ocean having a high salinity, the curves in Figure 4.5.1 reveal that the sensitivity to salinity will be at best approaching $\Delta T/\Delta S = 0.5K/psu$ for moderate-to-warm water which is above 10° C. For these conditions, the brightness temperature sensitivity to sea surface temperature does not rise above $\Delta T/\Delta SST = 0.2K/°C$. Brightness temperatures that are horizontally polarized do not respond to salinity and will

not be discussed. Brightness temperature does not only respond to salinity. It also has a dependence on sea surface roughness, which is a result of wind speed.

Sea Surface Roughness and Slope

Air flow above the ocean surface is perturbed by the presence of a tsunami. The turbulence of this air flow plays a role in enhancing velocity changes in the atmospheric boundary layer [Godin, 2004]. The sea surface slope accounts for the perturbations in the shape of the sea surface due to a tsunami. It is assumed that the tsunami is a monochromatic wave and the surface shape is sinusoidal. The determined slope is given by the derivative of the shape of the ocean surface. The overall equations are explained by Godin, which steps through the generalized Reynold's equations to show the analysis of the sea surface roughness in correlation with the presence of a tsunami. Godin determined that a change in the sea surface roughness and slope can be an indicator of a tsunami's presence, particularly with the correlation of other indicators.

Surface Wind Velocity

The model of the atmospheric boundary layer over the surface explains the changes in the air produced by the tsunami wave [Troitskaya and Ermakov, 2006]. As seen in Figure 4.5.2, the elevation of the water surface of the tsunami wave is accompanied by the reduction of wind ripples and an increase in the radar cross section (RCS). Small wind velocity variations can result in substantial variations of the RCS (about 1 dB) with conditions of weak wind. From the radiometer's standpoint, a direct relationship is assumed between brightness temperature and wind speed. This is definitely a viable assumption at higher microwave frequencies and can be verified by wind scatterometers that yield highly useful wind data. However, the dependent relationship is extremely difficult to model, unlike salinity, so experimental data is used to create models.

Brightness Temperature Response to Three Parameters in the Open-Ocean

Table 4.5.1 shows the approximated radiometer brightness temperature response to salinity, sea surface temperature, and wind speed in open-ocean, high temperature areas.

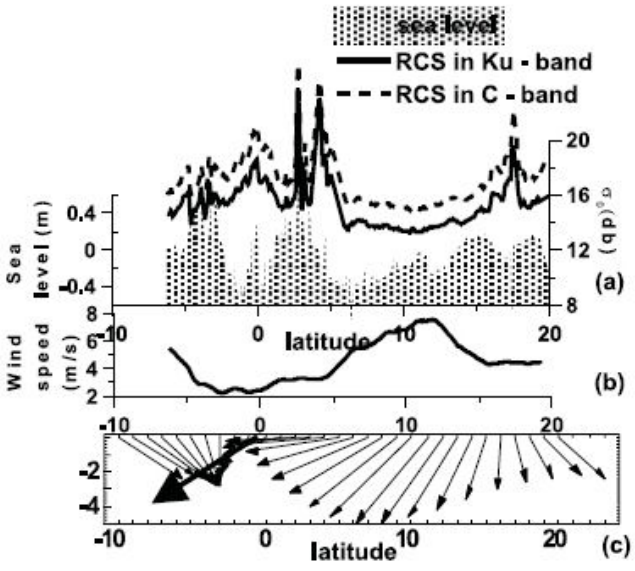

Figure 4.5.2: Latitude dependencies of parameters from the geophysical altimetry data of Jason-1 on 26 December 2004 (cycle 109, track 129) (a) Sea-level anomaly and C- and Ku-band RCS, (b) the 10 m wind speed and (c) the direction of wind speed (small arrows) and the tsunami wave propagation (large arrow) near equator according to numerical simulations [Troitskaya and Ermakov [2006] and Lay et al. [2005]].

Table 4.5.1: Brightness Temperature Response to Three Parameters in Open-Ocean, High Temperature Areas

Salinity	Sea Surface Temp.	Wind Speed
$\Delta T_B/\Delta S \approx 0.5$ K/psu	$\Delta T_B/\Delta SST \approx 0.2$ K /°C	$\Delta T_B/\Delta WS \approx 0.1$ K per m/s

4.6 Overall Ocean Measuring Potential of the Radiometer

Microwave brightness is influenced by sea parameters, showing there is potential for passive microwave radiometers to generate valuable information about the ocean. Due to the multiple interactions between the parameters, no single measurement can give information that independently detects a tsunami. Frequency bands may help determine properties of the ocean, because they limit dependence. Even with the utilization of frequency bands to determine the ocean's parameters, knowledge of sea surface roughness is required to correctly measure temperature.

If several different ocean properties are to be understood, multiple frequencies must be utilized by employing a radiometer that simultaneously scans the same field of view at multiple frequencies and polarization states. It is possible for radiometers to detect

specific variations in ocean microwave emissions that are induced by tsunami events. These variations are detectable and could be considered so-called tsunami microwave signatures. The next chapter will explain how microwave radiometers can be deployed by using a satellite constellation. In using a spaceborne system, specific advantages can be gained.

Chapter 5

Satellite Constellation Architecture

5.1 General Considerations

A constellation intended to continuously monitor the oceans for tsunami indications must provide near global coverage, since more than 70% of the earth's surface is covered by water. Since the constellation's satellites will employ passive sensors, there are no heavy power requirements which enables small satellites to be employed. Nevertheless, the total number of satellites should be kept to a minimum, in order to hold down total system costs.

One important consideration is the satellites' collective exposure to harmful radiation. The Van Allen belt of trapped radiation is a main concern. This doughnut-shaped belt lies mainly near the equatorial plane, roughly between altitudes of 1,400 and 7,000 km. Another consideration is the minimum elevation angle from points of interest on the earth to the satellite. There are indications that moderate elevation angles enhance the observed contrast that enable tsunami shadow to be seen by the naked eye.

5.2 Preliminary Constellation Design

The use of circular orbits will ease the challenges for the sensor designer in two ways. First, the sensor will be operating at a constant altitude, rather than experiencing the continuously varying altitudes typical of elliptical orbits. Second, the maximum altitude for the circular orbit will be much less than that for an elliptical orbit of the same period. Since increases in altitude put an extra burden on the radiometric sensors carried by the

satellite (particularly in achieving an acceptable resolution for tsunami-shadow detection and tracking), the circular-orbit approach appears to be the better choice.

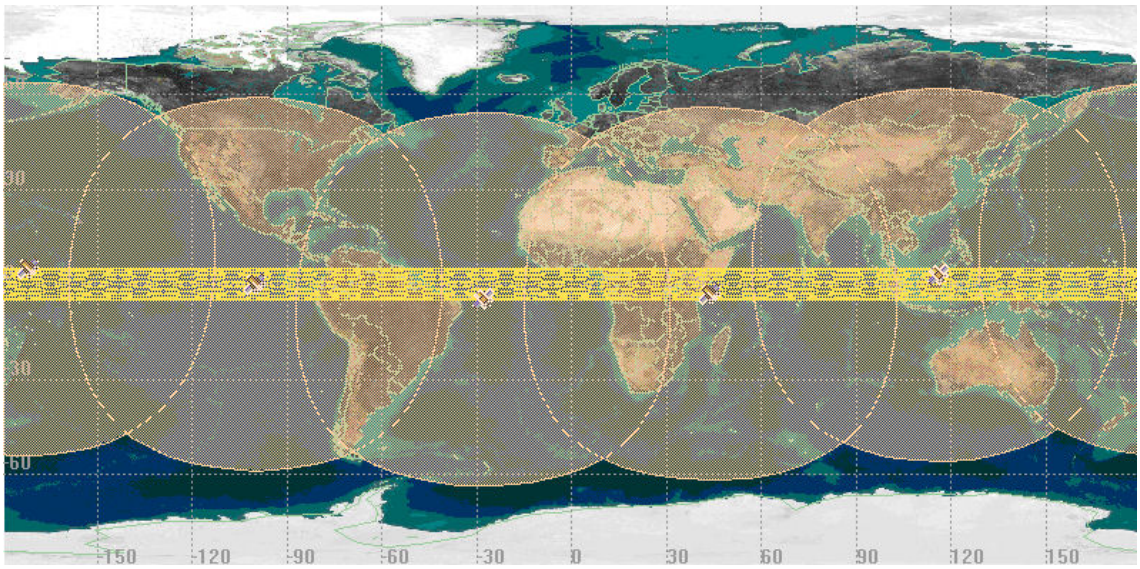

Figure 5.2.1: Tsunamisat Constellation, generated by STK^{TM}

The preliminary constellation design uses a low-inclination, moderate altitude array of circular-orbit satellites. The chosen altitude lies just above the Van Allen belt at an altitude of 8,036 km. For a number of reasons, like station-keeping and standardized operations, a repeating ground track is considered desirable. The nearest circular-orbital period for satellites lying above the Van Allen belt is 4.8 hours which is equivalent to five revolutions per day. The relatively low inclination from the equatorial plane is made possible by the large footprint of each satellite, since the edge of the footprint lies at relatively high latitudes. Also, using a low inclination angle can result in fewer satellites in the constellation. Accordingly, for this five satellite system, we have selected an inclination angle of 5 degrees, with the Right Ascension of the Ascending Nodes (RAAN) separated by 72 degrees.

Table 5.2.1: Constellation Orbital Elements

Satellite	a(km)	e	i (deg)	RAAN (deg)	MA (deg)	Ω (deg)
1	14413.8	0	5	0	0	0
2	14413.8	0	5	72	144	0
3	14413.8	0	5	144	288	0
4	14413.8	0	5	216	72	0
5	14413.8	0	5	288	216	0

A depiction of the satellites' footprints at the constellation's epoch is shown in Figure 5.2.1. The orbital elements of all of the satellites are shown in Table 5.2.1. Note that the Mean Anomaly spacing is twice the value of the RAANs. Since True Anomaly (TA) and Mean Anomaly (MA) values are the same for circular orbits the TA's may be substituted for MAs if so desired.

5.3 Alternative Constellation Designs

Other constellation designs may prove more desirable, as more knowledge is acquired about sensor capabilities and limitations, satellite attitude stability, and basic phenomenology of the microwave emissions from tsunami waves. Should these facts dictate a lower altitude constellation, one would be selected that lies underneath the Van Allen belt, with altitudes less than 1,400 km. Due to the much smaller satellite footprints, it is estimated that 24-30 circular-orbit satellites would be required in a Walker-type orbit for this lower altitude. Also, due to the much smaller individual footprint size, a small inclination angle can no longer be used. Instead, a much large inclination, say 50-60 degrees, would be required to reach the higher latitude subduction zones, and their surrounding ocean areas.

Another system, called the PARIS (Passive Reflectometry and Interferometry System) method has received good review from the scientific community [Martin-Neira et al., 2005]. This system picks up ocean-reflected signals sent from the Global Navigation Satellite System (GNSS) spacecraft, which allows the system to make measurements of the ocean surface's elevation. The sensor, however, can only measure the sea surface height at the locations where the GNSS satellites transmit their reflected signal within the antenna's field of view [Martin-Neira et al., 2005]. This is a major flaw in the system when compared with a passive microwave radiometer system, which can measure the ocean and its properties at any location in between the inclination latitudes. In addition, the PARIS concept cites a very low inclination, which prohibits it from reaching upper and lower latitudes which include Alaska, Japan, and Southern Chile. Chapter 1 explained the risks associated with these particular regions. It is imperative that these areas be actively covered by a spaceborne tsunami detection system.

Another problem is that the PARIS method works by making significant calculations of the reflected signal's geometry that are dependent on the orbit determination of not only the

PARIS method's satellite, but also the satellite that sends the signal. The increased amount of computation combined with the added error of another satellite's orbit determination is another weakness when compared to the passive microwave radiometer system explained here. Overall, The PARIS method incorporates a narrow design of the more broad passive microwave radiometry system proposed in this thesis. Therefore, the broader system should be shown at least the same amount of attention as the PARIS method from the scientific community.

5.4 Conclusion

Designing the system's constellation is an iterative process that has flexibility and can be changed right up to launch time. Historically, typical development cycles of constellations involve tens, if not hundreds, of iterations. Therefore, the constellation must take a back seat to the design of the radiometer and its requirements. The constellation can be tailored to match the maximum performance requirements of the radiometer sensor. One key item to keep in mind during the constellation design is that as altitude is reduced, the required number of satellites to cover the same area will increase.

Chapter 6

Physics Based Algorithm for Image Processing Simulation

The main goal of the thesis is to create a foundation that will lead to future studies of the tsunami early-warning and detection problem. The physics based algorithm outlines the steps required to produce a meaningful result: an image. This image will allow the end-user to examine the ocean's surface to determine the presence of a tsunami wave. The algorithm described below will be utilized to model the satellite system and sensor processing which changes the way the image looks. Overall, this foundation should be used to examine whether the spaceborne system has the capability to observe tsunami in real-time. The analysis for whether this system can determine the tsunami presence with greater accuracy and in reduced reaction time compared with the current detection system will be discussed in Chapter 7.

Figure 6.0.1 shows a general outline of the basic components to be accounted for within the specialized algorithm created here. It shows the basic steps needed to process the data points collected by the radiometer as they are manipulated to include the satellite constellation's parameters and sensor parameters. The radiometer will process the brightness temperature it detects from the ocean's surface. This quantity must then be analyzed and corrected for errors and other effects that are acting on and within the system.

First, the antenna's effects must be considered. This step can include correction for properties such as gain pattern, cross-polarization, noise, and sidelobe radiation. Our algorithm will take into account the antenna gain pattern for reasons explained in Section 6.1.

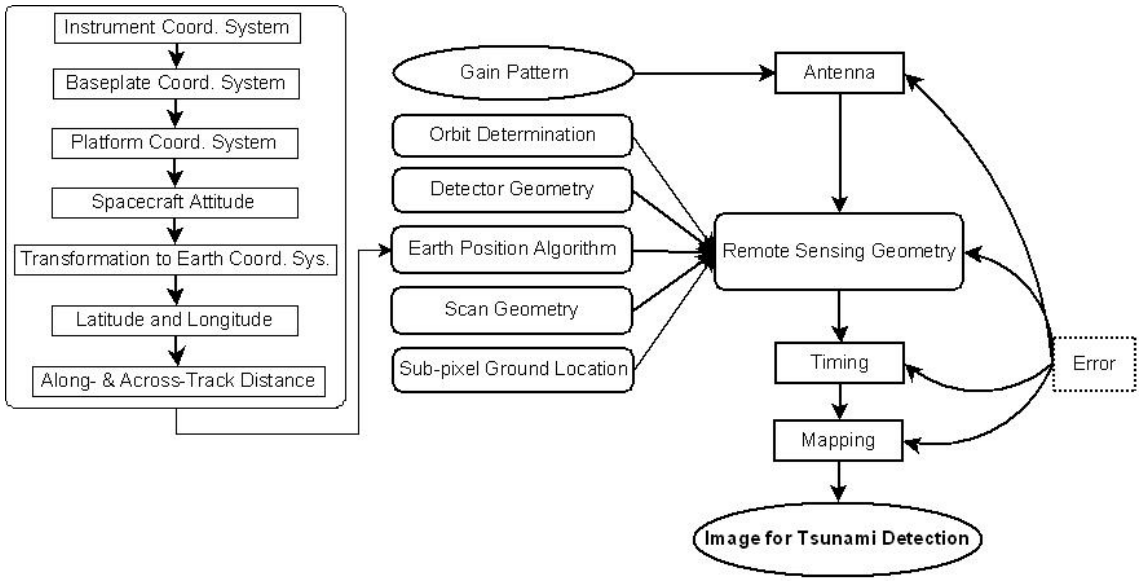

Figure 6.0.1: Outline of physics algorithm for components in simulation

Second, the remote sensing geometry of the system during detection must be considered as outlined in Section 6.2. This includes using orbit determination, detector geometry, coordinate system transformations, and spacecraft attitude to find latitude, longitude, the along-track distance, and the across-track distances. Third, the timing of the detection must be considered. This includes recording the satellite's ephemeris and computing an accurate time of detection for each pixel, which is discussed in Section 6.4. After all these items have been considered, the signature that was detected from the ocean's surface can be processed and a geographic image can be created that maps the scene (see Section 6.3). This map is the final product for the end-user of both the satellite system and also within the simulation model. Because of the multiple corrections and manipulations for the resulting image, there are many sources of error within the simulation model. These error sources will be discussed in Section 6.5.

6.1 Antenna Corrections

The spatial distribution of energy radiated by an antenna as a function of position or direction in space is characterized by the antenna pattern [Ulaby, 1981]. This pattern can change a microwave radiometer's observed brightness temperature. An antenna pattern's effects are greatest at low frequencies because a greater brightness temperature accuracy

is required and the beam efficiency is reduced. The antenna's cross-polarization effects are important as well because data from the ocean's surface unique information that could be subtly altered. Sidelobe radiation plays a role because it contributes a certain portion of the energy captured by the antenna, but may not necessarily be part of the scene being measured.

Aside from the antenna's effects, there are also a key performance tradeoff for efficiency that must be carefully made: noise versus spatial resolution. More advanced correction algorithms than the one described here also incorporate second-order corrections for several parameters that cause additional polarization coupling: attitude variations, phase of co- and cross-polarization components of the antenna pattern, Faraday rotation, and non-nominal locations of data [Njoku et al., 1980]. The algorithm used in the thesis will assume negligible cross-polarization effects, second-order effects, and side lobe radiation effects because these are not as significant.

The antenna correction algorithm requires that the input data be reformatted onto grid cells. Antenna gain patterns for a specific frequency can result in a different size or location of each pixel on the earth, but physical inversion algorithms will assume that they are at the same location. The difference in positions must be accounted for by creating a spatially consistent observation to allow for accurate data. The scanning pattern also plays a part in the correction algorithm as well. For example, a conical scan's observation density increases at the edge of the scan. Finally, all the data should be arranged in a gridded format to be used by the geolocation algorithm processing.

Multiband radiometric images are better than radiometric profiles because they show spatial variability and features of ocean hydrodynamic processes and fields through unified passive microwave radiometer pictures [Raizer, 2005a]. Each radiometer integrates through a time interval, τ, which is dependent on frequency as the antenna rotates. Therefore, the brightness temperature measured by the microwave radiometer is a time average. The brightness temperature measured by a scanning microwave radiometer, $T_I(x, y)$, can be represented as a convolution of the scene's brightness temperature incident on the antenna, T_B, with a spatial filtering function called a spread function, P:

$$T_I(x, y) = \int P(x - x', y - y')T_B(x', y')dx'dy' \tag{6.1.1}$$

The microwave contributions in Equation 6.1.1 are statistically independent and present multi-parameter functions of oceanic variables [Raizer, 2005a]. In this equation, the computation can be accomplished numerically for the accomplishment of the physics based algorithm described in this chapter. The two-dimensional spread function, P, should be determined by pre-launch measurements and analysis of the chosen antenna. Prior to launch, the antenna pattern must be measured for multiple frequencies that will be used by the radiometer. It will be a matrix that represents the spatial distributions of the antenna radiation power or the antenna pattern. The pattern can be visualized in two-dimensions or in a three-dimensional array plot using Matlab^{TM}software. Visually, the pattern will look something like what is shown in Figure 6.1.1.

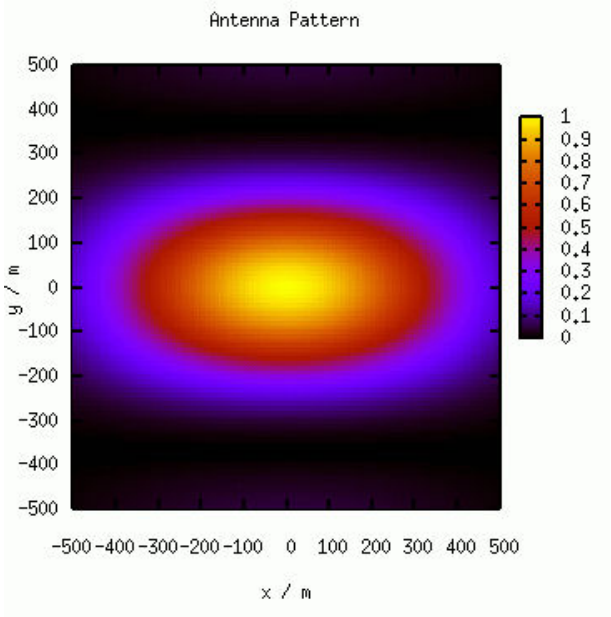

Figure 6.1.1: Antenna beam pattern as visualized in Matlab^{TM} [Raizer, 2007b]

The hydrodynamic processes that are on the ocean's surface, are captured by the antenna. As a hypothetical model example, the brightness temperature of the surface incident on the antenna, T_B, can be represented as an image in Figure 6.1.2 [Raizer, 2007b]. This figure is very similar to Figure 2.0.1 which shows the sea surface elevation at a moment in time.

For a physics based model that will be created here, the brightness temperature incident on the antenna will be specified using available hydrodynamic-electromagnetic models, as

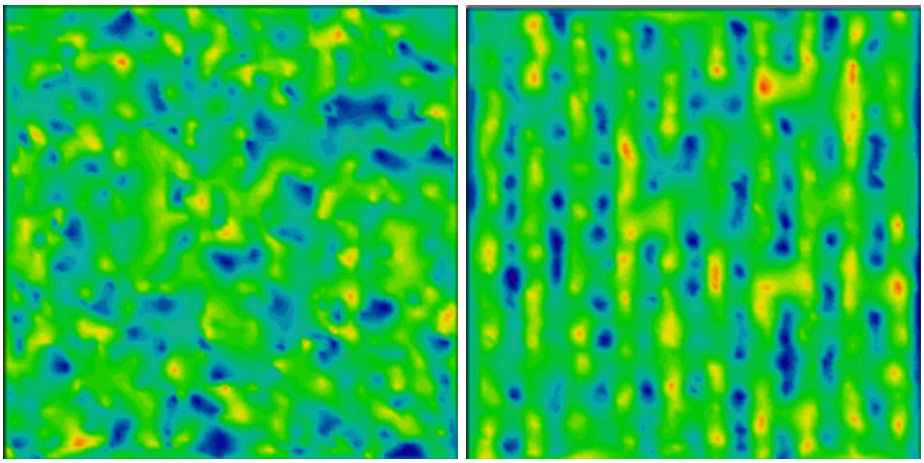

(a) Random (b) Periodic

Figure 6.1.2: A sample of the brightness temperature textures of the ocean's surface (1024 x 1024 pixels) [Raizer, 2007b]

published in Raizer [2005a]. These models are described in detail within Raizer's work, and will not be described here.

The gain pattern of the antenna describes the angular weighting of radiation incident on the antenna. The gain pattern is assumed to have negligible cross-polarization coupling. Cross-polarization, as mentioned above, will not be included because it is mainly a second-order effect. Side lobe effects are mainly important when the sensor is over a non-homogenous region. For our study of the ocean, the side lobe effects are negligible because it is homogenous and the ocean's surface has low contrast. However, for other secondary measurements of a radiometer, the effects of the gain pattern's side lobe characteristics should be corrected in order to obtain accurate measurements from the radiometer.

6.2 Remote Sensing Geometry

The overall objective of computing different quantities from an observed sample is to maintain a uniform reference format as well as to obtain information useful to the end-user to conduct scientific observations and investigations. A uniform reference format is critical to collecting and collaborating data at a later point, or in real-time, as the scanner completes many scans over the earth's surface. The quantities to be computed and stored include geodetic latitude and longitude, height above the earth's ellipsoid, satellite zenith angle, satellite azimuth, range to the satellite, solar zenith angle, and solar azimuth.

Geodetic latitude and longitude are needed to correlate the individual scans and images. These individual scans will later be assembled into a full picture to describe a part of the ocean's surface. Without the reference locations of each sample, there would be no way to assemble them together, which makes the objective of detecting a tsunami nearly impossible. The solar angles, satellite angles, and height are used during processing to account for variations, such as atmospheric correction. The ground point height and zenith angles are measured with respect to the local ellipsoid normal. The azimuth angles are relative to geodetic north.

Geometric correction is one of the most crucial stages in the pre-processing of raw satellite data. Applications using the sensor's data rely on its accuracy. For the use of tsunami early-warning, the accuracy of the tsunami's location and direction is important to accurately release information for a warning to the *correct* location. The first step in the assembly of the data from individual scans is to understand the movement of the sensor, the scanning path and behavior, and the pixel shape and size. These factors are discussed in the next section.

6.2.1 Instrument Geometric Characteristics

Two specific geometric characteristics of a radiometer are the detector and the scanning pattern. Because these are unknown at this time, we will continue to explain the algorithm for determining the geolocation of each sample, without the information from the scan and detector. Overall, the steps to correct for geometric characteristics are shown in Figure 6.2.1.

Detector Geometry

Each detector is related to a specific focal plane, as explained in Chapter 4. The plane's angles will result in further analysis to determine the sample's geometry. All the detectors from a certain band will align within the focal plane, to create the *sample*. The sample is comprised of all the information from all detectors in a specific band. If any are misaligned, this too must be calculated and determined. The best estimate of each detector's pixel in the sample will be stored and included within the geolocation data set. A single sample is the integrated signal received at the detector during the sampling interval. The sampling interval is usually the amount of time it takes the projected image of the detector on the ground to move to the next sample. For moderate resolution bands, the interval is about

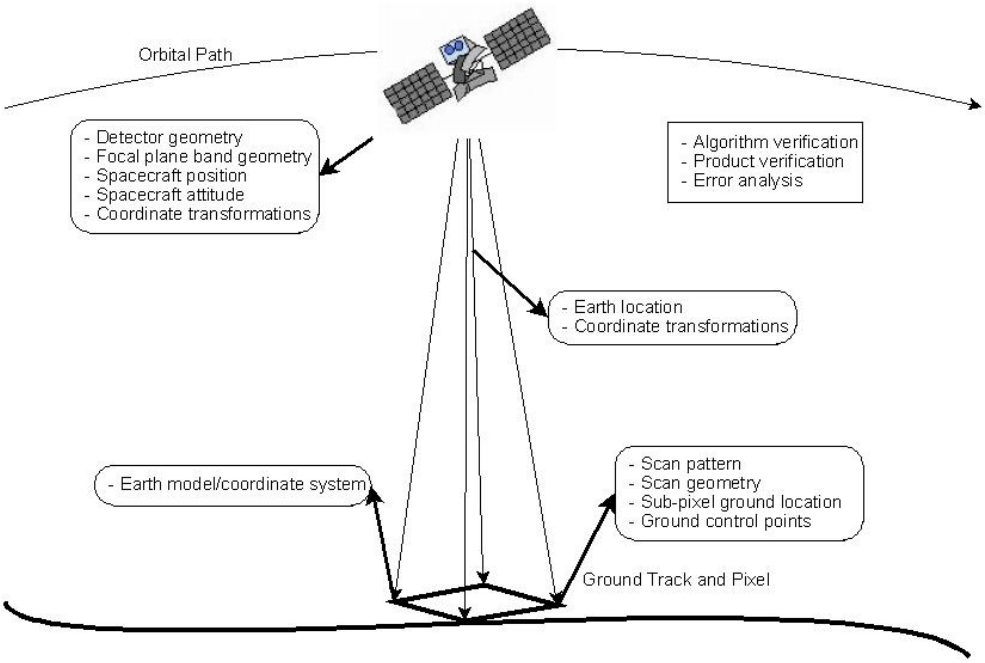

Figure 6.2.1: Overall algorithm schematic [Byerly and Storey, 2002].

88.26 μs [Byerly and Storey, 2002]. Each pixel's information must be compiled to form the sample. Individual pixels will overlap during detection; the overlapping must be accounted for during the algorithmic process.

Scanning Geometry

The second important characteristic is the scanning behavior of the radiometer. Some radiometers rotate, creating a unique pattern on the ground. Others move linearly with respect to the earth's surface. The motion of the radiometer must be measured and recorded with the geometric data to determine the instrument pointing. See Section 4.4.2 for more explanation of the different types of scanning patterns.

6.2.2 Geolocation Algorithm

Geometric correction is one of the most crucial stages in the processing of raw satellite image data. The process outlined here is explained in further detail by Byerly and Storey [2002]. Applications which use image registration, like tsunami early-warning and detection, are dependent on the geometric accuracy of images. The geolocation process begins after receiving the data recorded by the radiometer. This data includes the satellite ephemeris,

satellite attitude, and scan timing data as well as the instrument telemetry. The satellite's information is used to calculate the platform's position, velocity, and orientation as a function of time. Because the entire algorithm begins with loading data from the instrument, these pieces of information are critical to the accuracy of the images that will be produced. Other information is used, such as instrument constants and ground control points.

Instrument constants used to describe the internal geometry of the instrument within the satellite. The focal plane, band, and detector locations must be known for the instrument. These geometrical constants will be used to generate corrections for each detector in a spatial element. Optics parameters must also be stored. These include focal lengths, and the instrument-to-spacecraft alignment information. The alignment information may have a time variation if the instrument rotates. Ground control points used to validate the accuracy of the Earth location data. These points are "windows" that have well defined features with known ground locations [Byerly and Storey, 2002]. However, few ground control points exist within the scene of the deep ocean. Therefore, this type of validation may not be possible.

Relating the position in an image to a location on the earth is very important and must be incorporated within the simulation model. Pixel positions scanned by the radiometer must be derived. We must consider the curvature of the Earth and consider oblique viewing of the earth. This involves stretching each scan line from the sensor to allow for the distortion caused by oblique viewing. A vector projection method in Cartesian coordinates, described by Shin et al. [1997], is used to calculate the scanned pixel positions on the earth's surface. The first input into this method is the orbit of the satellite. The satellite orbit's determination is one of the most difficult components of the geolocation segment due to the complicated gravitation model. Nondeterministic parameters are also important, including air drag, solar particle pressure, and the earth's magnetic/electric field. The earth is formulated mathematically as an ellipsoid, using the World Geodetic System (WGS84) for the earth's ellipsoid parameters.

The pixel position procedure is a sequence of coordinate transformations. A certain pixel position on the scanning cone is calculated in the coordinate system of the instrument itself. Then the coordinate is then transformed into different coordinate systems, including scanning geometry and the orbit-Earth model. Finally, the vector from the scan mirror to the pixel is projected onto the curved earth surface in a geocentric coordinate system.

The position in along- and across-track coordinates is then calculated by spherical triangle methods. Most of this method is described by Shin et al. [1997] based on the geometric correction of Along Track Scanning Radiometer (ATSR) images.

Coordinate of the Scanned Cone in Instrument Coordinate System

Assuming a conical scan, the scan mirror of the radiometer rotates around a reference axis that will be tilted at a known angle, α. Figure 6.2.2 illustrates the instrument coordinate system $(X_a, -Y_a, -Z_a)$ and a scanned point on the bottom of the cone's circle. The Z_a axis is the reference axis of the imaginary cone. The Y_a is perpendicular to the Z_a axis and directed to the center pixel of the forward scan. The origin is located at the scan mirror, which is at the top of the cone.

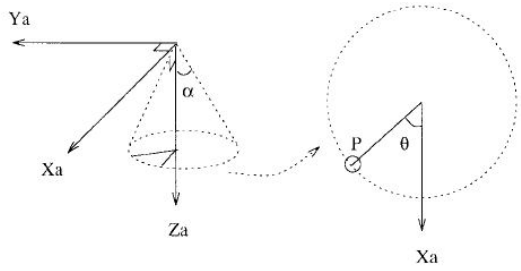

Figure 6.2.2: Radiometer instrument coordinate system [Shin et al., 1997]

In the $X_a, -Y_a, -Z_a$ system, the scanned vector is expressed as

$$P = (\sin\alpha\cos\theta, \sin\alpha\sin\theta, \cos\alpha) \tag{6.2.1}$$

Transformation to Baseplate Coordinate System

The baseplate axes $X_b, -Y_b, -Z_b$ have the Z_b axis pointing towards the nadir center point. The instrument axis are mapped onto the baseplate axes by a rotation of α about the X_a axis. The transformation matrix, M_{ab}, is:

$$M_{ab} = \begin{bmatrix} 1 & 0 & 0 \\ 0 & \cos\alpha & \sin\alpha \\ 0 & -\sin\alpha & \cos\alpha \end{bmatrix} \tag{6.2.2}$$

Transformation to Platform Coordinate System

The baseplate of the radiometer will not be precisely aligned with the platform $(X_p, -Y_p, -Z_p)$ because of human error involved. The error will be very small, but still plays a part in the geometric changes to the image, and must be included. Three successive rotations are required for correction. The transformation matrixes $M_z(\delta z)$, $M_y(\delta y)$, and $M_x(\delta x)$ are:

$$
\begin{aligned}
M_z(\delta z) &= \begin{bmatrix} \cos\Delta z & \sin\Delta z & 0 \\ -\sin\Delta z & \cos\Delta z & 0 \\ 0 & 0 & 1 \end{bmatrix} \\
M_y(\delta y) &= \begin{bmatrix} \cos\Delta y & 0 & -\sin\Delta y \\ 0 & 1 & 0 \\ \sin\Delta y & 0 & \cos\Delta y \end{bmatrix} \\
M_x(\delta x) &= \begin{bmatrix} 1 & 0 & 0 \\ 0 & \cos\Delta x & \sin\Delta x \\ 0 & -\sin\Delta x & \cos\Delta x \end{bmatrix}
\end{aligned} \tag{6.2.3}
$$

The misalignment angles for the ATSR were calculated by collating hundreds of images with different rotation angles. They are $\Delta z = 0$, $\Delta y = -0.00375$ mrads and $\Delta x = 0.0025$ mrads. It is expected that the same order of magnitude error will be observed for the new system proposed here.

Attitude Variation

The satellite's attitude variation gives geometric errors in the form of three-dimensional rotations. The matrices for correcting the errors are $M_z(A_y)$, $M_y(A_r)$, and $M_z(A_p)$ from Equation 6.2.3. The A_y, A_r, and A_p stand for the yaw, roll, and pitch angles, respectively. Since the attitude angles are only included in the information received while the satellite is operational, it is not used in the preliminary correction stage. We will use this information later to correct the data.

Transformation to Earth Fixed Coordinate System

The preliminary determination of the attitude control system is mirrored from the ATSR mission, explained by Shin et al. [1997]:

1. The yaw axis points to the local vertical of the earth.
2. The roll axis is oriented along the composite ground velocity vector including Earth rotation.

The local vertical point on Earth, $\vec{s} = \langle s_x, s_y, s_z \rangle$ can be obtained by a fourth-order equation which is solved using a numerical method. The unit vector $\vec{a} = \langle a_x, a_y, a_z \rangle$ is directed from $\vec{X_{ers}}$ (the position of the satellite in the Earth Fixed frame) to $\vec{s}$. Therefore:

$$\vec{a} = \frac{\vec{s} - \vec{X_{ers}}}{||\vec{s} - \vec{X_{ers}}||} \tag{6.2.4}$$

The composite ground velocity vector of the satellite, $\vec{V_c}$, is obtained by the local vertical points of two successive satellite positions:

$$\vec{V_c} = \frac{\vec{s_{i+1}} - \vec{s_i}}{||\vec{s_{i+1}} - \vec{s_i}||} \tag{6.2.5}$$

The projection of $\vec{V_c}$ to the plane perpendicular to $\vec{a}$ is:

$$\vec{V_{cp}} = \vec{V_c} - (\vec{V_c} - \vec{a})\vec{a} \tag{6.2.6}$$

The roll axis is, therefore:

$$\vec{b} = \frac{\vec{V_{cp}}}{||\vec{V_{cp}}||} \tag{6.2.7}$$

The pitch axis, $\vec{c} = \langle c_x, c_y, c_z \rangle$, is defined as orthogonal to both $\vec{a}$ and $\vec{b}$:

$$\vec{c} = \vec{b} \times \vec{a} \tag{6.2.8}$$

Therefore, the transformation matrix to Earth Fixed axes is:

$$M_E = \begin{bmatrix} c_x & c_y & c_z \\ b_x & b_y & b_z \\ a_x & a_y & a_z \end{bmatrix} \tag{6.2.9}$$

Projection onto Earth's surface

The vector pointing to the pixel from the surface is calculated using several transformations of the scanned pixel point P in Equation 6.2.1 [Byerly and Storey, 2002].

$$\begin{aligned} M &= \langle m_1, m_2, m_3 \rangle \\ &= M_E M_x(\Delta x) M_y(\Delta y) M_z(\Delta z) M_{ab}(\alpha) P \end{aligned} \tag{6.2.10}$$

The equation of the line of the pixel vector is:

$$\langle x, y, z\rangle = t\langle m_1, m_2, m_3\rangle + \langle X_s, Y_s, Z_s\rangle \tag{6.2.11}$$

where $\langle X_s, Y_s, Z_s\rangle$ is the position vector of the satellite in the Earth Fixed frame, and t is a variable. The equation of the earth's ellipsoid is:

$$\frac{x^2 + y^2}{R_e^2} + \frac{z^2}{R_p^2} = 1 \tag{6.2.12}$$

where R_e is the length of the major axis of the earth's ellipsoid and R_p is the length of the minor axis. The solution of Equations 6.2.11 and 6.2.12 is:

$$t_p = \frac{-B - \sqrt{B^2 - AC}}{A} \tag{6.2.13}$$

where

$$\begin{aligned} A &= (m_1^2 + m_2^2)R_p^2 + m_3^2 R_e^2 \\ B &= (m_1 X_s + m_2 Y_s)R_p^2 + m_3 Z_s R_e^2 \\ C &= (X_s^2 + Y_s^2)R_s^2 + Z_s^2 R_e^2 - R_e^2 R_p^2 \end{aligned} \tag{6.2.14}$$

The coordinates $\langle x_p, y_p, z_p\rangle$ of the pixel point on the earth's surface are:

$$\begin{aligned} x_p &= X_s + t_p m_1 \\ y_p &= Y_s + t_p m_2 \\ z_p &= Z_s + t_p m_3 \end{aligned} \tag{6.2.15}$$

Pixel geocentric latitude and longitude are calculated by:

$$\begin{aligned} latitude &= \arctan\left(\frac{z_p}{\sqrt{x_p^2 + y_p^2}}\right) \\ longitude &= \arctan\left(\frac{y_p}{x_p}\right) \end{aligned} \tag{6.2.16}$$

Along- and Across-Track Distances

For an orbit with an inclination, only finding latitude and longitude is not suitable because the scale of the images compared with those measured on the ground depends on the latitude of the sub-satellite point. The locations with very high latitude in the extreme North and South of the globe are particularly affected. Along-across track image representation requires that the pixel positions in Earth Fixed coordinates be represented in the x (across-track) and y (along-track) plane. The along-track coordinate is defined as parallel to the velocity vector of the sub-satellite point relative to fixed Earth. The across-track coordinate is measured along the great circle orthogonal to the sub-satellite track. The conversion is based on geometrical equations from the properties of a spherical triangle.

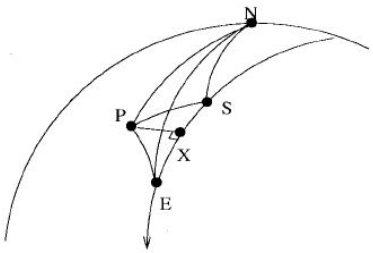

Figure 6.2.3: Spherical geometry of sub-satellite track and scanned pixel [Shin et al., 1997].

Figure 6.2.3 shows the southbound sub-satellite points and a scanned pixel points (P) on the earth's surface. The line from S to E is part of the sub-satellite track which is short enough to approximated by an arc, although in practice, the sub-satellite track is not part of a great circle. X is the point between S and E where the great circle joining P is orthogonal to the track. For the spherical triangle $\triangle N$-S-E,

$$\begin{aligned} \text{Side}(NS) &= 90 - S_a \\ \text{Side}(NE) &= 90 - E_a \\ \text{Angle}(SNE) &= S_o - E_o \end{aligned} \tag{6.2.17}$$

where the subscripts a and o represent longitude and latitude, respectively. From these three known quantities and the sine law, all six parts of the spherical triangle can be found. We can also solve $\triangle S$-N-P using the latitude and longitude of the pixel, by the same method.

To find the position of X, we first must solve the $\angle PSE$.

$$\text{Side}(PS) = \arccos(\sin P_o \sin S_o + \cos P_o \cos S_o \cos(P_a - S_a)) \tag{6.2.18}$$

From this, the other two sides can be calculated. The $\angle PES$ can be calculated by the cosine rule:

$$\angle(PES) = \arccos\left(\frac{\cos(\text{Side}(PS)) - \cos(\text{Side}(PE))\cos(\text{Side}(SE))}{\sin(\text{Side}(PE))\sin(\text{Side}(SE))}\right) \tag{6.2.19}$$

The sides PX and XE which determine the position of X and along/across track distances of P, can be acquired by Napier's laws because $\triangle P - E - X$ is orthogonal:

$$\begin{aligned} \text{Side}(PX) &= \arcsin(\sin(\text{Angle}(PES)) \times \sin(\text{Side}(PE))) \\ \text{Side}(XE) &= \arccos(\cos(\text{Side}(PE))/\cos(\text{Side}(PX))) \end{aligned} \tag{6.2.20}$$

The final coordinates (x, y) of the pixel P in the along-across track domain are:

$$x = \text{Side}(PX) \times R_e \qquad\qquad y = (Y(E) - \text{Side}(XE)) \times R_e \tag{6.2.21}$$

where $Y(E)$ is the y-coordinate of E. For the simulation, not every pixel's geophysical location must be calculated. To save computational time, the coordinates of a pixel every n number of scans should be appropriate. The user must determine how often to compute the coordinates to keep error within tolerances. The rest of the scan's locations can be calculated using linear interpolation. The smaller n is, the lower the difference between the interpolated location and the actual location of each pixel.

The information produced by the geolocation algorithm will be stored with the data points from the antenna pattern correction output. The location of each data point on the earth can then be used to map an image.

6.3 Mapping

The key point of mapping the data sensed by the microwave radiometer is to allow the end-user to gain information from the observations. This information can be gained by enhancing

the numerical data with the use of maps, histograms, contour plots, and one-dimensional transects of data. However, if insufficient data is available, no additional manipulation of the numerical data will generate useable information. Figure 6.3.1(a) shows a sample plot of the brightness temperature of the earth's surface. Another key point in data mapping is that the data behind images must be kept organized, so it will be easy to understanding what the processing algorithm is doing.

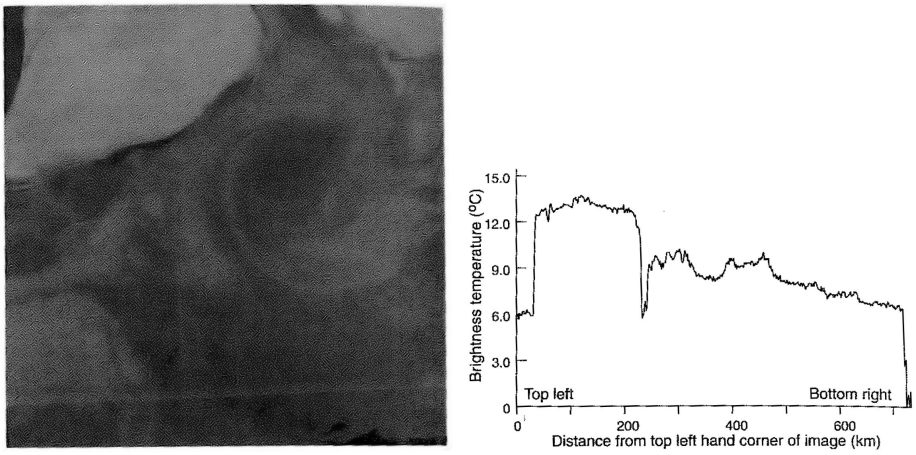

(a) Sample map of brightness temperature of the earth's surface

(b) One-dimensional transect across the diagonal of plot to left

Figure 6.3.1: Mapping samples [Robinson, 2004]

Image processing should enable the user to plot a transect of an image which makes it easier to analyze. Figure 6.3.1(b) shows a one-dimensional transect across the diagonal of the plot in Figure 6.3.1(a). Relative magnitudes in peaks and troughs shown in one-dimensional transects are especially useful in tsunami detection [Robinson, 2004]. At the completion of mapping the data, additional information can be added to help the end-user, such as latitude and longitude lines, and color addition. Easy access to the generated maps and images is imperative because quick turnaround time is very important. Labeling, referencing, and organization is essential to the early-warning system because of the limited time available for image viewing.

6.4 Timing

The overall timing of when measurements will be taken and at what frequency plays a large role in the ability of an end-user to use the data for an early-warning task. In ocean remote

sensing, it is assumed that the sensor records an average of data because measured variables change only gradually. Satellite data sets are created after the satellite track has covered the ground with enough density to enable the measured parameter to be smoothly mapped from the point measurements [Robinson, 2004]. If the user does not wish to average the measurements, a scanning sensor can be used to scan sideways along the satellite track direction. The spacing of the scan line and the overlap are important but will not be discussed here because they must be chosen by the system designers. It is assumed that the scanning occurs within the time it takes the spacecraft to advance over one footprint's distance on its track, which allows the scan line spacing to match the sensor spatial resolution. The image is constructed from individual pixels, one for each sensor measurement. The calculated location of each pixel has already been found by the geolocation algorithm, explained in Section 6.2.2.

The frequency of spatial views to create images is based on the repeat period of the satellite's orbital track. However, if the sensor has a wide swath width, there is a much higher density of observations. Because a wide swath width implies coarser spatial resolution, there is a tradeoff in the overall system design. There are a number of factors that influence the sampling characteristics of sensors on satellites. Overall, a tsunami's time scale in the ocean is the most important influence on the design of the constellation architecture. A tsunami has a very short time scale as compared to other ocean phenomena like currents and seasonal processes. Therefore, the frequency of coverage over the ocean must be fairly rapid. Designing the system for our purposes is not the only concern. Because a basic advantage to the spaceborne system is that it can contribute to other scientific fields, a study should be conducted to see what observation frequencies serve the most purposes.

6.5 Error Sources

The error of the physics based algorithm is the result of several estimations and assumptions made during the radiometric processing. There is error from antenna calibration, remote sensing algorithm processing, and mapping processing.

6.5.1 Antenna Error

The physics based model neglects the side lobe radiation. Therefore, no error will result from the main-beam efficiency because the model assumes it is ideal. In the real world, the exact determination of $\bar{T}_{ML}$ requires that η_l, η_M and $\bar{T}_{SL}$ be known. $\bar{T}_{SL}$ is not a measurable quantity and it is also not a constant because it depends on the radiation incident on the antenna from directions outside the main lobe [Ulaby, 1981]. The magnitude of the error associated with the estimated value $\bar{T}_{ML}$ due to the estimation of $\bar{T}_{SL}$ is only a function of η_M. To minimize this error, the radiometer antenna must be characterized by a main-beam efficiency that is as close to ideal as possible ($\eta_M = 1$). This can be accomplished in suppressing side lobes of the radiation pattern by tapering the aperture distribution.

Within the physics based model, there will be error associated with assumptions about the antenna gain pattern, because the actual antenna is not yet available for testing. This error is the first contributor to the change in brightness temperature yielded from the earth's surface. However, multiple antenna types can be used to create many options for the end-user and a cost-analysis can be performed with this method before an actual antenna is chosen. This will help optimize the system before manufacturing begins.

6.5.2 Remote Sensing Geometry Error

Because this section is the heart of the corrections for the earth's emitted brightness temperature, it contributes the most sources of error. First, orbit determination of the satellite is used to base all other computations. If the orbit determination information is incorrect or contains its own error, it will affect the radiometer signature. It is imperative that the orbit determination is as accurate as possible to eliminate unnecessary contributions of error. The second step is detector geometry. This step's error can come close to zero because after the detector is built, the geometry can be calculated very precisely.

The third step in determining remote sensing geometry is the Earth Position Algorithm. This step is the most complicated. Several coordinate transformations are performed through the use of angles, requiring these angles to be precisely known. After the transformations, the satellite attitude plays a role, which means the attitude of the satellite and its measurements must be computed with a low margin of error. The scan geometry should be known, which will not contribute much error.

The last step is the sub-pixel geometric locations. This step computes the geodetic latitude and longitude. However, because of the large number of pixels, it is recommended that the actual computations take place once every so often, requiring the use of interpolation. Interpolation will contribute to the error of the final product, but it is a necessary trade because of the massive amounts of data being sent to the end-user.

6.5.3 Mapping Error

Errors from remote sensing trickle down to the mapping of the sensor's observations. If there is significant geolocation error, the maps will not be accurate. In the world of tsunami early-warning and detection, this is a major concern. The maps must be accurate in order to accurately warn those at risk. Even small errors can be magnified over the large distances that a tsunami travels, affecting the accuracy of the areas in danger and the time of arrival of tsunami. Great care must be taken to accurately map the observations to eliminate costly and unnecessary false warnings.

6.6 Physics Based model conclusions

Overall, the physics-based model can yield helpful results for how the overall satellite system will work to detect a tsunami in real-time. This model will contribute to the understanding of the overall system and can aid the scientific community in working to apply new technology to the purpose of disaster early-warning and detection. It is important now to explore the comparison of the current and new systems so those at risk can be served by the most effective system.

Chapter 7

Comparison of DART II Buoy Network with Space-Based Remote Sensing Network

7.1 Advantages and Disadvantages of the DART II Buoy Network

The present detection system of buoys has several critical issues. First, the network must have buoys accurately placed near possible open ocean zones where tsunami are likely to occur [Braddock, 2003]. NOAA has increased the number of operational buoys from six in 2003 to twenty-eight in 2007. This boost was mainly the result of the Sumatra tsunami that devastated parts of the Indian Ocean region. After this precipitous event, more funding was devoted to the tsunami early-warning and detection initiative, resulting with more buoys being placed by the United States and also by other international groups like the United Nations Educational, Social and Cultural Organization's Intergovernmental Oceanographic Commission (UNESCO-IOC). UNESCO-IOC worked with other humanitarian organizations to install 25 new seismographic stations in the Indian Ocean basin [Record, 2006].

However, the buoys rely solely on the tsunameters and bottom pressure recorders (BPR) to relay the detection of tsunami wave. If the buoy communication system fails, or if the tsunameter itself fails, the system is broken. This is a single point failure that makes the system very vulnerable to the deep ocean's environment.

The buoy network also compares its detection data with nearby tide gauges. A reliance on outside data is difficult for three reasons. First, the tidal gauge data is in harm's way. For the tide gauge to detect a tsunami, it must lie in the tsunami's path. The gauge can be damaged or swept away by the outgoing tide before the onslaught of the first tsunami wave. Second, the gauge must be close enough to the tsunami's original location for the warning to be issued in plenty of time for those in danger to help themselves and leave low-lying areas. Third, the tide gauge's reading may be complicated by the shape and size of the basin where it is located. The tide gauge is affected by geographical features like the continental shelf, coastline, and harbors.

The buoy network has an advantage in that the buoys and tsunameters can be placed by human hands, and can be revisited at any time. However, the only way to be sure that the entire ocean is monitored is to continue to boost the number of tsunameter systems in the ocean. This will take a massive amount of resources from the UNESCO-IOC and other national governments, allowing the cost to continue to rise.

7.2 Advantages and Disadvantages of the Space-Based Remote Sensing Network

The satellite network will rely on the principals of physics to continue orbiting the globe and monitoring the ocean's surfaces. The advantage to this system is that it will be capable of monitoring the entire ocean. It also has the capability of contributing to more than just tsunami early-warning and detection. Satellites carrying microwave radiometers collect data for scientific studies about climate change, sea ice changes, pollution and contamination, oil spills, and more. The spaceborne system can aid in data collection for many scientific uses which makes it more beneficial than the buoy network. A disadvantage is that currently there is no capability to revisit the spaceborne system if something goes wrong onboard the satellite.

7.3 Comparison of Two Network Systems

The Massachusetts Institute of Technology (MIT) Space Systems Laboratory developed the Generalized Information Network Analysis (GINA) methodology for distributed satellite

systems [Shaw, 1998]. A distributed satellite system uses multiple satellites that operate in a coordinated way to complete a mission or task. GINA allows a comparison of different design architectures, treating them like modular information processing networks. GINA uses a quantitative analysis and specifies metrics for the cost, capability, performance, and adaptability. These metrics can be used to address sensitivity of performance and cost when there are changes in system components [Jilla, 2002]. The methodology analyzes newer architectures and can reduce risk. The following steps describe the GINA methodology, which is used to quantitatively design and compare architectures for a prediction of their performance. The GINA methodology was outlined by Jilla [2002] and examined by Shaw [1998] and their ideas are outlined here.

7.3.1 Identify Mission Objectives and Conceptual Design Phase (CDP) Objectives

For the case of either a satellite system of sensors or the current network of DART II Buoys, the customer is typically a country's government situated near tsunami prone subduction zones. Secondary customers include the space science community receiving scientific data, which prefers a system that generates a large amount of quality data. Because the financing for a tsunami detection system mainly comes from governments, a third customer is the taxpayer community, who would obviously prefer the least expensive effective system. The mission objective in both cases is the same:

- To accurately detect a tsunami as quickly as possible to disseminate the information to civilians in areas susceptible to the tsunami. Specifically, to detect a tsunami as quickly as possible after an event using the highest accuracy possible to determine its direction and possible height.

The customer requirements are that the local civilian authorities receive the information as quickly and as accurately as possible, to maximize reaction time and minimize the number of false warnings. The CDP objective is:

- To develop a methodology for the comparison of an architecture consisting of microwave radiometers onboard a constellation of satellites with the current architecture consisting of a network of DART II Buoys.

7.3.2 Transforming a System into an Information Network

GINA compares the two systems by equating the systems to a corresponding information network. For the spaceborne system, the origin is the ocean surface. For the buoy network, the origin is the ocean bottom. The destination for both systems is where the data is analyzed, either at a ground station, or at a control/data center. The network must be tracked to determine the imaging rate, accuracy, and cost. Transforming the individual system into an information network will also require probability models predicting network failures over the lifetime of the mission.

Quality of Service Metrics

Four parameters describe the quality of service provided to customers at an instantaneous point in time: signal isolation, information integrity, information rate, and availability of services over time [Shaw, 1998]. The four parameters serve as the minimum instantaneous capability requirements the system must meet to satisfy the customer. The customer will analyze the entire systems quality by these measures.

1. Signal Isolation

   A system's ability to isolate and identify signals from sources within the field of view is critical to the mission of tsunami detection. For a satellite system with microwave radiometers, the system's angular resolution determines the smallest field of view the radiometer can image and discriminate. For the DART II buoy network, the systems tsunami detection algorithm determines the ability to detect the tsunamis signal.

2. Information Integrity

   The information quality transferred through the network is quantified as the bit error rate for the DART II buoy network. For a satellite system, the integrity is a function of the signal-to-noise ratio required to obtain the image. The information's quality is extremely valuable because false warnings are very costly and create difficulty when the warning is then real.

3. Information Rate

   The rate, typically measured in bits per second, measures how fast information moves between the origin and the destination. This is of the utmost importance for the

Table 7.3.1: Comparison of the Quality of Service Metrics

Capability	Satellite System	DART II Buoy Network
Isolation	Angular Resolution	Reliability of Tsunami Detection Algorithm
Integrity	Signal-to-Noise Ration	Bit Error Rate
Rate	Images per Unit Time	Bits per second
Availability	% Time in Use	% Time in Use

tsunami problem due to the time constraints associated with a pending arrival of a tsunami wave. The rate is measured in images per unit time from the ocean surface for a satellite system. The DART II system's information rate is measured in bits per second from the ocean bottom relayed by the acoustic modem between the tsunameter and buoy [Meinig et al., 2005b].

4. Availability of Services

   Availability characterizes the probability that information is being transferred through the network between all nodes [Jilla, 2002]. Actual imaging time over the ocean versus the time over land or the time to complete tasks such as calibration or retargeting affects the availability of the system. The buoy network's availability will depend on the time it is operational versus time it is disabled due to mechanical failure, weather, or malfunction.

The quality of service metrics will vary based on the type of system and the parameters of that system. Table 7.3.1 shows the breakdown of each service metric's respective quantity with respect to the two systems [Shaw, 1998].

7.3.3 Develop System Metrics

The performance, lifecycle cost, cost per function, and adaptability metrics by which all proposed system architectures will be evaluated and compared must also be defined for both systems.

Performance

This metric measures how well the architecture satisfies the market demands over the life of the mission. It is based on the differences between the quality of service metrics. Because the

information rate, signal isolation, and signal integrity requirements are all distinguishable between the two systems, these requirements will all be used to determine the system's overall performance. To calculate performance, each system's points of failure must be analyzed. GINA uses a Markov reliability model to evaluate the reliability of a complex system. The model will determine the likelihood that the system will continue to function over a given amount of time and the likelihood that the system will continue to function in partial failure states [Shaw, 1998].

Lifecycle Cost

Three primary cost categories are hardware development (satellite buses or buoys), system deployment, and system operation. Secondary cost trades exist within the intersections of these primary categories. Autonomy can increase design costs but will lower operational cost later in the mission. Satellite payload distribution can use a learning curve, decreasing overall design costs. Learning curves can also be utilized for the tsunameter and buoy production. The launch costs associated with the DART II System will be calculated from the cost of the equipment needed to reliably deploy the buoys and tsunameters. The satellite launch costs will be based on the costs from the launch vehicle. The hardware costs will be inherently different for each system.

Cost per Function

This cost provides the cost performance metric for the system. It is computed by dividing the Lifecycle Cost by its lifecycle performance. For example, a communications system would have a cost per function of cost per billable minute. For a satellite observational system involving detecting tsunami, the cost per usable image would be analyzed.

Adaptability

This metric can be thought of as the system's sensitivity or ability to overcome incremental changes in the requirements. It can also be thought of as a system's flexibility to new requirements.

7.3.4 Partition the Conceptual Design Problem and Develop Simulation Software

To partition the design problem, variables should be defined and included in two vectors. The design vector contains the key independent variables that the system engineer has control over. The constants vector contains the remaining variables. As Jilla describes, the design vector can be put into a matrix against the capability metrics of the system, which will result in a matrix showing associated trades within the system.

7.4 Conclusion

The comparison is a critical step for understanding which system is most effective and for understanding each system's strengths and weaknesses. The comparison will also be a critical component for the debate over tsunami detection systems. The next chapter will describe the system needed international to describe the early-warning system as a whole.

Chapter 8

Early-Warning Capability and Disaster Risk

The physics based model described in Chapter 6 plays a main role in helping those at risk prepare for a threat with enough response time to protect themselves and others. However, this model is not the entirety of the early-warning system.

8.1 Early-warning system architecture

Traditionally, early-warning systems are linear in shape and are usually end-to-end systems that focus on the hazard and the steps taken in between detecting a hazard and warning the end-user (see Figure 8.1) [Basher, 2006]. The linear system makes forecasts and warnings relevant to end-users. The system has a particular model at its heart and pays particular attention to the time evolution for the geophysical process. The Chapter 6 model could be the very same component as the model in the end-to-end system. Currently, the tsunami early-warning system is based on statistical relationships with precursor seismic observations but the latter component does not allow the accurate prediction of oceanic response [Basher, 2006]. The probability characteristics are poorly known so the false warning rate is high.

The linear system has many shortcomings, some of which have been highlighted in recent disasters such as Hurricane Katrina and the Sumatra tsunami. The following outline of the linear system difficulties are taken from Basher [2006]:

1. The system should be mainly focused on the safety of people, instead of the hazard.

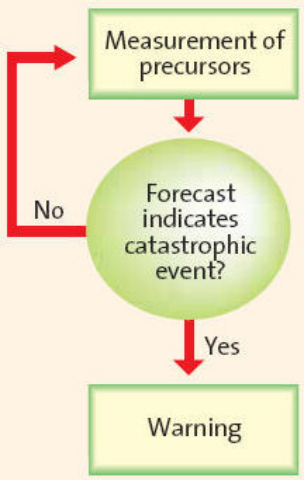

Figure 8.1.1: Three phases of early-warning systems [Villagran de Leon and Bogardi, 2006].

2. There is little engagement with the end-user.

3. Different hazards are dealt with by different communities, without seeking mutual benefit or synergy [Basher, 2006].

4. The system is dominated by experts, who are not directly in harm's way. End-users may not thoroughly understand the problem, the warning, and the appropriate response to the warning.

5. The role of research outside the core physics area, such as social science and health, is not acknowledged [Basher, 2006].

6. There are few systematic mechanisms designed to improve the system.

7. Weak public engagement brings on weak political and monetary support.

Because of these weaknesses, the system should be overhauled. Not only should a very accurate model be created from the geophysical process, but other areas of concern should also be incorporated to increase the safety of those in harm's way, no matter what the risk.

The first problem is the one that should be fixed first. This means that those at risk must be interacted with, the needs of at-risk communities must be analyzed, town meetings and community involvement must be conducted to improve the understanding of response behaviors, public information tailored to specific communities and cultures must be disseminated, people-focused benchmarks and performance standards for technical warning

services must be created [Basher, 2006], formal mechanisms must be constructed to allow public representatives to oversee and monitor warning systems, and surveys must be conducted regularly to understand the public's view of early-warning and how it can be improved. By changing the role that the end-user plays in their own safety, the other difficulties can be fixed to increase safety again. It can be a positive-feedback system.

Changes to the linear system must be taken concurrently by many organizations including the government and non-profit entities. Coordinated response and precursor actions will drastically improve the safety of at-risk communities. As such, an integrated early-warning system should be adopted to improve the linear system. The integrated system will have two added factors. First, those who are not regularly associated with disaster response, including politicians and community leaders, should be included. Second, multiple links and feedback paths must be included, especially from individual communities, to help create communication lines with the end-user to those who are creating the new system.

This level of communication is important to understand how subtle changes in various components of the warning system can affect an at-risk community. Overall, the physics based model can also be improved to include particular situations of countries to better specify lower level community players or the technical roles of different institutions. Cost analysis should also be included to expose areas which need creative response and resourceful thinking in order to accomplish the task. Overall, the risk of a tsunami or any natural disaster poses a major threat to non-developed and developed communities alike. This can transfer into a considerable threat to national security for any country and affect economic development.

8.2 National Security

Besides a tsunami's creation of economical and national security concerns, the creation of a new, shared disaster warning system is also a problem. Nations cite the sharing of technical information and networking as a security risk. Intelligence experts suggest that some data could be sensitive, particularly from space (visual images), which can compromise national intelligence gathering efforts [Morrissey, 2005]. Some nations, such as India, still maintain proprietary rights to all real-time satellite data.

So far, despite these concerns, there was still an international response to the tsunami disaster in 2004. The response included monetary help, military response in recovery efforts, and political proposals to improve the warning system in place.

8.3 International Response

Monetary support was the initial way most countries assisted the affected countries from the Sumatra tsunami. Many nations (including Australia, United States, Great Britain, Japan, and Germany) chose to show "soft-support" by donating funds [Huxley, 2005]. Some nations who pledged funds also assisted with "hard-support" which is a military response, like the United States, Australia, and Japan.

On January 6, 2005, the United Nations Environment Program (UNEP) announced an international effort to develop a tsunami early-warning capacity for nations bounding the Indian Ocean [Morrissey, 2005]. Some individual governments volunteered to patrol and guard their own coastlines to assist in the international effort. A few United States Congressmen and Senator Joe Lieberman also proposed global warning systems. Senator Lieberman's proposed adding to the existing six buoys that were in the ocean at the time of the Sumatra tsunami. He proposed increasing the number of buoys to fifty. At this time, there are presently 39 planned or positioned buoys in the global oceans.

As expected, international agreement and cooperation will be difficult for a number of reasons. First, different countries have separate priorities which make agreement extremely unusual. Second, funding is currently difficult to obtain. Third, nations with proprietary rights may require payment for satellite data. In addition, there are also concerns about compromising national intelligence.

However, the disaster response and the early-warning system must be completed in order to improve the safety of those in at-risk areas. A global system that includes multiple agencies, governments, and types of technology is mandatory for increased reaction time. Helping those who need support and live in volatile areas where tsunami occur is worth the difficulty in achieving a global system. The next chapter outlines the overall conclusions reached from the research of this thesis and how to proceed in the future to improve the ability of a spaceborne network to determine the presence of a tsunami in the open ocean.

Awareness and interest in disasters and early-warning systems is high and the time is ripe for bold action to implement the globally comprehensive, systematic, and people-centered early-warning systems for all hazards and all countries that former UN Secretary General Kofi Annan called for in January 2004 [Basher, 2006]. The next chapter discusses the overall conclusions from the thesis and its proposal. It also outlines what to do next in order to continue solving the problem of how best to create a safe and secure system for those in harm's way.

Chapter 9

Conclusions and Future Work

There exists the potential for tsunami detection from a satellite utilizing microwave radiometers. Because of this potential, tsunami detection and early-warning systems should be analyzed to investigate the benefits and trades of conducting surveillance and monitoring of the deep ocean from space. The proposed microwave radiometer system represents an extension to the radiometers onboard Jason-1, the proposed National Polar-orbiting Operational Environmental Satellite System (NPOESS), and NASAs Terra satellite. Some of these satellites carry operating radiometers and even observed the 2004 Indian Ocean tsunami. The advancement of knowledge about radiometers can also improve sensors deployed in the past to make tsunami early-warning and detection more successful.

The importance of a complete system for tsunami early-warning and detection cannot be emphasized enough. The spaceborne system can be used to monitor more than the oceans and can benefit many different scientific fields with coordinated data sets. Overall, the spaceborne system has more potential to witness the initial event that creates a tsunami because it will monitor the entire ocean. Because of the potential in a spaceborne system, not only can tsunami be more efficiently detected, but alternate areas can see progress and additions to their field's database network.

The disaster risk associated with tsunami makes it imperative that the new system have a chance to prove its worth. Those at risk rely on the ethical evaluation of the tsunami detection system. They trust that the scientific community is conducting research for this topic with the true value of human life at heart.

9.1 Conclusions

This thesis supports the use of a spaceborne system of radiometers to effectively monitor the whole of the earth's oceans. The outcome of research can provide a new, applicable system to save lives and increase the warning time for vulnerable communities. The long history of tsunami shows that it is time to put new technology to use to help those at risk create safety nets and add to their security. The physics based model relies on the underlying background physics of ocean waves. Tsunami in deep water are difficult to detect because they have a long wavelength and a small amplitude. Their journey towards shorelines is affected by the laws that bound their behavior. The waves will eventually grow in height, slow, and shoal. It is their behavior close to shore that is familiar because of the Sumatra tsunami of 2004.

Tsunami are currently detected by a network of tsunameters, seismographs, and tide gauges. This network is proficient, but has weaknesses. It cannot effectively warn threatened communities in all cases because of the locations of the sensors. It is vulnerable because it has two one-point system failure. First, if the acoustic link from the tsunameter and the buoy fails, the buoy is not operational. Second, if the link from the buoys to the communication satellite fails, the buoy is no longer operational. These failure cases are critical because a failed buoy could be the only buoy that detected the tsunami, which makes the entire network unable to detect the tsunami. For all these reasons, a new satellite constellation of passive microwave radiometers can be used to detect tsunami waves. The new system can take advantage of the advances in microwave technology since the 1930s.

Besides contributing effort to preventing devastating tsunami, the system will also be available to observe the ocean for rogue waves and other oceanic changes. For example, radiometers can monitor the oceans changes with respect to global warming due to their ability to detect sea surface temperature. They can also detect changes to the surface such as an oil spill or other types of environmental contamination. The radiometer system can contribute daily to the knowledge of the oceans.

To determine if the proposed system will be feasible, a simulation model is suggested that will create a simulation of what happens to the surface's brightness temperature after being intercepted at the satellite sensor. This system can highlight the strengths of the system and also illustrate its weaknesses, which can be somewhat deemphasized through

careful design. The simulation can then be used to create a GINA model to compare the proposed system with the current system of tsunami detection [Jilla, 2002].

The comparison of the two systems will translate the systems into comparable information networks. The result of the study should show which system is more effective and more desirable for the task of tsunami detection and early-warning. The study will culminate in the comparison, which can be used to illustrate the reasons why one system is more advantageous than the other and also is a method for entering the debate about tsunami detection systems.

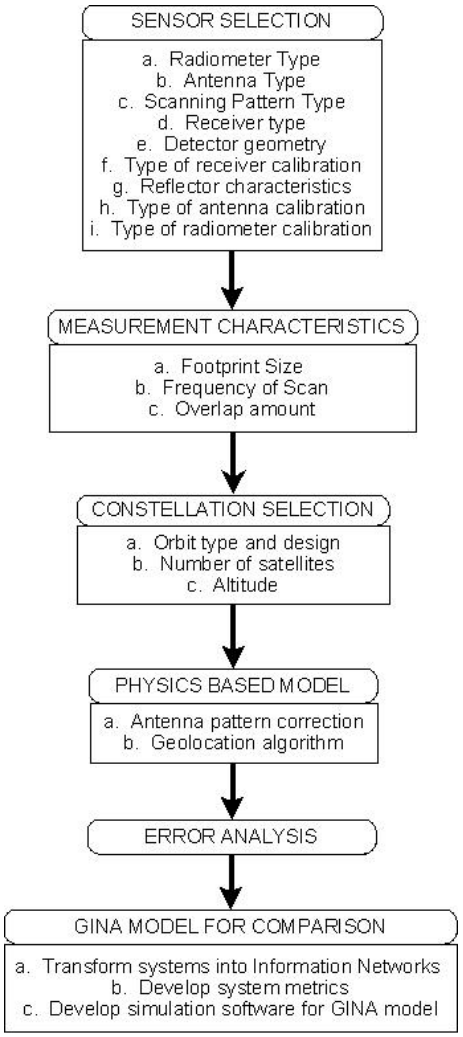

Figure 9.1.1: Simulation Tools Development Plan

9.2 Future Work

A Simulation Tools Development Plan shown in Figure 9.1.1 outlines the needed steps to continue analyzing spaceborne radiometry for the application of tsunami early-warning and detection.

Many of the items in Figure 9.1.1 include multiple analyses to determine key parts of the system. Some of the analyses should be optimization studies to determine what type of radiometer or what type of receiver can best facilitate tsunami detection from the ocean's surface. Other options such as the footprint size, scanning pattern, and frequency bands should be chosen after an in-depth analysis is conducted to determine which best suits the tsunami detection purpose. After the key components are chosen, a complete analysis utilizing the GINA model must be conducted [Jilla, 2002]. The GINA model will allow the systems to be compared analytically, to see which system would best benefit the communities at risk and flesh out key trades. The model would also recommend a system that has the best capability of detecting tsunami in the deep ocean. Finally, a physics based simulation model should be constructed to represent the real-world situation. This simulation can better show the differences and similarities between the architectures from the GINA model.

Overall, the work done in the future to further the study of a new system for tsunami early-warning and detection can only increase the understanding of dangerous tsunami waves and their properties. The communities at risk will benefit greatly from the study of detection systems. If the new system is shown to hold improved abilities, hopefully the system can be implemented by the will of the political and scientific communities to help out millions of human lives living in the shadow of tsunami risk.

Chapter 10

Appendix A: Tsunamisat Website

The background readings and references used as resources for this thesis can be found at `http://stellar.mit.edu/S/projects/tsunamisat`. This is a project website held by the Massachusetts Institute of Technology.

Bibliography

Amateur Teleseismic Network, 2007. URL `http://teleseismic.net/aboutearthquakes/`.

National Geophysical Data Center, 2007. URL `http://www.ngdc.noaa.gov/`.

United States Geological Survey, 2007. URL `http://earthquake.usgs.gov/research/structure/crust/index.php`.

P.-C. Athukorala and B. Resosudarmo. The Indian Ocean tsunami: Economic impact, disaster management and lessons. Technical report, Austrailian National University, 2005. URL `http://ideas.repec.org/p/pas/papers/2005-05.html`.

B. Barish, K. Ford, K. Droegemeier, L. Lanzerotti, and G. W. Clough. Hurricane warning: The critical need for a national hurricane research initiative. Technical report, National Science Board, 2006.

R. Basher. Global early warning systems for natural hazards: systematic and people-centred. *Philosophical Transactions of the Royal Society A*, 364:2167–2182, 2006.

J. Berkhoff. Computation of combined refraction-diffraction. In *Proceedings of the Thirteenth International Conference on Coastal Engineering*, 1972.

J. C. Borrero. Field data and satellite imagery of tsunami effects in Banda Aceh. *Science*, 308:1596, 2005.

R. D. Braddock. Sensitivity analysis of the tsunami warning potential. *Reliability Engineering and System Safety*, 79:225–228, 2003.

E. Bryant. *Tsunami: the underrated hazard*. Cambridge University Press, New York, 2001.

D. Burrage, M. Goodberlet, and M. Heron. Simulating passive microwave radiometer designs using simulink. *Simulation*, 78:36–55, 2002.

W. Byerly and J. Storey. Geolocation: Visible and infrared imager radiometer suite algorithm theoretical basis document. Technical Report Y3258, Raytheon Company, March 2002. URL `http://140.90.86.6/IPOarchive/SCI/atbd/msoBDD36.pdf`.

A. Camps, J. Font, and M. Vallllossera. From the determination of sea emissivity to the retrieval of salinity: recent contributions to the SMOS mission from the UPC and ICM. In *IEEE International Conference on Geoscience and Remote Sensing Symposium (IGARRS)*, 2006.

P. Cefola, R. Proulx, R. Metzinger, M. Cohen, and D. Carter. The Radarsat flight dynamics system: An extensible, portable, workstation-based mission support system. In *AIAA/AAS Astrodynamics Conference*, August 1994.

I. Cherny and V. Raizer. *Passive microwave remote sensing of oceans*. Wiley, New York, 1998.

P. Dias, R. Dissanayake, and R. Chandratilake. Lessons learned from tsunami damage in sri lanka. In *Proceedings of Institution of Civil Engineers*, volume 159, pages 74–81, May 2006.

S. Donnan. Java tsunami exposed flaws in warning system. Finanical Times Ltd, August 2006.

J. E. Draim, P. J. Cefola, and K. J. Ernandes. Seamless handovers in cobra teardrop satellite arrays. *Acta Astronautica*, 61:139–150, 2007.

W. Dudley and M. Lee. *Tsunami!* University of Hawaii Press, 2nd edition, 1998.

T. Eisenman. Noaa continues to increase u.s. tsunami warning capability: Three dart buoy stations deployed off the eastern equatorial pacific ocean. *NOAA Magazine*, R205:1, 2007. URL `http://www.noaanews.noaa.gov/stories2007/s2829.htm`.

T. Eisenman and D. Feltgen. Noaa provides first tsunami detection buoy for Indian Ocean. NOAA News, November 2006.

F. Eugenio, F. Marques, and J. Marcello. Pixel and sub-pixel accuracy in satellite image georeferencing using an automatic contour matching approach. In *International Conference on Image Processing*, volume 1, pages 822–825, October 7-10 2001.

J. Excell. Tsunami detectives: first element of deep-sea early-warning tsunami detection system up and running. *The Engineer*, January 16-29:8, 2006.

J. Font, J. Boutin, N. Reul, P. Waldteufel, C. Gabarro, S. Zine, J. Tenerelli, F. Petitcolin, and J. Vergely. An interative convergence algorithm to retrieve sea surface salinity from SMOS L-band radiometric measurements. In *IEEE International Geoscience and Remote Sensing Symposium (IGARSS)*, 2006.

P. Gaiser, G. Poe, and K. S. Germaine. Critical design issues for space borne polarimetric radiometry. In *IEEE International Geoscience and Remote Sensing Symposium Proceedings*, volume 3, pages 1698–1700, July 1998.

P. Gaiser, K. S. Germaine, E. Twarog, G. Poe, W. Purdy, D. Richardson, W. Grossman, W. L. Jones, D. Spencer, G. Golba, J. Cleveland, L. Choy, R. Bevilacqua, and P. Chang. The WindSat spaceborne polarimetric microwave radiometer: Sensor description and early orbit performance. In *IEEE Transactions of International Geoscience and Remote Sensing Symposium*, volume 42, pages 2347–2361, November 2004.

GAO. U.S. tsunami preparedness: Federal and state partners collaborate to help communities reduce potential impacts but significant challenges remain, June 2006.

K. S. Germain, G. Poe, and P. Gaiser. Polarimetric emission model of the sea at microwave frequencies and comparison with measurements. *Progress in Electromagnetics Research*, 37:1–30, 2002.

M. Glasius. The EU response to the tsunami and the need for human security approach. *European Foreign Affairs Review*, 11:353–378, 2006.

O. A. Godin. Air-sea interaction and feasibility of tsunami detection in the open ocean. *Journal of Geophysical Research*, 109:C05002, 2004.

F. Gonzalez, E. Bernard, C. Meinig, M. Eble, H. Mofjeld, and S. Stalin. The NTHMP tsunameter network. *Natural Hazards*, 35:25–39, 2005.

J. Gower. The 26 December 2004 tsunami measured by satellite altimetry. *International Journal of Remote Sensing*, 28:2897–2913, 2007.

J. Gower. Jason 1 detects the 26 December 2004 tsunami. *Eos*, 86:37–38, 2005.

C. Gumbert, M. Violet, D. Hastings, W. Hollister, and R. Lovell. Assessing mobile satellite systems using a cost per billable minute metric. In *AIAA International Communications Satellite Systems Conference*, pages 888–899, February 1996.

C. Gumbert, M. Violet, D. Hastings, W. Hollister, and R. Lovell. Cost per billable minute metric for comparing satellite systems. *Journal of Spacecraft and Rockets*, 34:837–846, 1997.

M. Halif and S. Sabki. The physics of tsunami: Basic understanding of the Indian Ocean. *American Journal of Applied Sciences 2*, 8:1188–1193, 2005.

J. Hollinger. Passive microwave measurements of sea surface roughness. *IEEE Geoscience Electronics*, 25(2):165–169, 1971.

L. Holthuijsen. *Waves in oceanic and coastal waters*. Cambridge University Press, New York, 2007.

T. Huxley. The tsunami and security: Asia's 9/11? *Survival*, 47:123–132, 2005.

B. Iannotta. Will GOES-R go? *Aerospace America*, July:40–44, 2007.

K. Iida. *Preliminary catalogue of tsunamis occuring in the Pacific Ocean*. Hawaii Institute of Geophysics, University of Hawaii, Honolulu, Hawaii, 1967.

Indian Ocean Tsunami Warning & Mitigation System (IOTWS). Implementation plan third session of the Intergovernmental Coordination Group for the Indian Ocean Tsunami Warning and Mitigation System (ICG/IOTWS-III). Technical Report 71, IOC Technical Series, March 2007. URL `http://ioc3.unesco.org/indotsunami/documents/IOC%20Technical%20Series%2071%20Report_March07.pdf`.

C. Jilla. *A Multiobjective, Multidisciplinary Design Optimization Methodology for the Conceptual Design of Distributed Satellite Systems*. PhD thesis, Massachusetts Institute of Technology, 2002.

M. Kemppinen and M. Hallikainen. The theory and mechanical realization of an ideal scanning method for a single-channel imaging microwave radiometer. *IEEE Transactions on Geoscience and Remote Sensing*, 30(4):743–749, July 1992.

R. Kerr. Continuing Indonesian quake putting seismologists on edge. *Science*, 317:1660–1661, 2007.

L. A. Klein and C. T. Swift. An improved model for the dielectric constant of sea water at microwave frequencies. *IEEE Transactions on Antennas and Propagation*, 25(1):104–111, 1977.

N. Koyama, M. Onda, Y. Sasaki, R. Miura, and W. Akinaga. Tsunami monitoring system by stratospheric LTA platform. In *AIAA 5th Aviation, Technology, Integration, and Operations Conference (ATIO)*, 2005.

D. Kunkee and A. Gasiewski. Simulation of passive microwave wind direction signatures over the ocean using an asymmetric-wave geometrical optics model. *Radio Science*, 32: 59–78, 1997.

G. Lagerloef, Y. Chao, and F. R. Colomb. Aquarius/SAC-D ocean salinity mission science overview. In *IEEE International Conference on Geoscience and Remote Sensing Symposium*, pages 1675–1677, July 2006.

H. Lamb. *Hydrodynamics*. Cambridge University Press, 6th edition, 1932.

B. Lambrigtsen, A. Tanner, T. Gaier, P. Kangaslahti, and S. Brown. Prototyping a new earth observing sensor - GeoSTAR. In *IEEE Aerospace Conference*, pages 1–9, March 2007.

C. Lautenbacher. Tsunami warning systems. *The Bridge*, 35:21–25, 2005.

C. Lautenbacher. Gravity wave refraction by islands. *Journal of Fluid Mechanics*, 41: 655–672, 1970.

B. Lautrup. Tsunami physics. *Kvant*, January:1–6, February 2005.

T. Lay, H. Kanamori, C. Ammon, M. Nettles, S. Ward, R. Aster, S. Beck, S. Bilek, M. Brudzinski, R. Butler, H. DeShon, G. Ekstrom, K. Satake, and S. Sipkin. The great Sumatra-Andaman earthquake of 26 December 2004. *Science*, 308:1127–1133, 2005.

D. Le Vine, G. Lagerloef, S. Yueh, F. Pellerano, and E. Dinnat. Aquarius mission technical overview. Technical report, National Aeronautics and Space Administration (NASA), 2007. URL `http://ntrs.nasa.gov/search.jsp?N$=$4294673175`.

P. Liu. Tsunami simulations and numerical models. University of Southern California's The Bridge, Summer 2005.

A. Lonnqvist. *Applications of Hologram-Based Compact Range: Antenna Radiation Pattern, Radar Cross Section, and Absorber Reflectivity Measurements*. PhD thesis, Helsinki University of Technology, October 2006. URL `http://lib.tkk.fi/Diss/2006/isbn9512283654/`.

M. Martin-Neira and C. Buck. A tsunami early-warning system: the paris concept. ESO Bulletin 124, November 2005.

M. Martin-Neira, C. Buck, S. Gleason, M. Unwin, M. Caparrini, E. Farres, O. Germain, G. Ruffini, and F. Soulat. Tsunami detection using the PARIS concept. In *Progress in Electromagnetics Research Symposium*, August 2005.

R. McCaffrey. GEOPHYSICS: The next great earthquake. *Science*, 315:1675–1676, 2007.

C. Meinig, S. Stalin, A. Nakamura, F. Gonzalez, and H. Milburn. Technology developments in real-time tsunami measuring, monitoring, and forecasting. In *OCEANS*, 2005a.

C. Meinig, S. Stalin, A. Nakamura, and H. Milburn. Real-time deep-ocean tsunami measuring, monitoring, and reporting system: The NOAA Dart ii description and disclosure. Technical report, National Oceanographic and Atmospheric Administration, 2005b. URL `http://nctr.pmel.noaa.gov/Dart/Pdf/DART_II_Description_6_4_05.pdf`.

F. Mello. Under the sea: Network of sensors and robots will probe oceans' mysteries. The Boston Globe, September 10, 2007.

W. Menzel. Applications with meteorological satellites. Technical Report 1078, World Meterological Organization, 2001.

H. Milburn, A. Nakamura, and F. Gonzalez. Deep-ocean assessment and reporting of tsunamis (DART). Technical report, National Data Buoy Center, 1996. URL `http://www.ndbc.noaa.gov/dart/milburn1996.shtml`.

J. Miles. On the generation of surface waves by shear flows. *Journal of Fluid Mechanics*, 3:185–204, 1957.

W. Morrissey. Tsunamis: Monitoring, detection, and early-warning systems. Technical report, CRS Report for Congress, June 2005. URL http://stinet.dtic.mil/cgi-bin/GetTRDoc?AD=ADA465385&Location=U2&doc=GetTRDoc.pdf.

D. Myles. *The great waves*. McGraw-Hill, New York, 1985.

N. Nirupama, T. Murty, I. Nistor, and A. Rao. Energetics of the tsunami of 26 December 2004 in the Indian Ocean: A brief review. *Marine Geodesy*, 29:39–47, 2006.

E. Njoku, E. Christensen, and R. Cofield. The Seasat Scanning Microwave Radiometer (SSMR): Antenna pattern corrections- development and implementation. *IEEE Journal of Oceanic Engineering*, OE-5(2):125–137, April 1980.

NOAA. Pacific tsunami warning system. Internet, December 2007. URL http://www.prh.noaa.gov/ptwc/responsibilities.php.

D. Normile. Tsunami warning system shows agility - and gaps in Indian Ocean network. *Science*, 317:1661, 2007.

E. Okal, A. Piatanesi, and P. Heinrich. Tsunami detection by satellite altimetry. *Journal of Geophysical Research*, 104:599–615, 1999.

S. Padmanabhan, S. Reising, W. Asher, V. Raizer, and P. Gaiser. Correlation of modeled and observed microwave emissivities of water surfaces in the presence of breaking waves and foam. In *IEEE International Geoscience and Remote Sensing Symposium*, 2007.

A. Pasztor. Iridium satellite considers ambitious earth-imaging role. The Wall Street Journal, July 2007.

M. Peichl, S. Dill, and H. Sub. Application of microwave radiometry for buried landmine detection. In *Second International Workshop on Advanced GPR*, May 2003. URL http://ieeexplore.ieee.org/iel5/8580/27169/01207314.pdf.

O. Phillips. On the generation of waves by turbulent wind. *Journal of Fluid Mechanics*, 2: 417–445, 1957.

G. Poe. Optimal interpolation of imaging microwave radiometer data. *IEEE Transactions of Geoscience and Remote Sensing*, 28:800–810, 1990.

V. Raizer. Statistical modeling for ocean microwave radiometric imaging. In *IEEE International Geoscience and Remote Sensing Symposium*, 2002.

V. Raizer. Texture models for high-resolution ocean microwave imagery. In *IEEE International Geoscience and Remote Sensing Symposium*, 2005a.

V. Raizer. Microwave radiometric signatures of ocean internal waves. In *IEEE International Geoscience and Remote Sensing Symposium*, 2007a.

V. Raizer. Correlation analysis of high-resolution microwave radiometric images. In *IEEE International Conference on Geoscience and Remote Sensing Symposium*, volume 3, pages 1907–1910, 2004.

V. Raizer. High-resolution passive microwave-imaging concepts for ocean studies. In *MTS/IEEE OCEANS*, 2005b.

V. Raizer. Images Courtesy of V. Raizer, 2007b.

A. Ratier. Space-based observations in the global ocean observing system: The operational transition issue. In *Ocean Observations*, 1999.

I. E. N. Record. Indonesia to add warning system. Internet Engineering News Record, September 2006.

B. Richardson. New push for tsunami-alert system. Christian Science Monitor, December 29 2004.

I. Robinson. *Measuring the oceans from space: The principles and methods of satellite oceanography*. Praxis, 2004.

G. Rosborough, D. Baldwin, and W. Emery. Precise AVHRR image navigation. *IEEE Transactions of Geoscience and Remote Sensing*, 32:644–657, 1994.

T. Russell. The humanitarian relief supply chain: Analysis of the South East Asia earthquake and tsunami. Master's thesis, Massachusetts Institute of Technology, 2005.

G. Shaw. *The Generalized Information Network Analysis Methodology for Distributed Satellite Systems*. PhD thesis, Massachusetts Institute of Technology, 1998.

D. Shin, J. Pollard, and J.-P. Muller. Accurate geometric correction of ATSR images. *IEEE Transactions of Geoscience and Remote Sensing*, 35(4):997–1006, 1997.

R. Silva, I. Losada, and M. Losada. Reflection and transmission of tsunami waves by coastal structures. *Applied Ocean Research*, 22:215–223, 2000.

R. Singh, G. Cervone, M. Kafatos, A. Prasad, A. Sahoo, D. Sun, D. Tang, and R. Yang. Multi-sensor studies of the Sumatra earthquake and tsunami of 26 December 2004. *International Journal of Remote Sensing*, 28(13):2885–2896, 2007.

N. Skou and D. Le Vine. *Microwave Radiometer Systems: design and analysis*. Artech House, 2nd edition, 2006.

N. Skou, S. Sobjaerg, J. Balling, and S. Kristensen. A second generation L-band digital radiometer for Sea Salinity campaigns. In *IEEE International Geoscience and Remote Sensing Symposium*, pages 3984–3987, July 2006.

W. Smith, R. Scharroo, V. Titov, D. Arcas, and B. K. Arbic. Satellite altimeters measure tsunami. *Oceanography*, 18:11–13, 2005.

Staff. Deep tsunami waves off the Sri Lankan coast. Earth Observatory, NOAA, 2005a. URL `http://earthobservatory.nasa.gov/Newsroom/NewImages/images.php3?imgid16802`.

Staff. World bank response to the tsunami disaster. World Bank Report, February 2005b.

E. Stokstad. Ocean research gets a modest boost. *Science*, 315:585–586, 2007.

R. Stone and R. Kerr. Girding for the next killer wave. *Science*, 310:1602–1605, 9 December 2005.

S. Tadepalli and C. Synolakis. The run-up of N-waves on sloping beaches. *Proceedings of the Royal Society of London A*, 445:99–112, 1994.

G. Teissonniere. Economic impact of tsunami disaster. *Carribean Business*, January 13:8, 2005.

E. Thomas, G. Wehrfritz, S. Mazumdar, J. Overdorf, J. Cochrane, E. Unmacht, P. Dillon, A. Murr, J. Reno, E. Conant, S. Tuttle, T. T. Gegax, and J. Scelfo. Tide of grief. *Newsweek*, 145:Issue 2, 2005.

V. Titov, A. B. Rabinovich, H. O. Mofjeld, R. E. Thomson, and F. I. Gonzalez. The global reach of the 26 December 2004 Sumatra tsunami. *Science*, 309:2045, 2005.

A. Trembly. US to bolster tsunami warning technology. *National Underwriter*, March 14: 26, 30, 2005.

K. Trimbath. Researchers confirm asian tsunami detected by hydrophones. *Civil Engineering*, December:33, 2005.

Y. Troitskaya and S. Ermakov. Manifestations of the Indian Ocean tsunami of 2004 in satellite nadir-viewing radar backscatter variations. *Geophysical Research Letters*, 33: L04607, 2006.

Y. Trokhimovski. Microwave radiometric measurements of atmospheric internal waves over ocean. In *IEEE International Geoscience and Remote Sensing Symposium*, pages 1981–1982, June 1999.

F. Ulaby. *Microwave remote sensing: active and passive*, volume 1. Addison-Wesley Publishing Company, 1981.

University of Washington. Tsunami! Department of Earth and Space Sciences Website, March 2005. URL `http://www.geophys.washington.edu/tsunami/general/historic/aleutian46.html`.

J. Villagran de Leon and J. Bogardi. Early warning systems in the context of disaster risk management. *entwicklung & lndlicher raum*, February:23–25, 2006.

Vitaliy. Research Centre for Earth operative monitoring, 2005. URL `http://eng.ntsomz.ru/spacecraft/sich_m/`.

S. Voit. Tsunamis. *Annual Review of Fluid Mechanics*, 19:217–236, 1987.

M. Wilson. Modeling the Sumatra-Andaman earthquake reveals a complex, nonuniform rupture. *Physics Today*, June:19–21, June 2005.

B. Wood. An analysis method for conceptual design of complexity and autonomy in complex space system architectures. Master's thesis, Massachusetts Institute of Technology, 2001.